NORTHWESTERN UNIVERSITY

Probing the Transition from the Diffuse to the Molecular ISM

A DISSERTATION

SUBMITTED TO THE GRADUATE SCHOOL

IN PARTIAL FULFILLMENT OF THE REQUIREMENTS

for the degree

DOCTOR OF PHILOSOPHY

Field of Physics & Astronomy

By

Cody Dirks

EVANSTON, ILLINOIS

September 2019

ABSTRACT

Probing the Transition from the Diffuse to the Molecular ISM

Cody Dirks

The study of the translucent interstellar medium (ISM) is important for understanding the behavior of the ISM as it transitions from hot, tenuous gas to dense, star-forming regions. This regime is know to be associated with the initial formation of persistent molecular material, and thus represents the first stages of the process that eventually forms the large molecular clouds responsible for the bulk of the star formation in the Galaxy. The *Planck* mission has provided a wealth of information about this regime of the ISM via the *Planck* Catalogue of Galactic Cold Clumps, which contains thousands of sources of cold dust emission. These sources represent a broad range of physical conditions spanning from diffuse sources with relatively little molecular material to dense, highly molecular cores embedded within larger molecular cloud complexes.

This work uses high-resolution ultraviolet absorption-line spectroscopy from the *Hubble Space Telescope* to investigate these sources and thus study the translucent ISM. 25 spectroscopic targets whose sightlines probe the environments of a PGCC source were chosen. Neutral carbon and carbon monoxide were used to probe the gas content of these

environments, while oxygen, krypton, germanium, magnesium, and nickel were used to probe the dust content.

Analyses of these species reveal that a transition occurs around a CO column density of N(CO)$\sim 10^{15}$ cm^{-2}. Above this threshold, it appears that smoother, more coherent molecular envelopes begin to form out of the patchier, diffuse ISM that is present below this threshold. These molecular envelopes show evidence of being quiescent rather than turbulent, dynamic sources. Additionally, a correlation is observed between the presence of molecular gas and elemental depletion onto dust grains within these sources. Taken as a whole, these results suggest that the PGCC sources do indeed represent an important transitionary phase of the ISM.

Acknowledgements

The following work represents the culmination of years of work, beginning with a little kid's fascination with looking up at the night sky. Myriad people over those years have been instrumental in making this dissertation possible, and I would be remiss if I did not include them within these pages.

Firstly and most importantly, I would like to thank my mother, my father, my sister and the entire Dirks-Schafer family for their unconditional love and support throughout this journey. From a young age they nurtured my interest in outer space, making sure I had my very own telescope and an endless supply of books that kept me engaged and interested in the Universe around me. As a by-product of this, they instilled in me a lifelong curiosity of the unknown and willingness to engage with and learn new things, without which I never would have made it through years of schooling and research.

I would also like to thank Dr. Dave Meyer for his mentorship during my time at Northwestern. He has been a constant source of information and expertise, ranging from technical details about telescopes and instrumentation, to tips on writing research grant proposals, to guidance on how to engage the general public in science. His advice throughout my time in graduate school has been pivotal in the completion of this research and in making me a better scientist.

Additionally, I would like to thank Dr. Giles Novak and Dr. Claude-André Fauchere-Giguère for serving on my dissertation committee and reviewing this work.

Thank you to all of my fellow graduate students in the Department of Physics & Astronomy and CIERA whom I've crossed paths with over the years. Graduate school is an arduous undertaking, and having a group of friends to rely on for support, to ask seemingly silly research questions, and to empathize with during the most stressful times has kept me sane throughout the entire process.

To the many, many other people not listed here – friends, teachers, co-workers, etc. – I am forever grateful for your influence on me and my formation into someone capable of writing the following work.

Table of Contents

List of Tables

List of Figures

CHAPTER 1

Introduction

1.1. The Multi-Phase Interstellar Medium

The multi-phase picture of the interstellar medium (ISM) was first described in McKee & Ostriker (1977), who theorized that the energy and radiation from supernova explosions within the Galaxy would necessarily produce a medium that was filled primarily by hot, ionized gas. Embedded within this hot gas are cold, relatively dense clouds, which are in turn surrounded by warm gas which is partially ionized by the radiation from nearby early-type stars. These various components coexist due to approximate pressure equilibrium between the phases, where the pressure is a function of the temperature and density of the medium. Thus, understanding the star formation process in the Milky Way entails unraveling the process by which the ISM transitions from the hot, tenuous phase that fills the majority of the volume of the Galaxy to a dense, molecular phase where the majority of the mass and star formation is observed to reside.

The various regimes inherent to this multi-phase medium are described in Snow & McCall (2006) as being defined by two primary factors: the hydrogen content and carbon content of the medium. As the ISM transitions through these regimes from a diffuse state to a dense one, the hydrogen content must transition from a neutral atomic form (denoted H I) to diatomic, molecular hydrogen (H_2). H_2 represents a critical component of the ISM, as it is the most common molecule in interstellar gas and is the primary source

of the mass used to form new stars. For this transition from atomic to molecular hydrogen to progress, the interstellar gas must meet the following conditions: its density must be high enough for individual hydrogen atoms to interact, it must be cold enough for these molecules to not immediately dissociate upon formation, and the interstellar ultraviolet radiation field must be small enough that the molecules are not quickly photodissociated by UV photons.

In a similar manner, the carbon content must transition from a primarily atomic phase to a primarily molecular phase. In the more diffuse regions of the ISM, carbon primarily exists in the form of the singly ionized C II, which serves as one of the primary coolants of the warm ISM via emission at 158μm. Additionally, the electrons that were photoionized to generate C II often serve to inhibit the molecular chemistry in this regime. These free electrons destroy molecules via the dissociative recombination process, in which common interstellar molecular ions such as CH^+, CN^+, and H_3^+ re-combine with the electrons, and the resulting neutral molecule dissociates. As physical conditions change and ISM transitions toward cooler, denser regimes, the carbon becomes increasingly neutral in the form of C I. The resulting decrease in free electrons allows molecular chemistry to begin in earnest. As the molecular hydrogen abundance becomes non-negligible, other less-abundant molecules begin to form as well, the most important of which is carbon monoxide (CO).

CO has long been known to be an important constituent of the ISM. It serves an important physical role as a coolant in the molecular ISM (Goldsmith & Langer 1978), as emission via its rotational transitions allows the medium to cool down to extremely low temperatures, which enables gas to reach the densities necessary to trigger new star

formation. Additionally, as will be discussed in detail in later sections of this work, CO serves as an important observational tracer of H_2 and of the dense, molecular ISM in general. Since its initial detection toward the Orion Nebula by Wilson et al. (1970), observations of CO have been used to determine that H_2 is extremely common (in fact, more abundant than H I) in the inner Galaxy (Stecker et al. 1975), to map the molecular content of the entire Galactic plane (Dame et al. 1987), as well as to determine the molecular mass of other galaxies (Young & Scoville 1982).

Because of the utility of CO as a diagnostic tool to study molecular hydrogen and the cold dense ISM as a whole, understanding the behavior of both hydrogen and carbon as they transition between these multiple phases is critical in developing a complete picture of the evolution of a complex, multi-phase ISM. The relative abundances of hydrogen and carbon in its various ionized, neutral, and molecular states are shown in Figure 1.1, which visualizes results from astrochemical modeling performed by Neufeld et al. (2005). It should be noted that the specific values and abundances present in Figure 1.1 are not meant to be definitive – as will be discussed later, theoretical modeling of the chemistry of the ISM can be inconsistent. Rather, they are intended to be illustrative of the typical behavior of these important species as the ISM progresses from a relatively diffuse state to a dense, molecular-rich phase, as well as to approximately quantify the abundances and column density ranges which define the "diffuse atomic," "diffuse molecular," "translucent," and "dense molecular" regimes which will be referenced throughout this work.

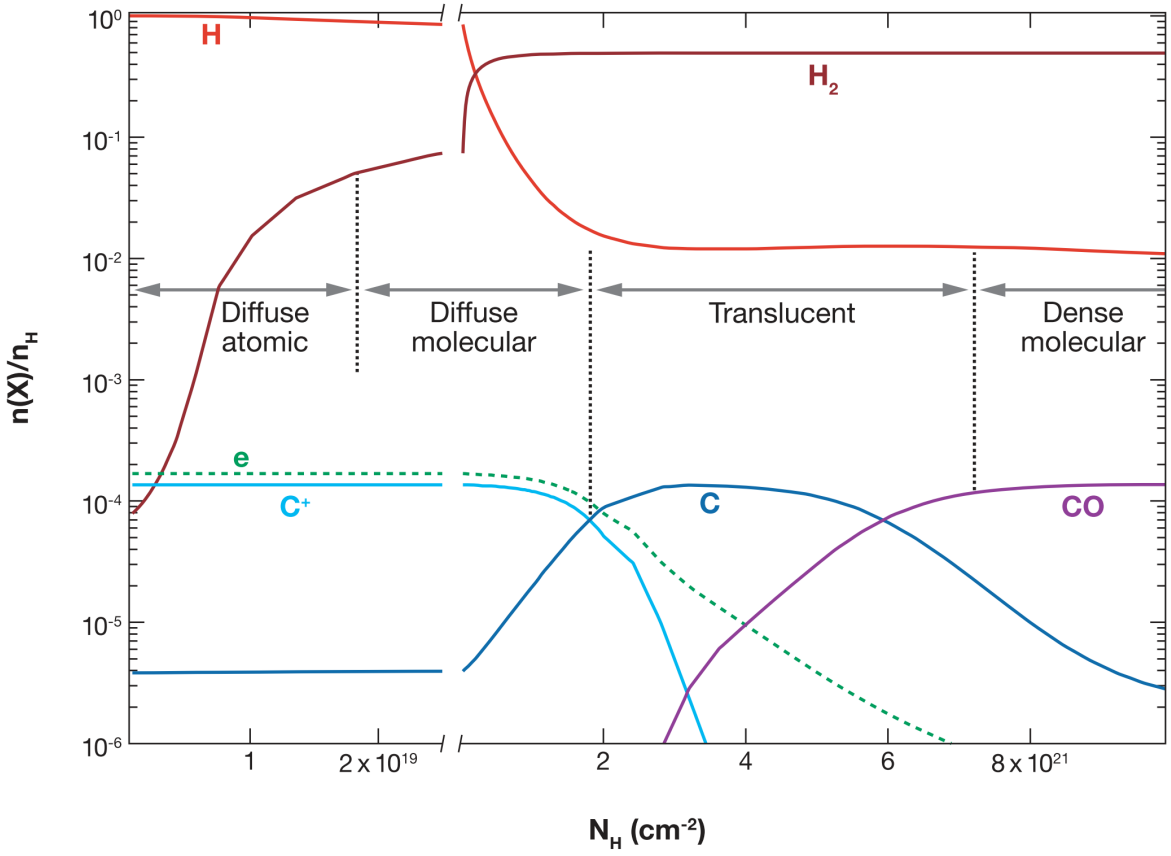

Figure 1.1. Figure 1 of Snow & McCall (2006), which illustrates results from astrochemistry models in Neufeld et al. (2005). Behavior of the hydrogen and carbon content as a function of total hydrogen column density, N(H), with approximate diffuse/molecular regimes noted.

The proposed physical mechanisms which drive the transition between these phases primarily involve processes that generate converging gas flows which drive material together in such a way that increases the local density and allows for the necessary chemical reactions to produce molecular material. Due to the extreme compressibility of the ISM, these are often turbulent processes. One of the main mechanisms by which this may occur is stellar feedback, where the energy output from supernovae or young early-type stars

creates a bubble of hot, ionized H II that then expands outward, sweeping up and compressing the ambient medium (McKee & Ostriker 1977; Vazquez-Semadeni et al. 1995). These expanding flows generate turbulence within the surrounding ISM, triggering further formation of cold, dense material. Simulations of such scenarios indicate that such processes are capable of generating molecular clouds with masses of a few times 10^4 $M_\odot$ (Vázquez-Semadeni et al. 2007). However, most of the molecular mass within the Milky Way is observed to reside in clouds with masses greater than 10^5 $M_\odot$ (Heyer & Dame 2015), implying that there must be some other mechanism by which these giant molecular clouds (GMCs) form. This could either occur by accretion of many of the aforementioned $\sim 10^4$ $M_\odot$ clouds, or by some other process capable of directly create these GMCs. Cloud-cloud collisions induced by the spiral arm structure of the Galaxy has been shown to be an effective method to build up GMC-scale clouds within the necessary timescale. Figure 1.2 shows results from a Dobbs & Pringle (2013) simulation of a galactic disk, which found that GMCs are often formed from a combination of smaller clouds, and follow a similar spatial structure to spiral arm density structures.

1.1.1. Interstellar Dust

A relatively small yet critically important component of the ISM is the population of interstellar dust grains – a broad term that encapsulates complex species ranging from tens of atoms in size up to micron-sized agglomerations (Draine 2003). These particles have a significant effect on the chemical composition of the ISM. This is due to the wide range of chemical reactions (including the formation of H_2 molecules (Hollenbach & Salpeter 1971)) for which dust grains serve as a catalyst, with these reactions taking

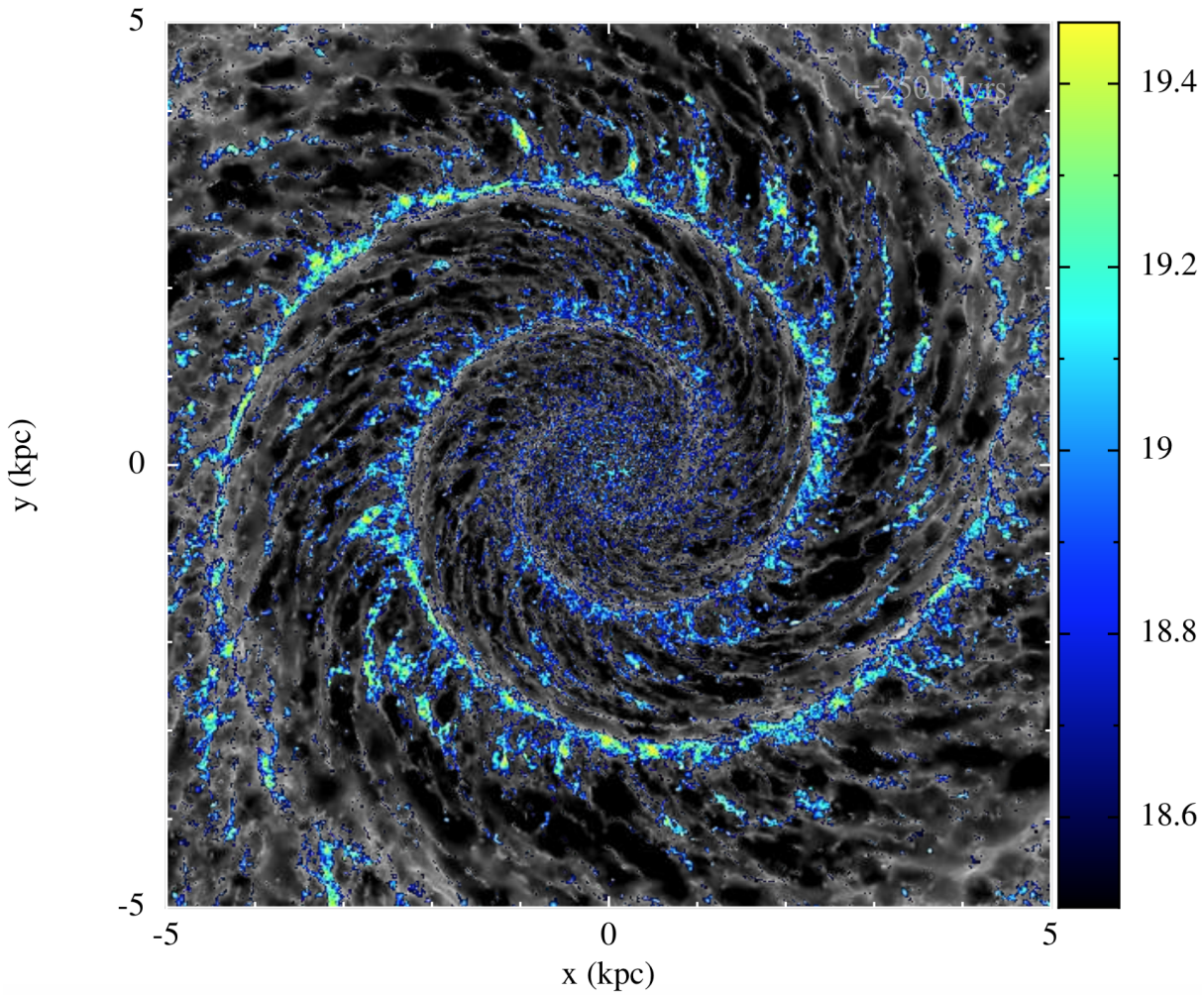

Figure 1.2. Snapshot of a Dobbs & Pringle (2013) simulation of the evolution of molecular material within a spiral disk. The background greyscale represents the total gas distribution, while the colorbar shows the log $N(H_2)$ distribution. Of note is the clear link between the spiral structure of the galaxy and the location of molecular cloud complexes.

place on the surface of the grains. Furthermore, as there must exist both a sufficient density for dust grains to accumulate multiple atoms, as well as an ambient radiation field weak enough to prevent the photodissociation of the dust grain, one might expect a link between the dust content and the molecular content of a particular ISM region of

interest. Simulations of the relationship between the dust and gas in the ISM have shown that the dust-to-gas ratio is dependent on the grain size (Hopkins & Lee 2016), as these dust grains behave as aerodynamic particles and thus are not necessarily well-coupled to the dynamics of the gas.

This dust-to-gas relationship was first investigated observationally at high Galactic latitudes by Boulanger et al. (1996), who found a good linear relationship between the dust emissivity τ and the total hydrogen column density N_H, with

$$\tau/N_H = 1.0 \times 10^{-25} \, (\lambda/250\mu\mathrm{m})^{-2} \, \mathrm{cm}^2. \tag{1.1}$$

More recently however, the *Planck* mission was able to simultaneously gather maps of thermal dust emission and CO emission, and use these two maps in conjunction with each other to determine a dust-to-gas ratio. They determined that there was an excess of dust emission relative to what would be expected from a simple linear correlation in the column density range of $\sim 8 \times 10^{20} < N_H < 5 \times 10^{21}$ cm^{-2} . Since the *Planck* team derived the total gas content using CO emission, they interpreted this excess as evidence of "dark molecular gas" – that is, dense molecular gas which contains dust, but has yet to form enough CO to be detectable via emission.

As dust grains form and grow within the ISM, different chemical elements vary in their chemical interactions with the grains. As a result, some elements are more readily depleted onto these grains while others that interact with the dust are able to break free and return to the gas phase quite easily. Any persistent depletion onto dust grains necessarily reduces the gas-phase abundance of these elements, and thus observations of these gas-phase abundances may yield insight into the prevalence of dust in the ISM. Jenkins

(2009) studied the behavior of these gas-phase depletions in great detail. By simultaneously comparing the observed gas-phase abundances of 17 different atomic species, they developed an empirical model which characterized the overall depletion along any given sightline with a parameter F_*, and determined how strongly the depletion of each individual gas-phase species was correlated with F_*. That is to say, some elements (for example, nickel and magnesium) are strongly depleted and thus have observed gas-phase abundances that are strongly coupled to this overall depletion factor. Others (such as oxygen or krypton) are not as easily depleted, and thus have abundances that only vary by a small amount between weakly and strongly depleted sightlines.

In the Jenkins (2009) study, oxygen and krypton displayed unusual depletion characteristics, both being more strongly depleted than one would naturally expect from simple chemical principles. As oxygen is believed to be primarily depleted onto silicates and oxides, the oxygen depletion would be expected to be correlated with the relative depletions of the other elements known to reside in these silicates and oxides, such as Ni, Ge, and Si. It was found, however, that the amount of oxygen tied up in dust was a factor of ~ 1.5 larger than expected. Similarly, krypton, which is an inert noble gas, would be expected to show almost essentially no depletion, and yet it was found that the krypton abundance decreased with increasing F_*. These larger-than-expected depletions could be evidence of either incorrect reference abundances, or the presence of some unknown physical process that changes the expected depletion patterns. Jenkins (2019) specifically followed up on the behavior of these oxygen and krypton abundances to better understand how these specific elements are incorporated into dust grains and to more accurately determine their gas-phase depletion characteristics.

1.2. Theoretical Work

Tracing the transition between a diffuse ISM and a dense, star-forming ISM involves investigating the diffuse molecular and translucent regimes that bridge the gap between these two extremes. The physical space in which this process occurs in the ISM is referred to as a photodissociation region (PDR), a term for the regions of space where the physical conditions are such that the ISM density has increased to the point where H_2 can begin to form on dust grains, but the interstellar radiation field (ISRF) is such that these molecules are routinely destroyed by the absorption of FUV photons in the Lyman and Werner bands. Thus, the molecular abundance is controlled by the ratio between the gas density n_H and the FUV radiation intensity I_{UV}. Once the abundance of H_2 has increased sufficiently to self-shield itself from destruction via photodissociation, it can serve as a seed and catalyst for a large number of chemical reactions yielding other molecules, including CO. Importantly, the density at which H_2 begins to effectively self-shield is different that that of CO, yielding imbalances in the molecular fractions of hydrogen and carbon, respectively.

The translucent ISM first studied theoretically by van Dishoeck & Black (1988), who performed photochemistry models of the ISM specifically focused on the chemistry of hydrogen and carbon. They defined "translucent" in their results to refer to material where carbon has transitioned from a primarily ionized atomic state (i.e. C II) to neutral atomic (C I) and molecular forms, as opposed to the traditional observational definition of an extinction A_V is ~ 1. This regime is somewhat less well understood that its more diffuse and dense counterparts, and theoretical models of this regime vary in their predictions of the relative abundances of these ionized atomic, neutral atomic, and molecular forms.

In the years since van Dishoeck & Black (1988), detailed simulations involving complex chemical modeling attempted to capture in more detail the behavior of these abundances as a function of n_H and/or I_{UV}. Wolfire et al. (2010) focused on the different regimes where hydrogen and carbon transition to their respective molecular phases, in order to evaluate how much H_2 exists in the transitionary regime where C II still dominates the carbon budget. Due to the lack of the common observational tracer CO, this would be analogous to the "dark molecular gas" or "CO-dark gas" suggested by the *Planck* observations. This gas may be important in understanding the true abundance of molecular gas in the ISM, since Wolfire et al. (2010) estimates that as much as 30% of the molecular gas in the ISM exists in this dark form. Others, such as Krumholz et al. (2008) built models with more complex and realistic geometries, both in the structure of the gas of interest and the impinging radiation fields. Their results showed that while simple, one-dimensional PDR models may work well for dense, opaque clouds, they often fail for the cases of smaller clouds or weaker radiation fields.

A further complicating factor is the time-dependence of interstellar chemistry – the presence of supersonic turbulence and shock effects in interstellar gas often means that the gas is not in chemical equilibrium, yet many 1D PDR models assume a steady state due to the complexity of incorporating a full time-dependent chemical network. Advancements have been made in recent years by approximating a full time-dependent chemical network with a small number of the species deemed to be the most important to the behavior of the gas. Glover & Clark (2012) showed that such lightweight networks are viable, as the resulting thermodynamics of full time-dependent networks are not particularly sensitive to the detailed chemistry within the gas. These important species are typically deemed

relevant for one or more of the following reasons: a) they factor into the heating and cooling of the gas, such as CO or C II, both of which represent important coolants of the gas in their respective regimes, b) they are observationally important such as CO and H_2, and c) they represent critical pathways of chemical formation or destruction, such as H_3^+, which is an important starting point for many ion-molecule reactions Oka (2013).

The most recent of these lightweight, time-dependent chemical networks is that of Gong et al. (2017), which expanded upon the previous such networks described in Nelson & Langer (1999) and Glover & Clark (2012). This model performs extremely well in reproducing the abundances of CO and other dense gas tracers in density regimes of n between 100 cm^{-3} and 1,000 cm^{-3}. However, in more diffuse and translucent regimes, this model overpredicts the abundance of C I (and the resulting diagnostic ratio CO/C I) by at least an order of magnitude compared to observational results (Figure 1.3). This appears to be a common feature of PDR simulations and chemical network modeling, indicating that the behavior of C I and its role as a transitionary species between C II and CO remains poorly understood. Gong et al. (2017) note that while this may be due in part to inaccuracies in the chemical network model, it is also likely in part due to non-equilibrium effects, as C I primarily resides in the outer regions of these translucent clouds which are inherently less dense and less shielded from the interstellar radiation field, making them more susceptible to dynamical effects that drive abundances away from equilibrium.

With this in mind, Clark et al. (2018) carried out magnetohydrodynamic simulations of the collision of two atomic clouds and the resulting formation of molecular gas, and performed post-processing on these simulations using a radiative transfer code to produce synthetic C II, C I, and CO emission data, in an attempt to test how radio observations

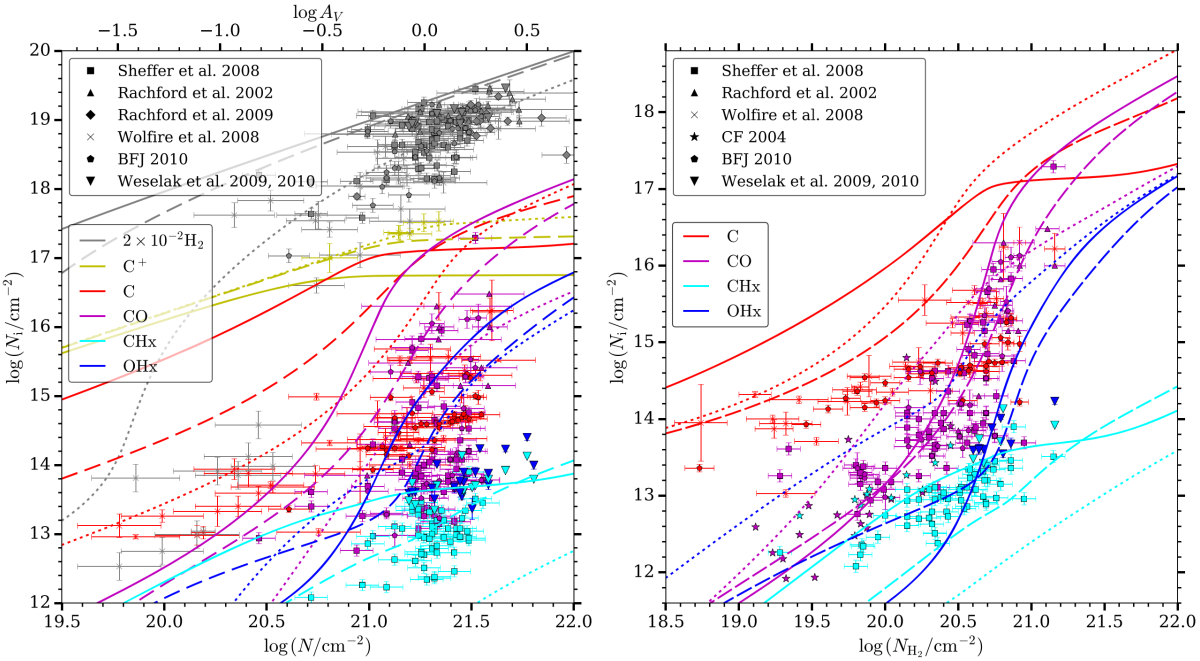

Figure 1.3. Figure 10 from Gong et al. (2017). Comparison between theoretical chemical network simulations and various observational results (Rachford et al. 2002; Crenny & Federman 2004; Sheffer et al. 2008; Wolfire et al. 2008; Rachford et al. 2009; Weselak et al. 2009; Burgh et al. 2010; Weselak et al. 2010). We note that the total column density range shown on the horizontal axis ($\sim 3 \times 10^{19}$ to 1×10^{22} cm^{-2}) corresponds roughly to the diffuse molecular and translucent regimes shown in Figure 1.1 ($\sim 2 \times 10^{19}$ to 7×10^{21} cm^{-2}). Theoretical curves are shown for number densities of 10 cm^{-3} (dotted lines), 100 cm^{-3} (dashed lines), and 1,000 cm^{-3} (solid lines). Of note is the general agreement for molecular species H_2, CO, CH_x, and OH_x and the significant over-prediction for neutral atomic carbon (C I) by at least an order of magnitude.

of the C II fine-structure line at 158 μm, the C I fine-structure lines at 370 μm and 609 μm, and the CO J=1-0 line at 2.6 mm might be used to trace the formation of molecular clouds. They found that while hydrogen transitions from predominately atomic to molecular at a number density of $\sim$ 100 cm^{-3}, the carbon is primarily ionized up to number densities $> 1,000$ cm^{-3}, indicating that while these C I and CO lines both trace

primarily molecular gas, there is a significant portion of molecular gas not traced by emission from these species. These results highlight the importance of carbon chemistry to understanding the process by which dense, molecular gas forms in the ISM, which also highlighting the necessity for additional observational data of these species.

1.3. CO as a Tracer of H_2

Due to the diatomic nature of H_2, it has no (permanent) dipole moment by which to emit radiation, and emits only very weakly via its rotational quadrupole transitions. Thus, H_2 is essentially impossible to observe directly via emission surveys. As has already been alluded to in previous sections, this necessitates the use of indirect methods such as observations of the CO (J=1-0) emission line at 2.6 mm, coupled with the assumption that CO is a reliable tracer of H_2. Determining the conversion factor between CO and H_2, $X_{\rm CO}$, has been a point of emphasis of radio astronomy (see Bolatto et al. 2013, and references therein for a detailed review). In the terminology of radio astronomy, $X_{\rm CO}$ is quantified as:

$$\mathrm{N(H_2)} = X_{\rm CO}\,\mathrm{W(CO)}, \tag{1.2}$$

where W(CO) denotes the integrated line intensity of the J=1-0 emission line, in units of K km s^{-1}. However, since this emission is most commonly detected toward regions where the gas is optically thick, W(CO) is not easily converted into a column density N(CO), and thus a measurement of $X_{\rm CO}$ is not necessarily equivalent to the an abundance ratio N(CO)/N(H_2). Despite this issue, CO observations still serve as the primary tracer of dense, molecular gas within the ISM.

To circumvent the issue of optically-thick CO emission and correctly determine the CO column density, the isotope ^{13}CO is often measured instead. This species is considerably less abundant than ^{12}CO, which represents the most common CO isotope (and that which is typically referred to when CO is discussed). Thus, the emission observed from ^{13}CO is more likely to be optically thin and capable of producing an accurate measurement of the CO column density. This necessitates the use of a CO isotope ratio ^{12}CO/^{13}CO to determine a ^{12}CO column density, which is then translated further into a H_2 column density.

This CO isotope ratio is often chosen to be a constant conversion factor of ∼70 that corresponds to the elemental ^{12}C/^{13}C isotope ratio (Wilson 1999; Pineda et al. 2010). However, the ^{12}C/^{13}C isotope ratio has been shown to exhibit large-scale variations with Galactocentric distance, from ∼24 near the Galactic center to ∼70 at 12kpc (Langer & Penzias 1990). Furthermore, recent hydrodynamic simulations by Szűcs et al. (2014) have shown that the ^{12}CO/^{13}CO ratio can vary quite dramatically within the turbulent gas of an individual molecular cloud, independent of any variations in the elemental ^{12}C/^{13}C ratio. This is primarily due to two isotope-selective processes. The first of these – selective photodissociation – occurs when slight shifts in the locations of spectral lines result in preferential photodissociation of specific isotopes by UV radiation. The other process – chemical fractionation – occurs when ^{13}C is preferentially incorporated into CO molecules via the exothermic reaction

$$^{13}C^{+} + {}^{12}CO = {}^{12}C^{+} + {}^{13}CO + \Delta E \tag{1.3}$$

discussed in Watson et al. (1976).

If these CO isotopes within a given cloud have been differentiated by these processes and thus exist in slightly different locations within the cloud, this effect can also be detected observationally via shifts in the central line velocity of each observed isotope. This effect was seen in Zhang et al. (2011), who studied individual dense cores within the larger infrared dark cloud (IRDC) complex G084.81-01.09, and found that each of the six individual identified cores had a velocity shift of > 1 km s^{-1} between the observed ^{12}CO and ^{13}CO emission.

In addition to large-scale CO emission surveys at radio and sub-millimeter wavelengths, observations at ultraviolet wavelengths (discussed in detail in §1.4) provide a powerful complementary tool to study the molecular ISM, due to the vast array of spectral lines present in this regime. In particular, direct observations of Lyman and Werner absorption by H_2 are possible in the far-UV blueward of 1115 Å (Spitzer & Zabriskie 1959). These H_2 observations can be coupled with observations of CO molecular absorption in the UV, as CO has an extensive system of over a dozen absorption bands accessible in the far-UV. These observations allow for direct measurements of the relationship between H_2 and CO, better constraining both the theoretical models that investigate the molecular ISM, as well as the interpretation of observational data at radio wavelengths.

1.4. Previous Studies in the Translucent Regime

Ultraviolet observations of the molecular content of the ISM began with the discovery of molecular hydrogen via UV absorption by Carruthers (1970). Due to telluric absorption, these observations can only be made from above the Earth's atmosphere, and thus these early experiments relied on sounding rockets to carry instruments to high altitudes.

While they showed that such UV measurements were possible, these sounding rocket experiments were extremely limited in their available observing time and therefore only gathered limited data on a few bright targets. This paradigm changed with the advent of orbiting space-based observatories, beginning with the *Orbiting Astronomical Observatory (OAO)* series of launches in the late 1960s. With these technologies, large-scale surveys of broad swaths of the sky could be performed, and thus UV studies of the molecular ISM could begin in earnest. Here we discuss key findings from several important satellites over the past four decades.

1.4.1. *Copernicus*

Originally designated *OAO-3*, *Copernicus* operated from August 1972 to February 1981, and was equipped with a 0.8m aperture and six UV detectors. Of particular use to the study of molecular hydrogen were the U1 and U2 detectors, which covered the wavelength range 900-1560 Å at spectral resolutions R of 20,000 and 5,000, respectively. *Copernicus* directly measured H_2 column densities along 100 sightlines, providing the first opportunity to study in detail the general properties of the molecular content of the ISM. Many of the results of these observations are detailed in Shull & Beckwith (1982), but among the key results were the discovery that the molecular hydrogen fraction $f_{H_2} = 2N(H_2)/N(H_{tot})$ is correlated with the observed sightline extinction *E(B-V)*, and that f_{H_2} undergoes a transition from low to high values around $E(B-V) \approx 0.08$. Jura (1975a) was able to estimate the number density of H_2 toward their sample of sightlines ranged from $15 \leq n \leq 900$ cm^{-3}, while Jura (1975b) noted that an appreciable fraction ($> 50\%$) of their sightlines appeared to be strongly irradiated, indicating a physical association between the

observed molecular material along a line of sight and the hot OB stars used as background UV sources.

Another important area of study first enabled by *Copernicus* is the study of gas thermal pressures using the fine-structure excited states of neutral carbon. These J=1,2 states are populated when these C I atoms collide with ambient H atoms, and thus are sensitive to the local gas thermal pressure. Jenkins & Shaya (1979) detected variations in this thermal pressure along different sightlines, as well as finding evidence of gas with pressures well above the ISM average. However, due to the limited bandpass and sensitivity of *Copernicus*, more detailed studies of these gas pressures would not be possible until more advanced space-based spectrographs were launched.

1.4.2. *International Ultraviolet Explorer*

While *Copernicus* built a database of observed objects that measured in the hundreds, the *International Ultraviolet Explorer (IUE)* (Boggess et al. 1978) represented the first large-scale UV database, gathering more than 100,000 spectra covering over 10,000 different targets during its operational run from 1978 to 1996. *IUE* also carried two independent spectrographs, covering the spectral ranges of 1150-1950 and 1950-3400 Å. *IUE* excelled in studies of the neutral atomic hydrogen content, due to the presence of the Lyman-alpha (Lyα) lines at the blueward edge of its wavelength coverage. The damping wings of these Lyα lines can be fit to determine N(H I) to within 0.1 dex. In a molecular context, the wavelength regime of *IUE* excludes the Lyman H_2 bands near 1050 Å and thus cannot directly probe H_2 abundances, instead relying on the CO $A-X$ bands present in the UV between 1300 and 1550 Å to probe molecular content.

Measurements from *IUE* have been used to quantify the relationship between N(H I) and $E(B-V)$ (Shull & van Steenberg 1985), with an average N(H I)/$E(B-V)$ = 5.2 $\times$ 10^{21} cm^{-2}. Additionally, detailed analyses of the molecular content were possible toward specific sightlines, such as X Per (Kaczmarczyk 2000; Lien 1983), μ Oph (Cardelli & Boehm-Vitense 1982), and HD 110432 (Rachford et al. 2001), as well as broader studies covering many sightlines (Tarafdar & Krishna Swamy 1982; Sonnentrucker et al. 2007). While these studies were extraordinarily useful in correlating molecular content with other sightline properties such as $E(B-V)$, a major limitation of *IUE* was the dynamic range of its sensitivity. In practice, sightlines with extinctions greater than $E(B-V) \sim 0.5$ were quite difficult to observe, and thus the ability of *IUE* to probe the full transition to dense molecular material was limited.

1.4.3. *Far Ultraviolet Spectroscopic Explorer*

The *Far Ultraviolet Spectroscopic Explorer* (*FUSE*) mission, launched in 1999, was designed with molecular ISM studies in mind (Moos et al. 2000). The higher spectral resolution (R$\sim$20,000) allow for the disentangling of the multitude of strong absorption lines in the far-UV regime at which *FUSE* operates, roughly 905 to 1187 Å. Additionally, the instrumental throughput was optimized to be at a maximum near the Lyman H_2 bands near 1050Å, allowing for extremely sensitive studies of molecular hydrogen, particularly in the translucent ISM. Rachford et al. (2002) conducted the first survey of translucent sightlines using *FUSE*. Using a sample of 23 sightlines, they showed that the linear relationship between the interstellar extinction A_V and the total sightline column density, N(H) = 5.8×10^{21} cm^{-2} mag^{-1} $\times$ A_V. This value was consistent with the results

determined with *IUE*, but their work was able to show that this relationship remained valid up to an extinction of ∼1, the extinction traditionally used to define translucent clouds. Furthermore, they found that many of these sightlines had strong H_2 absorption, with column densities $N(H_2) > 3 \times 10^{21}$ cm^{-2}, but none had the extreme molecular fractions ($f_{H_2} \geq 0.8$) which would be expected for molecular regions. This led them to conclude that these sightlines were not probing single translucent clouds, but rather a multitude of more diffuse ISM gas clouds with each contributing some component of the total absorption profile.

1.4.4. *Hubble Space Telescope*

The current state-of-the-art technology for UV absorption studies is the *Hubble Space Telescope* (*HST*). Since its launch in 1990, *HST* has continuously represented the largest aperture (2.4m) available for UV spectroscopy. Two scientific instruments on board *HST* are of particular note to ISM spectroscopy: the Goddard High Resolution Spectrograph (GHRS) and the Space Telescope Imaging Spectrograph (STIS).

On board the telescope from its launch, GHRS was capable of providing high-resolution UV echelle spectra ($R = \lambda/\Delta\lambda$ up to 95,000) for relatively narrow wavelength bandpasses (∼5-17 Å, depending on the specific echelle mode used), limiting its ability to simultaneously study the absorption profiles of multiple species. This problem was resolved during the second *HST* Servicing Mission in 1997, when the Space Telescope Imaging Spectrograph (STIS) was installed as replacement to GHRS, with echelle modes specifically designed to maximize the spectral coverage accessible in a single observation. STIS has since proven to be a workhorse for UV studies, providing medium- to high-resolution

(R∼110,000) echelle spectra in both the near- and far-UV (1150-3100 Å) with considerably broader bandpasses, ranging from 200 to 800 Å depending on the instrument setup[1]. As observations taken with the STIS instrument are a critical component of this work, the technical details of STIS and the data obtained with it are discussed in detail in §2.2.

Observations with *FUSE* were routinely combined with *HST* observations to fully explore the ultraviolet regime. In particular, several near-simultaneous studies in the late 2000's – Burgh et al. (2007), Sonnentrucker et al. (2007), and Sheffer et al. (2008) – coupled *FUSE* observations of H_2 with high-resolution *HST* STIS observations of CO in order to probe the CO-to-H_2 ratio, with the aims of better understanding the relationship between these two key molecules and better informing the use of CO as a tracer for H_2. These studies varied in their methodology, with Sheffer et al. (2008) and Sonnentrucker et al. (2007) building cloud-component models of the absorption profiles, as opposed to using the apparent optical depth and curve-of-growth methods used in Burgh et al. (2007), which are susceptible to saturation effects that limit their ability to accurately estimate column densities.

These studies found large variations in the observed CO/H_2 ratio. Sonnentrucker et al. (2007) reported values ranging from 2.5×10^{-8} to 2.8×10^{-5}, noting that the variation arose primarily from differences in N(CO). Similar conclusions were drawn from Burgh et al. (2007) ($CO/H_2 \sim 10^{-7}$ – 10^{-5}). Sheffer et al. (2008) attempted to quantitatively derive a power law relation between the two, $N(CO) \propto N(H_2)^{\beta}$. Their results indicate a broken power-law relationship, with $\beta \sim 1.5$ for log $N(H_2)$ values below ~ 20.4, with a steeper relationship ($\beta \sim 3.1$) at high H_2 column densities. This yielded CO/H_2 values

[1] `http://www.stsci.edu/hst/stis/documents/handbooks/currentIHB/stis_ihb.pdf`

ranging between 2.6×10^{-8} and 2.1×10^{-5}, which are consistent with the previous works. They attribute this broken power law to different CO production paths, with $CH^+ + O$ being important at lower column densities, and $C^+ + OH$ being the primary production path at the higher end of the power law. Taken as a whole, it is clear that the CO/H_2 in this regime varies quite dramatically from the canonical 10^{-4} used to determine H_2 from radio observations of CO in dense clouds.

As a follow up to Burgh et al. (2007), Burgh et al. (2010) incorporated measurements of neutral carbon C I into their analysis of CO and H_2, building on the Snow & McCall (2006) conclusion that the carbon content is an important determinant of whether a cloud is diffuse and translucent. Importantly, they found a correlation between the CO/H_2 ratio and the CO/C I ratio, and used this relationship to propose a new observational distinction between diffuse and translucent clouds of $CO/H_2 = 10^{-6}$ and CO/C I = 1. This is in opposition to the traditional definition based on the visual extinction, where the transition to translucent material occurs at $A_V \sim 1$. They argue that this definition is more physically motivated, as they found no correlation in their sample between A_V and the physical or chemical properties of the sightline. Measurements of CO and C I, both accessible within the STIS wavelength regime, can thus be a valuable probe of translucent and molecular material without necessitating the incorporation of direct measurements of H_2 from other instruments such as *FUSE*.

First investigated by Jenkins & Shaya (1979) using *Copernicus*, the detailed study of gas thermal pressures became feasible due to the large bandpass capabilities of STIS. This technical advancement enabled the simultaneous analysis of numerous C I absorption multiplets, allowing for better de-convolution of blended profiles as well as better correction

for saturated absorption. Jenkins & Tripp (2001) performed the first large-scale study of 21 Galactic sightlines using the high-resolution mode of STIS. Their observations consisted of determining the fraction of C I in the first fine-structure excited state, denoted f_1, and the fraction of C I in the second excited state f_2. Expected outcomes of these values are plotted in Figure 1.4.

These plots have a distinctive shape to them: as the gas pressure increases and collisions between carbon and hydrogen atoms become more likely, the populations of both the C I* and C I** states increase in a roughly linear fashion. As the pressure continues to increase, these collisions become so common that electrons still in the C I* can be further excited into the C I** state, thus reducing f_1 in favor of increasing f_2. Jenkins & Tripp (2001) found that most values tend to lie in the space just above the low pressure linear regime of this curve, near the location of the large Maltese cross in Figure 1.4. It was determined that the observed values represented an admixture of gas at low pressures and high pressures, with the exact location of the final value determined by the relative amounts of each. They thus concluded that there must exist a small but pervasive component of the ISM with large gas pressures $p = knT$, where k is Boltzmann's constant, n is the local number density, and T is the gas temperature. Because of this, they concluded that interstellar turbulence must create small-scale, short-lived, compressed (i.e. highly pressurized) structures within the ISM.

This study was expanded upon by Jenkins & Tripp (2011), who studied 89 sightlines and found a similar distribution of thermal pressures. The vast majority of the gas has p/k between 10^3 - 10^4 cm^{-3} K, with a small fraction ($\sim$5%) of the gas having $p/k > 10^{5.5}$ cm^{-3} K. While this study acknowledged that turbulence is an attractive option

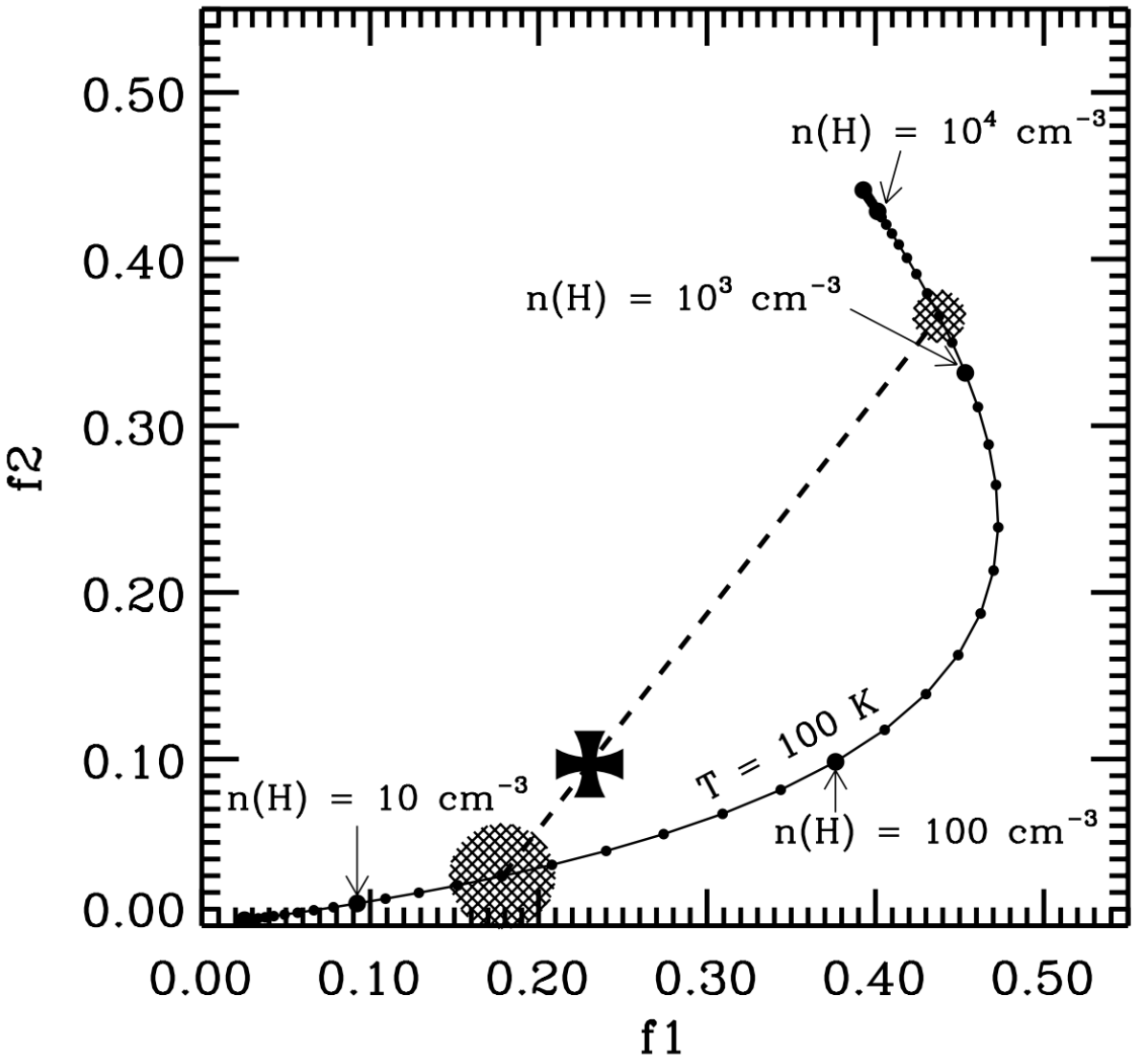

Figure 1.4. Figure 5 from Jenkins & Tripp (2001). Theoretical values of f_1, f_2 for gas with $T = 100$K and varying number density, indicated by the annotations. The large cross represents a typical value determined by the STIS observations, and is taken to represent an admixture of pressures from two parcels of gas – one large parcel at relatively low number density (and thus lower pressure) represented by the large cross-hatched region, and a smaller parcel at high density (and thus high pressure) represented by the smaller cross-hatch.

to explain these small pockets of extreme pressure, they note that the mass fraction observed in this regime is smaller than expected from theoretical modeling (Godard et al. 2009). Furthermore, they note that their results suggest a single distinct high-pressure component, rather than a continuous distribution in pressures as might be expected from a turbulent cascade.

1.5. The *Planck* Catalogue of Galactic Cold Clumps

In an attempt to characterize the population of potential star-forming gas in the Milky Way, the scientific collaboration behind the *Planck* satellite (Planck Collaboration et al. 2011a) have released a series of catalogs describing sources of cold dust emission detected during the *Planck* mission (Planck Collaboration et al. 2016a). The final, most extensive of these catalogs was the *Planck* Catalogue of Galactic Cold Clumps (PGCC) (Planck Collaboration et al. 2016b). The data within this catalog is described in detail in §2.1. Derived from the Galactic foreground dust maps extracted from the full mission data, this catalog represents an unbiased, all-sky census of 13,188 sources of cold dust emission. According to Planck Collaboration et al. (2016b), the broad range of sizes and number densities represented in this catalog indicate that it covers a variety of astrophysical sources and evolutionary stages, and thus represents a rich dataset with which to probe the earliest phases of star formation.

The gas content of these sources has been studied in detail using radio surveys, beginning with Wu et al. (2012) who surveyed 674 sources from the Early Cold Core (ECC) Catalogue (Planck Collaboration et al. 2011b) using the 13.7m telescope at the Purple Mountain Observatory in China (the ECC was a precursor to the PGCC based on the

first two passes across the entire sky instead of the five sky passes that comprise the full mission data, and contained only the most robust detections of cold clumps, many of which eventually overlapped with sources detected the PGCC). Wu et al. (2012) found that the emission line velocities of CO and two of its isotopes (^{13}CO and C^{18}O) agreed remarkably well across their entire sample, indicating that these sources were relatively uniform and did not exhibit dynamical structure, nor did they have complex thermal or chemical structure. They also measured the gas kinetic temperature T_k and compared it to the dust temperatures T_d derived by Planck Collaboration et al. (2011b) for the ECC sources. They found that $T_d > T_k$ for 95% of the studied sources, indicating that the gas is heated by collisions with dust, and therefore the dust and gas are generally well-coupled within these sources. This is a critical result for the prospects of using radio and ultraviolet methods (which are sensitive to the gas content of the ISM, as opposed to the dust) to investigate these sources that were detected via their dust emission.

More recent studies include Yuan et al. (2016), who focused on dense gas tracers such as HCO$^+$ and HCN. They surveyed 621 PGCC sources (also using the Purple Mountain Observatory) and detected 230 sources in HCO$^+$ and 138 in HCN. Based on these rates of detected dense gas tracers, they estimate that roughly 1,000 PGCC sources (out of 13,188 in the catalog) currently contain enough dense gas to form stars. The largest survey to date of PGCC sources was conducted by Liu et al. (2018), which surveyed ∼2,000 PGCC sources using a combination of data from the 14m telescope at the Taeduk Radio Astronomy Observatory in South Korea and the SCUBA-2 instrument on the James Clerk Maxwell Telescope in Hawaii. This study was intended to probe a sample that was representative of the entire PGCC catalog, yet was nonetheless biased toward higher

column density sources in an effort to ensure detection via radio follow-up. While results from the entire survey have yet to be released, potential science results were detailed for one example source, including detailed mass estimates, detection of substructure, and determination of the dense gas fraction within the source.

All of the above studies utilized various observations of emission from molecular gas tracers at radio wavelengths. While these specific tracers are a powerful tool to study dense gas, even CO (the most common observable molecular gas tracer) is only detectable via radio emission when $N(CO) \gtrsim 10^{15}$ cm^{-2} (Liszt 2007). Because of this detection limit, the vast majority of these follow-up studies are biased toward the densest PGCC sources, rather than probing a sample that is representative of the entire PGCC population.

Based on the $N(H_2)$ estimates listed in the PGCC catalog, a large number of these sources would be classified as "diffuse molecular" or "translucent" in nature, as defined in Figure 1.1. Figure 1.5 compares the $N(H_2)$ distribution of the entire PGCC catalog to radio studies that specifically targeted PGCC sources for follow-up observations, as well as the distribution of $N(H_2)$ for PGCC sources probed by this study. Radio studies are unsurprisingly biased toward dense molecular sources with $N(H_2)$ above a few $\times 10^{21}$ cm^{-2}, which only represent a fraction of the total source catalog and is not representative of the entire PGCC source distribution. For all sources with a measured $N(H_2)$, the mean $N(H_2)$ is $\sim 1 \times 10^{21}$ cm^{-2} and the median is $\sim 4 \times 10^{20}$ cm^{-2}. As such, there is clearly a wealth of sources that would not be expected to have enough molecular content to be detectable via CO emission. Thus, complementary observations capable of studying more diffuse molecular environments are necessary in order to fully understand the entire PGCC catalog, and thus the entire population of molecular gas in the Milky Way.

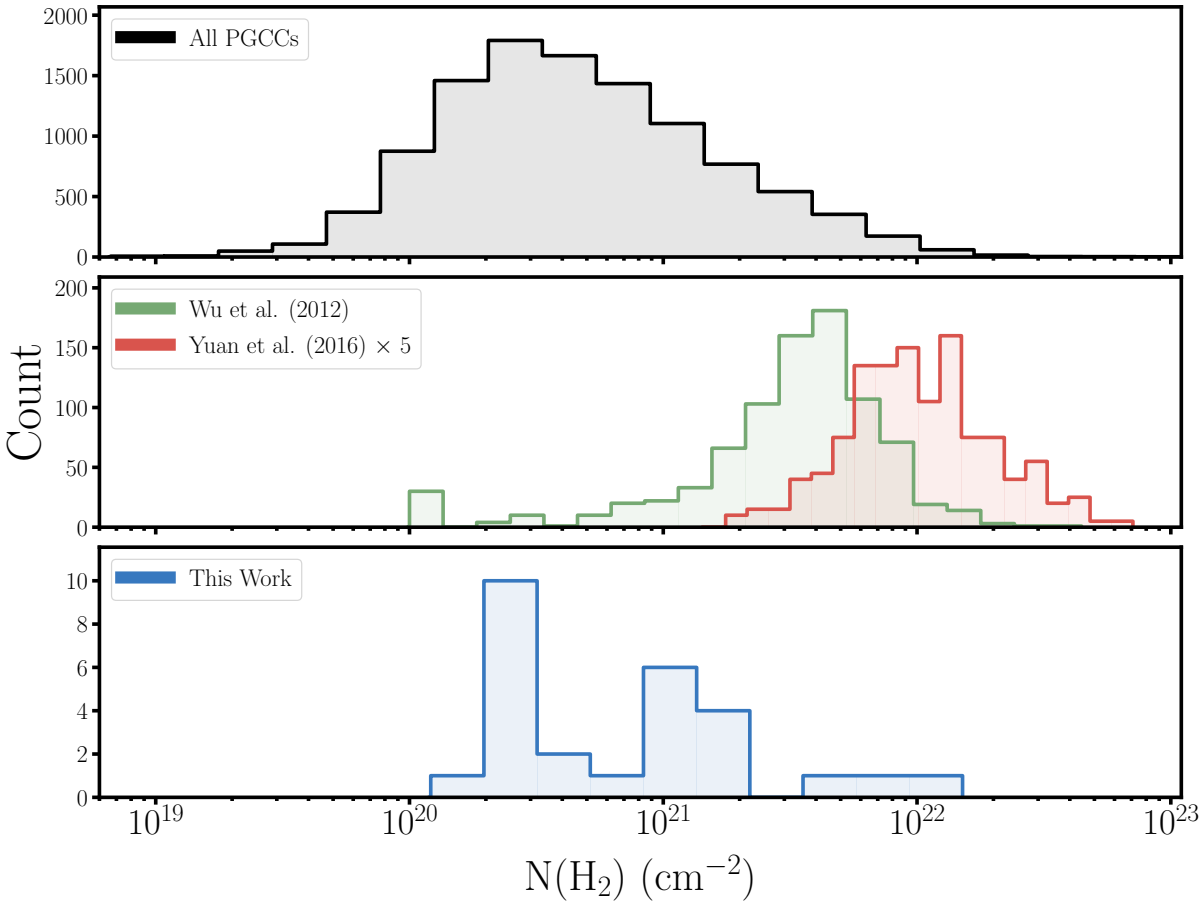

Figure 1.5. Comparison of previous PGCC studies. *Top:* Distribution of $N(H_2)$ for all sources in the PGCC catalog for which $N(H_2)$ could be determined (10,792 out of 13,188 total sources). *Middle:* Distribution of $N(H_2)$ for two follow-up studies that used radio surveys to follow-up on PGCC sources. *Bottom:* Distribution of $N(H_2)$ for PGCC sources determined to have absorption-line targets behind them.

1.6. Outstanding Questions

The paradigm of a multi-phase ISM, with a hot diffuse volume-filling phase, a cold dense star-forming phase, and a transitionary "diffuse molecular" or "translucent" phase that bridges the two extremes is well-established. The details of this transitionary phase,

and exactly how it occurs, are still unclear due to the combination of a lack of observational data focusing on the regime, and inconsistency in theoretical modeling of these photodissociation regions.

What physical properties define this transition, and what drives gas to move from a diffuse state to a dense state? As the PGCC sources are identified as discrete objects, does this imply that this transition is associated with specific structures within the ISM? The ISM has long been known to have a variety of different structures within it, from the large-scale expanding hydrogen shells first illustrated in McKee & Ostriker (1977), to the H I and cold neutral medium "sheets" described by Heiles & Troland (2003), to the presence of filamentary structures within star-forming regions Schneider & Elmegreen (1979); André et al. (2014).

To address these questions, it is critical to obtain more observations of translucent and molecular gas in this transitionary regime. Such observations will link observable parameters (such as molecular column densities, isotope ratios, and dust depletion parameters, among others) to this transition, as well as place this regime in context of both the more diffuse and more dense regimes. These observables can also be compared to predicted values from simulations of photodissociation regions, placing more stringent constraints on the physical parameters used to define these models. To achieve this, it is critical to employ data analysis techniques that best capture the local ISM conditions within these regions. This requires isolating the absorption components arising from the gas of interest, rather than convolving all observed absorption along the sightline. This will allow for better characterization of the gas associated with these sources.

In order to achieve these goals, this work aims to identify a sample of sightlines which probe translucent gas and study them via absorption-line spectroscopy. This sample is generated by combining the UV observational capabilities of *HST* with the PGCC source catalog, which represents an excellent foundational source catalog with which to inform targets of observation. The nature of these PGCC sources is such that they represent a broad range of physical parameters. Many of the PGCC sources in the catalog have estimated $N(H_2)$ values in the "diffuse molecular" and "translucent" regimes defined by Snow & McCall (2006) and shown in Figure 1.1. Additionally, the PGCC catalog almost certainly cuts across multiple types of structure, with many sources in the catalog described as elongated and evocative of filamentary structure (Planck Collaboration et al. 2016b). Sources are also often clustered together spatially, indicating that they represent smaller sub-cores within a single larger molecular cloud complex, such as the 51 PGCC sources within the Orion complex studied by Liu et al. (2012). Thus, the PGCC catalog represents a rich testbed by which to probe this transition in ISM density as well as the role of structure within this transition.

To our knowledge, no prior work has been done to specifically target the environments of PGCC sources using UV absorption-line spectroscopy. Such a study will be extremely useful in understanding the ISM within this regime, as UV spectroscopy is capable of probing a range of PGCC molecular column densities that is more representative of the inherent distribution observed by *Planck* (Figure 1.5). Furthermore, such observations are sensitive to CO column densities that are $\sim$2 orders of magnitude below the detection limit of typical radio emission studies of CO, as well as being sensitive to considerably smaller scales than the *Planck* observations. These differences between the observational

methods mean that UV spectroscopy is capable of probing a broader range of physical conditions. While many of the sightlines included in this work are well-known interstellar absorption sightlines that have been studied extensively, these were often either isolated studies of individual targets of interest, or part of larger all-sky surveys which combined observations that probed a wide range of ISM conditions ranging from diffuse to dense regions of the ISM. The presence of a large, all-sky census of molecular material such as as the PGCC allows for the first time a large, targeted study of this regime of the ISM.

CHAPTER 2

Data Selection Process

2.1. The *Planck* Catalogue of Galactic Cold Clumps

The genesis of this work was the *Planck* Catalogue of Galactic Cold Clumps (PGCC), which was compiled and released as part of the *Planck* science teams' final data release in 2015 (Planck Collaboration et al. 2016b). The *Planck* mission collected sub-millimeter emission data across the entire sky for a broad frequency range (100 – 857 GHz) with a resolution of $\sim 5'$. This emission arose from both Galactic and extra-galactic sources, prompting the *Planck* team to separate the raw data into an extra-galactic component to be used in cosmological studies, and a foreground component primarily composed of thermal dust emission from the Galactic ISM. In order to identify the presence of cold dust in the ISM, the *Planck* team isolated the observational bands closest to peak of the Galactic cold dust emission (the 353, 545, and 857 GHz frequency bands) and compared them to a reprocessed version of IRAS 3 THz data (Miville-Deschênes & Lagache 2005). This 3 THz data traces $\sim$20K warm dust, and thus convolving these two datasets should allow for the identification of "cold spots" in the combined map that specifically arise from cold dust emission.

In order to identify all such spots, a detection algorithm (CoCoCoDeT; Montier et al. 2010) was applied to this map to generate a catalog of sources. This algorithm begins by extrapolating the warm dust map to the frequency of a given *Planck* band. This warm

component is then subtracted from the raw *Planck* data in that band, with any residuals thus arising from dust colder than that which is present in the 3 THz data. CoCoCoDeT then searches for sources that are coincident across each of the three residual maps. The resulting catalog consists of 13,188 Galactic sources, which are primarily concentrated within $\sim 10^{\circ}$ of the Galactic Plane. Due to the variety of distances and angular sizes for these detected sources, their inherent physical sizes range from small, compact cores a few tenths of a parsec in size, up to giant molecular cloud scale objects hundreds of parsecs across.

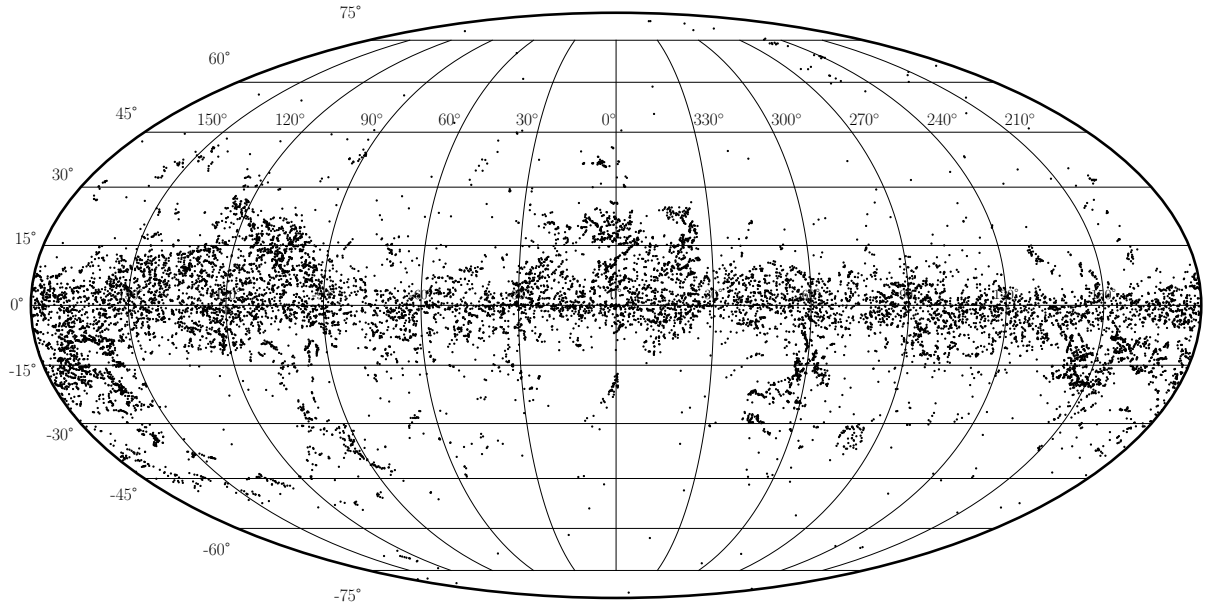

Figure 2.1. Map of all PGCC sources listed in the catalog in Galactic coordinates. Many sources are clearly associated with the Galactic plane. Additionally, many well-known molecular cloud complexes are visible as structures within this distribution.

2.1.1. Source Sizes

For source detected in all three *Planck* bands (353, 545, and 857 GHz), a two-dimensional elliptical Gaussian fit is performed to the residual map determined by differencing the 857 GHz map and the extrapolated IRAS 3 THz map. This fit yields a source location (given as the latitude/longitude of the center of the 2D Gaussian), major and minor axes (σ_{maj}, σ_{min}) and the resulting ellipticity, defined as

$$\epsilon = \sqrt{1 - \left(\frac{\sigma_{min}}{\sigma_{maj}}\right)^2}. \tag{2.1}$$

A source orientation, defined to be the position angle between the major axis and the Galactic Plane, is also included in the catalog. A distribution of the observed angular sizes is shown in Figure 2.2.

2.1.2. Source Distances

A critical component of conducting absorption line studies of the ISM is verifying that the absorption sightline is actually probing the gas of interest. Therefore, in this study we must compare the stellar distance to the PGCC source distance. A variety of estimators were used to derive distances for 5,574 of the 13,188 sources (The remaining 7,614 sources simply have no distance information given in the catalog). Here we briefly describe each method used. A summary of the number of sources whose distance was determined using each method is shown in Table 2.1. More detailed methodology and further references can be found in Planck Collaboration et al. (2016b).

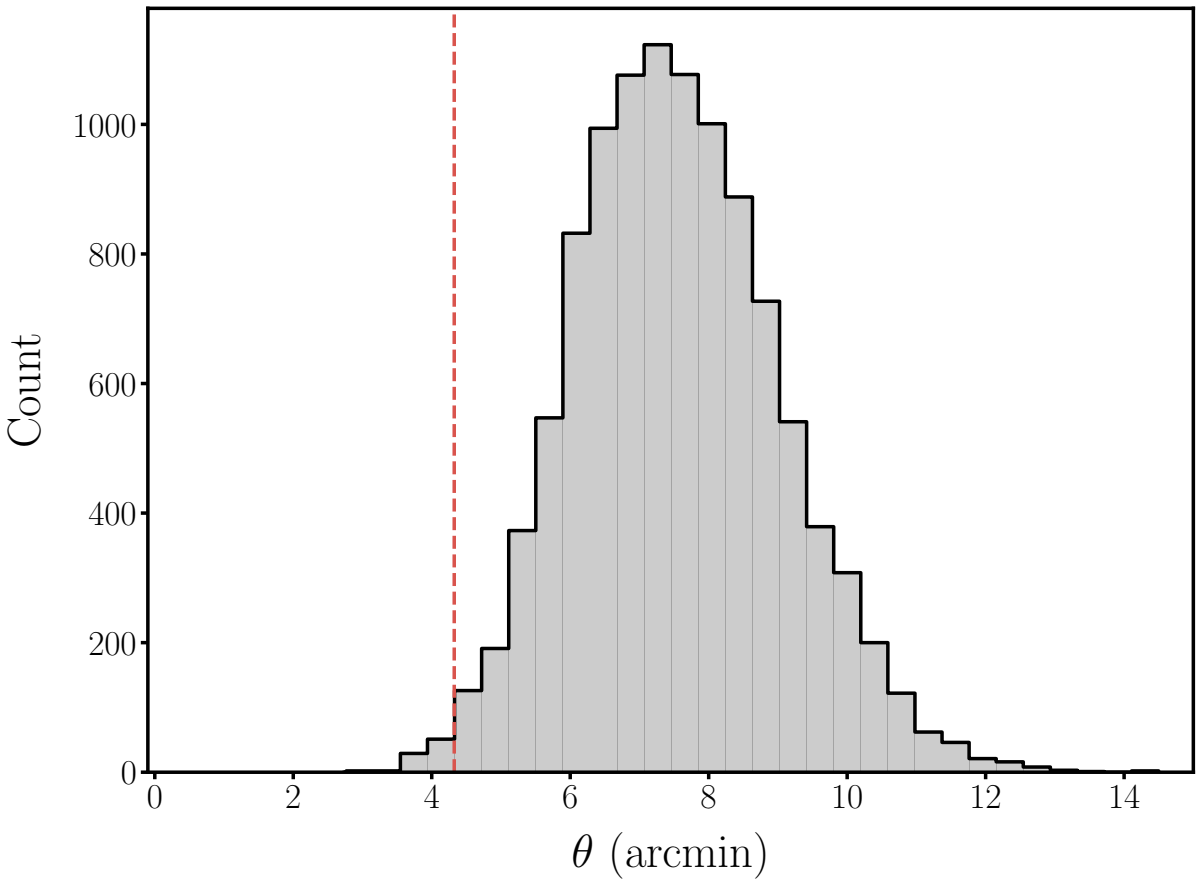

Figure 2.2. Distribution of angular sizes for all PGCC sources for which an angular size could be determined (10,748 out of 13,188 sources). The x-axis, θ, is defined as $\sqrt{\sigma_{maj}\,\sigma_{min}}$. The FWHM beam size of the *Planck* 857 GHz beam (4.3 arcmin) is denoted by the vertical dashed red line.

- Kinematic Distances – By combining a Galactic rotation model with the observed radial velocity of the gas associated with the source, one can derive values of distance for which the modeled 3D motion would yield the observed radial (i.e. 1D) velocities. For Galactocentric distances beyond the Solar circle, this solution is single valued, while Galactocentric distances within the Solar circle yield two possible solutions. In these cases, the *Planck* team always chose the nearer of

the two possible solutions. Errors of 25% were assigned to distances determined using this method.

- Optical Extinction – Using Sloan Digital Sky Survey (SDSS) photometry data of stars with known distances in the sky vicinity of each PGCC source, the optical extinction toward each star can be determined. Since the distances to these stars is known, the optical extinction as a function of distance can be determined, and the location of the cold, dusty gas associated with the PGCC source (which would be expected to contribute heavily to the optical extinction) can be determined. This procedure was done using two independent SDSS datasets, one based on SDSS DR7 and one based on SDSS DR9. Uncertainties in the derived distances are determined using Markov Chain Monte Carlo (MCMC) methods, in which 100 realizations are calculated and the resulting distribution of derived distance yields an estimation of the uncertainty.
- Near-Infrared Extinction – In a similar manner to the optical extinction method described above, near-infrared photometric data can be used to determine the dust distribution along the line of sight. This was done using two difference NIR catalogs: the IRDC catalog (Simon et al. 2006) and the Two Micron All Sky Survey (Skrutskie et al. 2006, 2MASS). Peaks in the dust density distribution greater than 3σ are flagged. Uncertainties are again determined via an MCMC method with 10^5 realizations.
- Molecular Complex Association – Many PGCC sources appear to lie in the vicinity of well-known, previously studied molecular cloud complexes. By comparing the sky coordinates of PGCC sources to CO emission maps within 11 of these

complexes, it can be determined if a source is associated with the complex and thus shares a common distance. The 11 molecular complexes were chosen to lie outside of the Galactic plane to minimize the effects of confusion between unrelated, overlapping sources.

- Herschel Follow-Up – Selected PGCC fields were targeted for follow-up observations using the *Herschel Space Observatory*. In particular, targets which were previously well-studied in the literature were chosen (Montillaud et al. 2015).

Table 2.1. PGCC Source Distance Methods

Method	Total	Best
Kinematic	92	23
Optical Ext. (DR7)	1083	719
Optical Ext. (DR9)	191	173
NIR Ext. (IRDC)	182	106
NIR Ext. (2MASS)	2810	2491
Molecular Complexes	1895	1834
Herschel Follow-up	228	228
Total	6481	5574

Adapted from Planck Collaboration et al. (2016b) Table 4. Various methods used to estimate distances to PGCC sources. "Total" refers to the total number of sources in the catalog for which the given method provides a distance estimate. "Best" refers to the number of sources for which the given method provided the most confident estimate of the source's distance.

2.1.3. Molecular Hydrogen in PGCC Sources

For many sources within the PGCC catalog, the *Planck* team was able to determine the molecular hydrogen column density, $N(H_2)$. These $N(H_2)$ estimates are derived based on the observed cold dust emissivity in these sources. This method is described in detail

in Planck Collaboration et al. (2011b), which detailed a precursor catalog to the current PGCC. To determine the cold dust emissivity, the *Planck* team compared their observed dust emission at 857 GHz to data from the InfraRed Astronomical Satellite (IRAS), which observed at 3 THz and thus is sensitive to warmer dust, as the blackbody emission for this higher temperature dust will be shifted to higher frequencies. By extrapolating this blackbody emission to the *Planck* 857 GHz band and subtracting this warm dust emission component observed by IRAS from the *Planck* dust emission, the contribution from the cold dust can be isolated and studied. This cold dust emissivity S_ν is then used to fit a blackbody curve of the form

$$S_\nu = \Omega_c \, \kappa_\nu \, B_\nu(T) \, N(H_2) \, \mu \, m_H \tag{2.2}$$

In this equation, Ω_c represents the solid angle covered by the detected source,

$$\Omega_c = \pi \, \sigma_{maj} \, \sigma_{min}, \tag{2.3}$$

κ_ν represents the dust opacity as a function of frequency from Beckwith et al. (1990),

$$\kappa_\nu = 0.1 \, \left(\frac{\nu}{1\,\mathrm{THz}}\right)^2 \mathrm{cm}^2 \, \mathrm{g}^{-1} \tag{2.4}$$

$B_\nu(T)$ is the classical Planck blackbody function expressed in terms of frequency,

$$B_\nu(T) = \frac{2\,h\,\nu^3}{c^2} \frac{1}{e^{\frac{h\nu}{k_B T}} - 1} \tag{2.5}$$

and μ and m_H are physical constants representing the mean molecular weight of H_2 and the mass of atomic hydrogen, respectively.

With this framework, the *Planck* team used the 857 GHz emission band as an input map into the above equations. This yielded an analogous N(H_2) map which was then integrated over the source region to find a single "average" value for each source. These are the values (and associated errors) that are reported in the PGCC catalog.

The nature of the detection algorithm used in the source identification and extraction process requires the input *Planck* dust emission maps and the IRAS 3 THz background map to be convolved to the same angular resolution – in this case, a FWHM value of 5′. This implies a minimum angular size over which these N(H_2) estimates are valid. This corresponds to a physical size of ∼0.15 pc for nearby (∼100 pc) PGCC sources, and ∼15 pc for sources at the furthest (∼10 kpc) distances listed in the catalog. Because of this angular resolution, PGCC sources have typical σ_{maj}, σ_{min} values of ∼5-10′ and thus their N(H_2) estimates represent averages of dozens to hundreds of square arcminutes on the sky.

2.2. *HST* STIS Spectra

The STIS instrument aboard *HST* is an extremely versatile instrument for studies in the ultraviolet. STIS contains three separate detectors: a charge-coupled device (CCD) chip and two Multi-Anode Microchannel Arrays (MAMAs). Each of these detectors has a 1024×1024 array of pixels and are capable of both imaging and spectroscopy. Of the two MAMA detectors, one (STIS/NUV-MAMA) was designed for near-UV observations between 1600-3100 Å range, while the other (STIS/FUV-MAMA) was designed for far-UV observations between 1150-1700 Å. Here we will focus exclusively on spectroscopic observations taken with the STIS/FUV-MAMA detector, whose wavelength coverage covers a

vast array of interstellar spectral lines, in particular CO, C I, O I, Kr I, Ni II, Ge II, and Mg II. Section 3.3 details the utility of each of these specific species as they relate to this work. In addition to the choice of detector, a variety of other instrumental settings must be chosen for any individual observation. Each of the NUV- and FUV-MAMA detectors have separate medium- and high-resolution grating modes at R $\sim$ 30,000 or 114,000 (corresponding to $\sim$10 km s^{-1} and $\sim$2.5 km s^{-1} resolutions in velocity space). These gratings are denoted as E140M and E140H in the FUV (due to the FUV-MAMA detector being centered on 1400 Å) and as E230M and E230H in the NUV (due to the NUV-MAMA detector being centered on 2300 Å). Furthermore, the entire dispersed echelle spectrum is too large to fit onto a single MAMA 1024×1024 array, thus necessitating the specification of a central wavelength for each observation, which identifies which subset of the entire wavelength range will be captured. An illustration of this is shown in Figure 2.3. This limitation results in each STIS exposure only capturing a $\sim$200 Å section of the entire 1150-1700 Å domain accessible to the STIS/FUV-MAMA detector.

An example raw STIS FUV-MAMA exposure is shown in Figure 2.4. Raw images such as these are processed using the `calstis` pipeline developed and maintained by the Space Telescope Science Institute (STScI), which is responsible for overseeing the science operations for *HST* (as well as many other space-based observatories). This pipeline allows for the output of a number of different types of data files, depending on the input parameters. Relevant for this work will be X1D files, which contain a series of one-dimensional spectra extracted from each of individual spectral orders present in the raw image. `calstis` is described in detail in the STIS Data Handbook[1], but the general

[1] `http://www.stsci.edu/hst/stis/documents/handbooks/currentDHB/stis_dhb.pdf`

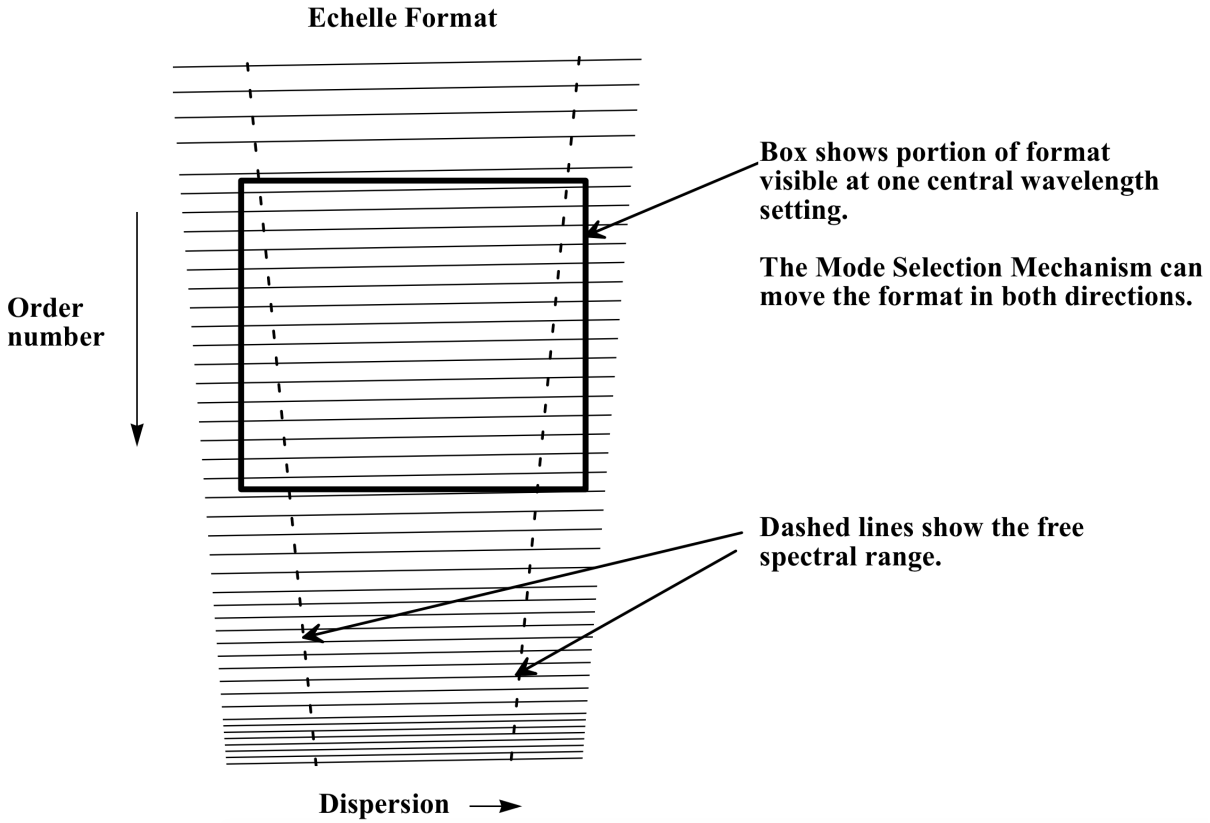

Figure 2.3. Figure 4.5 from the STIS Instrument Handbook. Illustration of the subset of the entire echelle spectrum captured by a single specification of the central wavelength setting.

outline of the processing pipeline used to generate these X1D output files from the raw science observations is summarized below.

(1) Initial Quality Check and Binning – The raw science image is checked against a known bad pixel mask, and information about the data quality of individual pixels is stored in a separate reference file. The science data is then binned to 1024×1024 resolution. While the STIS MAMA detectors have a native 1024×1024 resolution, the data is actually recorded in a high-resolution 2048×2048 mode – this is because each pixel contains multiple electrodes and thus the observed charge

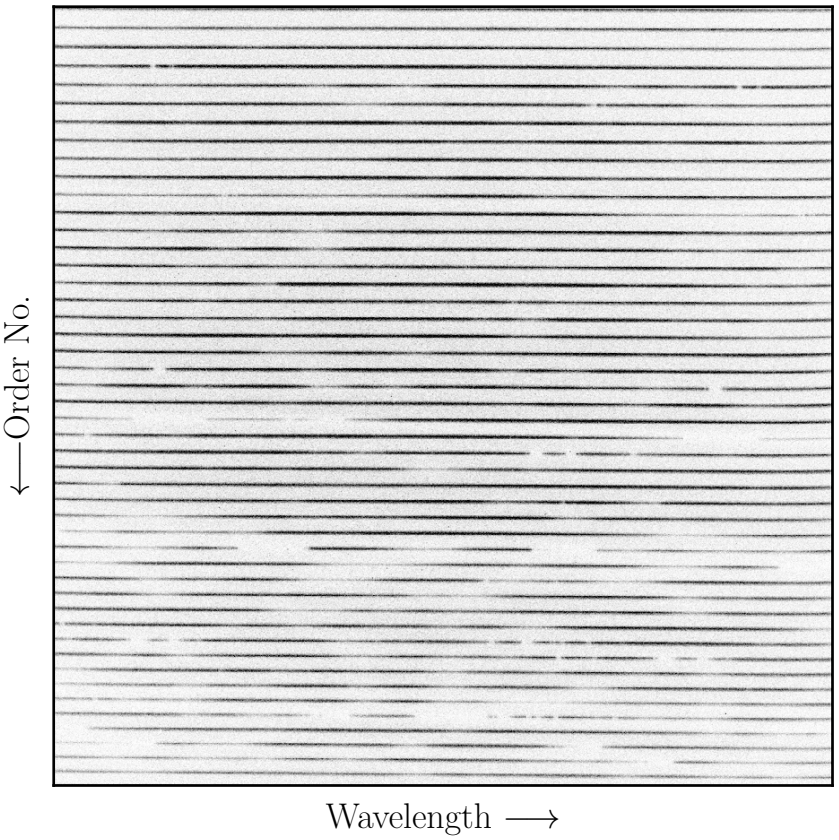

Figure 2.4. Raw STIS/FUV-MAMA detector image resulting from a 4,250 second exposure toward the star HD 4768, taken with the E140H grating mode at a central wavelength of 1343 Å. In this representation, darker shading indicates more detected counts. Clearly visible are the multiple orders of the dispersed echelle spectrum, as well as gaps within the individual orders indicating absorption. This particular exposure covers the wavelength range 1243 Å - 1445 Å.

distribution can be resolved at the subpixel level. However, because the subpixel electrode partitioning is poorly understood, and because the higher-resolution flat fields are observed to have much more structure, these high-resolution images are commonly binned back down to the native 1024×1024 resolution during calibration.

(2) Global Linearity Corrections – MAMAs are designed to be raw photon counters, but at high count rates their response can become non-linear (i.e. they will no longer correctly log 1 "count" per photon). This is due to both local material effects (where depletion of electrons from high count rates is larger that the rate at which electrons can replenish) as well as global electronic effects (the design of the STIS hardware and software processing cannot handle count rates above $\sim$300,000 counts s^{-1}). Fortunately, the count rates where these non-linearities become substantial are larger than the allowed observing bright limits, so these corrections are typically very small. Any pixels identified to exhibit non-linear behavior are flagged.

(3) Dark Subtractions – Subtract "dark current," the count rate that is observed to persist even in the absence of any incoming sky photons. This effect is primarily due to thermal effects within the detector.

(4) Flat-Fielding – A flat-field image is constructed from multiple reference files that are specific to the chosen grating/filter/detector. These individual reference files represent large-scale, smooth variations across the detector, and small-scale fluctuations around these smooth variations. The scientific data is then divided against this flat-field image to normalize out these fluctuations.

(5) Scattered Light Correction - Due to the nature of echelle spectrographs, some incoming light will be scattered by the grating and contaminate unrelated parts of the spectral image. For the STIS echelle grating, this scattering primarily arises in two ways: detector halo scattering and inter-order echelle scattering. Both of these effects can be seen in Figure 2.5. To account for this, the STIS Instrument

Definition Team (IDT) developed a routine, SC2DCORR, to iteratively estimate the effects of this scattered light using the estimated true spectrum, laboratory measurements of the scattering properties of the echelle gratings, and measurements of the instrumental point-spread function (PSF) (Howk & Sembach 2000). Once this iterative process converges on a solution, the scattered light background is then subtracted from the flat-field data, and this combined background and flat-field data is used during subsequent spectral extraction.

(6) Extract 1D Spectra - Locations of the individual 1D spectra present in the images are determined using spectrum trace tables. Once the individual spectra have been isolated, they are then summed along the axis perpendicular to the dispersion axis. Backgrounds are estimated using two regions (one above the spectrum and one below), and then subtracted from the individual summed 1D spectra.

(7) Assign Wavelength - Assign wavelength values to each pixel along the dispersion axis using a dispersion solution which relies on coefficients derived from reference wavelength measurements. A further correction is applied to the calculated wavelengths to account for the Doppler shift arising from the motion of the Earth relative to the Sun at the time of observation.

(8) Assign Fluxes - Converts the detected count rate at each observed wavelength into physical units of flux. This conversion depends on both physical constants such as the speed of light c and Planck's constant h, as well as instrument specific factors such as the area of the *HST* mirror, aperture and grating throughputs, and time- and temperature-dependent correction factors. For echelle data, a

further correction is applied due to the time- and spatial-dependence of the blaze function.

It should also be noted that, due to the motion of *HST* as it orbits the Earth, a slight Doppler shift is induced onto photons entering the spectrograph. Thus, for MAMA spectroscopic observations (including those taken with the echelle gratings) a correction is automatically applied to the location of the incident photon along the dispersion axis at the time of arrival for each photon event. Subsequent data reduction procedures that apply to the entire two-dimensional image (such as the data quality checks, flat-fielding, and dark subtraction) are convolved with a Doppler smearing function that applies this correction to the entire reference image before it is then used as part of the data reduction pipeline.

2.2.1. The *HST* Data Archive

All previous *HST* STIS observations are stored in the Mikulski Archive for Space Telescopes[2] (MAST), a public archive that allows for the search and retrieval of past observational data. MAST allows for the retrieval of either calibrated or uncalibrated scientific data files. For this work, only the X1D data format output by the `calstis` pipeline was used. These data are stored as Flexible Image Transport System (FITS) files, a robust data format that allows for the storing and transport of complex, multi-faceted astronomical data. Each FITS file output by `calstis` contains header information general to the entire spectrum (typically concerning instrumental set-up used to define and execute the observation), as well as individual data tables for each of the extracted 1D spectra which

[2] `https://archive.stsci.edu/`

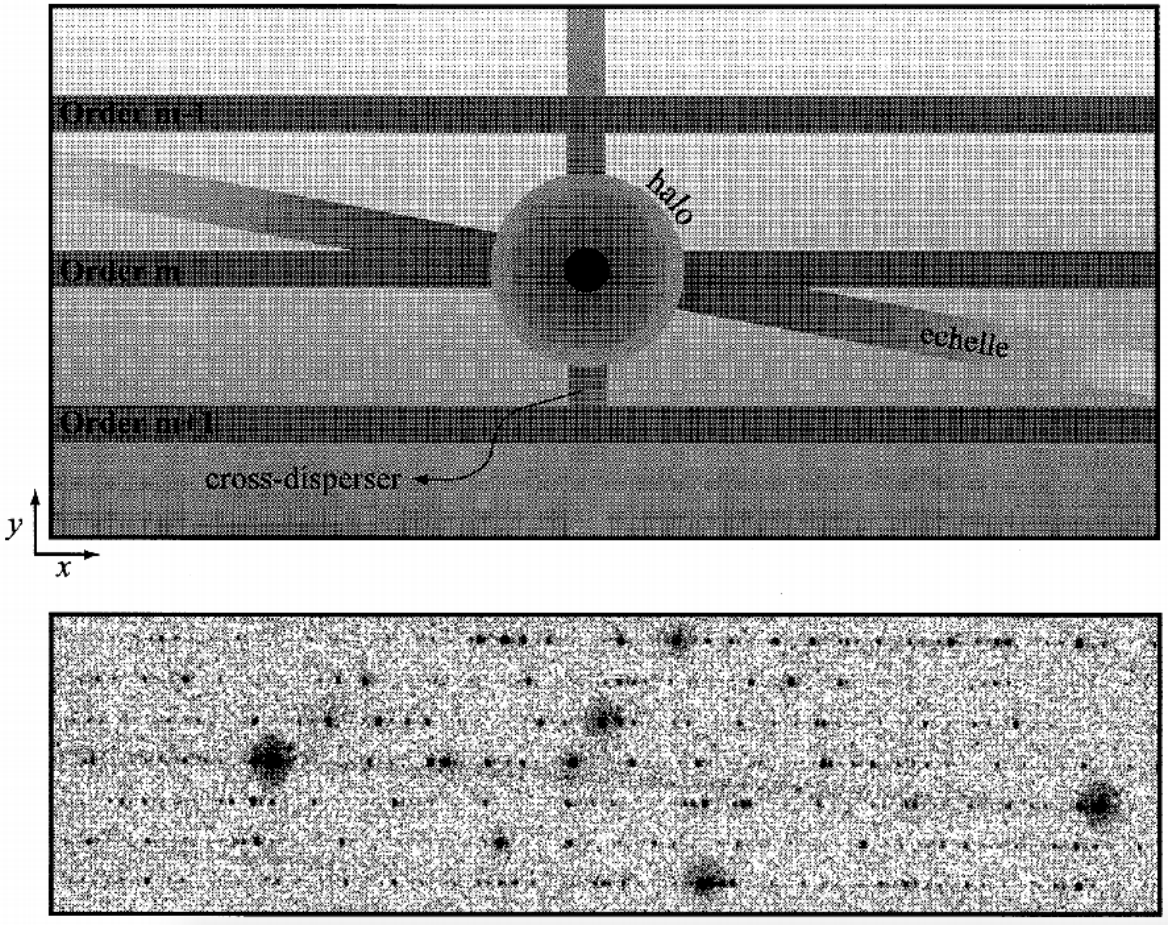

Figure 2.5. Figure 2 from Howk & Sembach (2000). Echelle scattering effects present in the raw 2D images taken with the STIS MAMA detectors. *Top:* Schematic diagram of the scattering effects. "Halo" refers to the large circular scattering around regions of bright flux. "Echelle" refers to the inter-order scattering present between bright flux in successive orders. *Bottom:* Cutout of a raw STIS MAMA E230H calibration lamp exposure. Large scattering haloes are seen around several bright emission lines, and a significant inter-order scattering band is seen stretching across the center of the image.

are stored as extensions within the FITS file. These tables contain separate columns for the wavelength array, flux array, and flux error array, as well as several others entries which will not be relevant here. §5.5.1 of the STIS Data Handbook (referenced in

the above section) details the structure of the X1D format, with each individual column present in each 1D spectrum's data table listed in Table 5.4 of that document. These data structures were parsed and accessed using the `astropy.io.fits` package, designed to allow for simple access to FITS data as well as easy integration of this data into other `astropy` and `Python` modules.

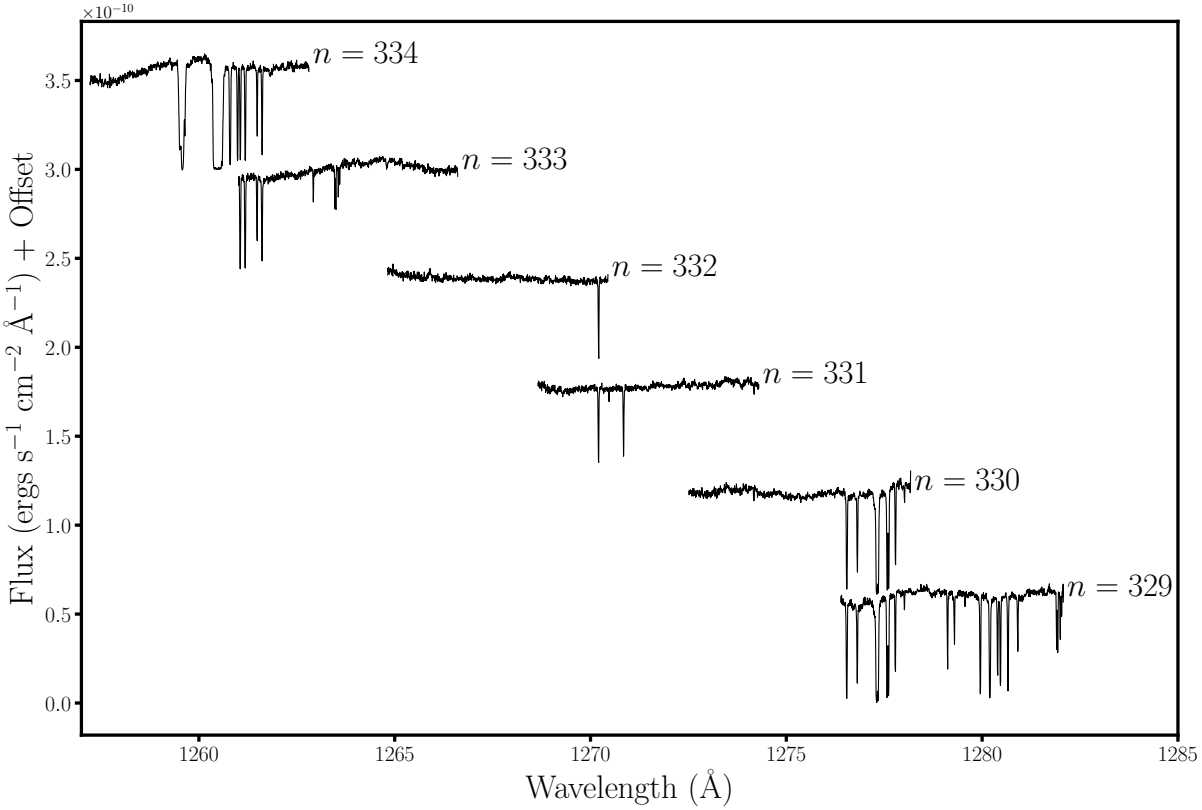

Figure 2.6. One-dimensional spectra extracted from the raw STIS/FUV-MAMA exposure. The corresponding echelle orders that give rise to each individual spectrum are noted. Clearly visible is the overlap in wavelength space between successive orders, allowing for the co-addition of individual orders to boost the signal-to-noise in a small range around of line of interest.

2.3. Combining *Planck* and *HST*

The goal of this project is to, for the first time, performed a targeted study of the cold dust ISM previously cataloged in the PGCC using the diagnostic power of UV absorption-line spectroscopy. To achieve this, this work aims to combine the PGCC and *HST* archive datasets described above to isolate sightlines probing gas associated with these sources. This can be done in an automated fashion by obtaining the coordinates of previous observations present in the *HST* archive, and checking the locations of these observations relative to all PGCC sources. While this may initially sound like a daunting task, a few well-motivated cuts can significantly reduce the size of each dataset, and thus reduce the computing time necessary to identify sightlines near PGCC sources.

Within the realm of the *HST* archive, the first major constraint was limiting the archival results to those that use the STIS E140H grating, which has only been used for ∼1,100 of the ∼98,000 STIS observations present in the archive. These results were limited even further by requiring that the target of the observation be a star, preferably an early-type OB star, as opposed to an extragalactic source or Solar System target. Due to inconsistencies in the target naming schemes or target classifications, this often necessitated cross-referencing the target identifiers and coordinates with the SIMBAD Astronomical Database[3] to confirm the nature of the target. Doing so for the full set of STIS E140H observations yields 267 unique suitable stellar targets. In an attempt to remain as consistent as possible throughout this work, Henry Draper (HD) catalog identifiers will be used.

[3] `http://simbad.harvard.edu/simbad/`

For the PGCC catalog, the first major constraint was to eliminate sources with no distance estimate, as this would make it impossible to verify that the absorption sightline was actually probing the gas of interest. Furthermore, targets for which no angular size could be determined were also eliminated, as this makes it impossible to determine if the sightline probed the central region of the source or the diffuse outer envelope. Lastly, a small number of sources that are flagged to be in either the Small or Large Magellanic Cloud were excluded. These cuts reduce the usable size of the PGCC catalog to 4,626 sources.

Having made the appropriate cuts, the process of finding absorption sightlines that lie near one of the remaining PGCC sources can begin. In order to account for variations in the size, shape and orientation of the PGCC sources, the separation between any given PGCC source and sightline is scaled by the σ_{maj} and σ_{min} parameters in the catalog. This is done by adapting the general equation for a rotated ellipse,

$$1 = \left(\frac{(x-h)\,cos(\theta) + (y-k)\,sin(\theta)}{a} \right)^2 + \left(\frac{(x-h)\,sin(\theta) + (y-k)\,cos(\theta)}{b} \right)^2 \tag{2.6}$$

where (a, b, θ) represent the semi-major axis, semi-minor axis, and rotation parameters of the ellipse, and (h, k) represents the location of the center of the ellipse. This equation yields all values of (x, y) that define the "1σ" boundary of an ellipse with the given parameters. One can also invert this problem – given an x, y which represents the coordinates of the sightline, the separation in terms of σ can be calculated. This can be visualized intuitively by taking the 1σ ellipse defined by the σ_{maj}, σ_{min}, and θ parameters in the PGCC catalog, and expanding this ellipse outward by some factor σ until it intersects the

sightline. Equation 2.6 can thus be re-written as

$$\sigma^2 = \left(\frac{\Delta l \, cos(\theta) + \Delta b \, sin(\theta)}{\frac{1}{2}\sigma_{maj}} \right)^2 + \left(\frac{\Delta l \, sin(\theta) + \Delta b \, cos(\theta)}{\frac{1}{2}\sigma_{min}} \right)^2, \tag{2.7}$$

where $(\Delta l, \Delta b)$ represents the separation in Galactic longitude and latitude, respectively, between the sightline and the center of the source, $(\sigma_{maj}, \sigma_{min})$ represent the source sizes along the major and minor axes, respectively (see §2.1.1), and θ represents the rotation of the PGCC major axis with respect to the Galactic plane. These parameters are shown visually in Figure 2.7.

Using this framework, all sightlines that fall within 10σ of a nearby PGCC source were identified. This value was chosen so that the outer, diffuse envelope that surrounds the molecular gas is also probed, and thus the entire transition from diffuse to molecular ISM is captured. Performing this cross-correlation of these two datasets yields 84 stellar sightlines deemed to lie near a PGCC source.

2.4. Determining Stellar Distances

Having isolated those sightlines which fall near PGCC sources on the 2D plane of the sky, the final step is to determine their relative locations in the third (distance) dimension to ensure that the absorption sightline is probing the gas of interest. This can be done via both direct and indirect methods, which are discussed individually below.

2.4.1. Direct Stellar Distances using *Gaia*

To determine their relative distances, PGCC source distances listed in the catalog were compared to stellar distances computed from measurements of their observed parallax.

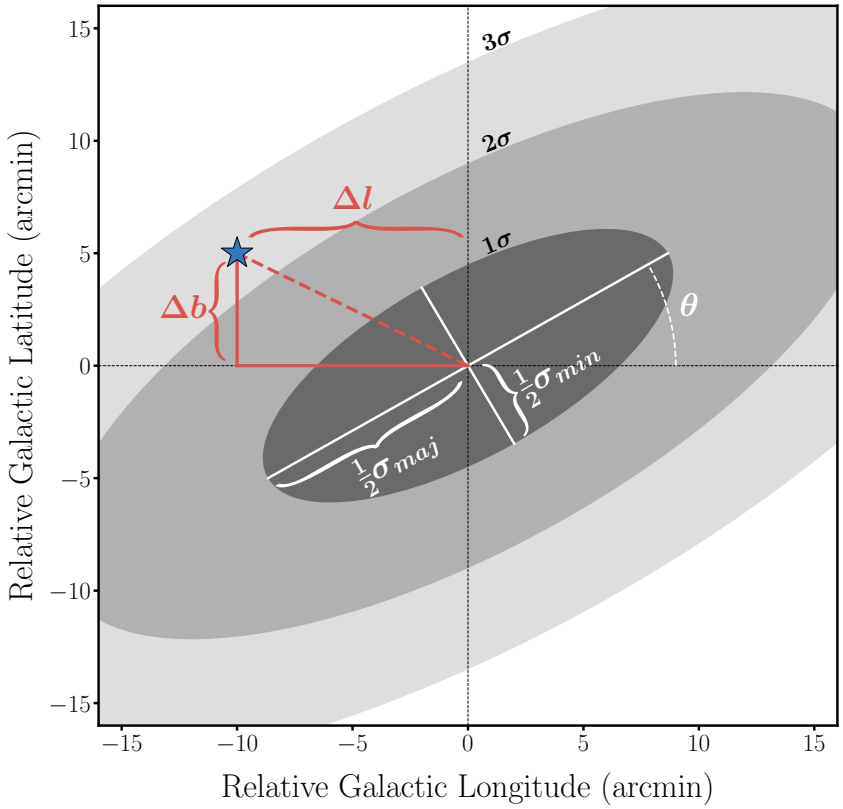

Figure 2.7. Geometry used to calculate the separation between a sightline, denoted by the blue star, and the center of a PGCC source, denoted by the rotated ellipses. The axes are in terms of relative Galactic coordinates, with the center of the source defined to be the origin. Parameters noted in white (σ_{maj}, σ_{min}, and θ) are taken from the PGCC catalog, while parameters shown in red (Δl and Δb) are calculated based on the sightline's location. These parameters are used in Equation 2.7 to determine the separation in terms of σ, which in this example is $\sim 2.4\sigma$.

This was done using the 2nd *Gaia* Data Release (DR2, Gaia Collaboration et al. 2018), which represents the largest and most accurate survey of stellar parallaxes to date. Since many of the stellar sightlines previously observed by STIS are bright, early-type stars, they are easily detectable by *Gaia*. Many have already been cross-referenced with this survey and assigned a *Gaia* DR2 identifier within the Simbad database. Sightlines that have not

yet been assigned such an identifier (10/84) are usually binary systems which have been assigned a single identifier within the HD catalog, but are resolved into their individual components within the *Gaia* dataset, and thus are treated as separate objects within their database. In these situations, a very small cone search (1 arcsec) was performed around the central location of the binary, and one of the returned entries was selected, assuming that the individual entries of the binary will have the same observed parallax.

Once the appropriate parallaxes have been selected, stellar distances (and their errors) are calculated using

$$d = \frac{1}{\overline{\omega}} \tag{2.8}$$

$$d_{max} = \frac{1}{\overline{\omega} - \sigma_{\overline{\omega}}} \tag{2.9}$$

$$d_{min} = \frac{1}{\overline{\omega} + \sigma_{\overline{\omega}}} \tag{2.10}$$

These results can then be compared to PGCC source distances and errors listed in the catalog. PGCC sources have analogous d_{max} and d_{min} measurements based on the distance uncertainty listed in the catalog. Cases where the stellar d_{min} from *Gaia* is greater than the source d_{max} from the catalog are flagged. These sightlines and the associated stellar and PGCC source distances are shown in Figure 2.8.

2.4.2. Indirectly Comparing Distances Using CO Emission

For all other cases, indirect methods must be used to determine if the source is in front of the star. This can be achieved using the Columbia-CfA CO Survey presented in Dame

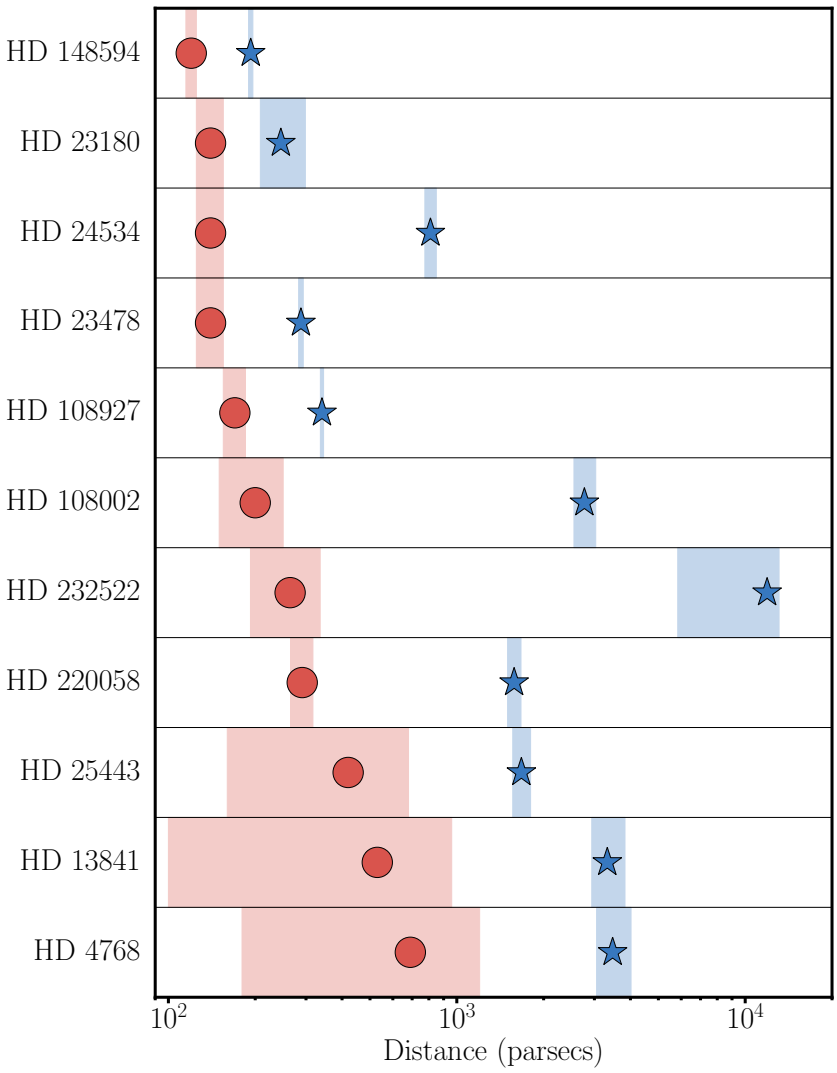

Figure 2.8. Sightlines where the star was deemed to be behind the gas of interest using *Gaia* DR2 stellar parallaxes. Each horizontal band compares the relative distances of a PGCC source (red) and its nearby star (blue). The associated colored bands represent the uncertainty ranges for each respective distance.

et al. (2001). This survey represents the broadest CO spectral survey in terms of sky coverage (Heyer & Dame 2015). Since direct distance values are no longer being compared, this indirect search can now include PGCC sources with no distance estimates.

By isolating CO emission data around the location of the PGCC source and star, it is possible to compare the CO emission at radio wavelengths to the observed CO absorption at UV wavelengths. If these emission and absorption components appear at the same velocity, it can be reasonably assumed that the absorption sightline is probing the same gas observed in emission. An example of such a comparison is seen in Figure 2.9, which compiles all of the relevant information for a single sightline, in this case HD 43582. This figure displays stellar distance (vis-a-vis the parallax from the *Gaia* catalog), the locations of the PGCC sources and the stellar sightline plotted on top of the CO emission from Dame et al. (2001), and absorption spectra from STIS for two species: O I which traces the total hydrogen column density (Meyer et al. 1998), and CO, which traces the molecular content. Furthermore, two CO emission spectra are included: one from the pixel on which the stellar sightline falls, and one from the pixel at the very center of the PGCC source. The good agreement in central velocity between absorption and emission, as well as the location of the sightline in the vicinity of a PGCC source, is a strong indication that this sightline is indeed probing PGCC gas.

2.5. Obtaining New Observations

While processing the data present in the *HST* archive, it was discovered that while numerous sightlines met our $< 10\sigma$ cutoff constraint, there were no cases where a sightline fell within the central 1σ region of a PGCC source. As this is nominally the true "source" as defined within the PGCC catalog, this represents an important part of the possible parameter space accessible with UV absorption sightlines that was at the time unexplored by the existing *HST* data. To remedy this, a new *HST* observing program was proposed

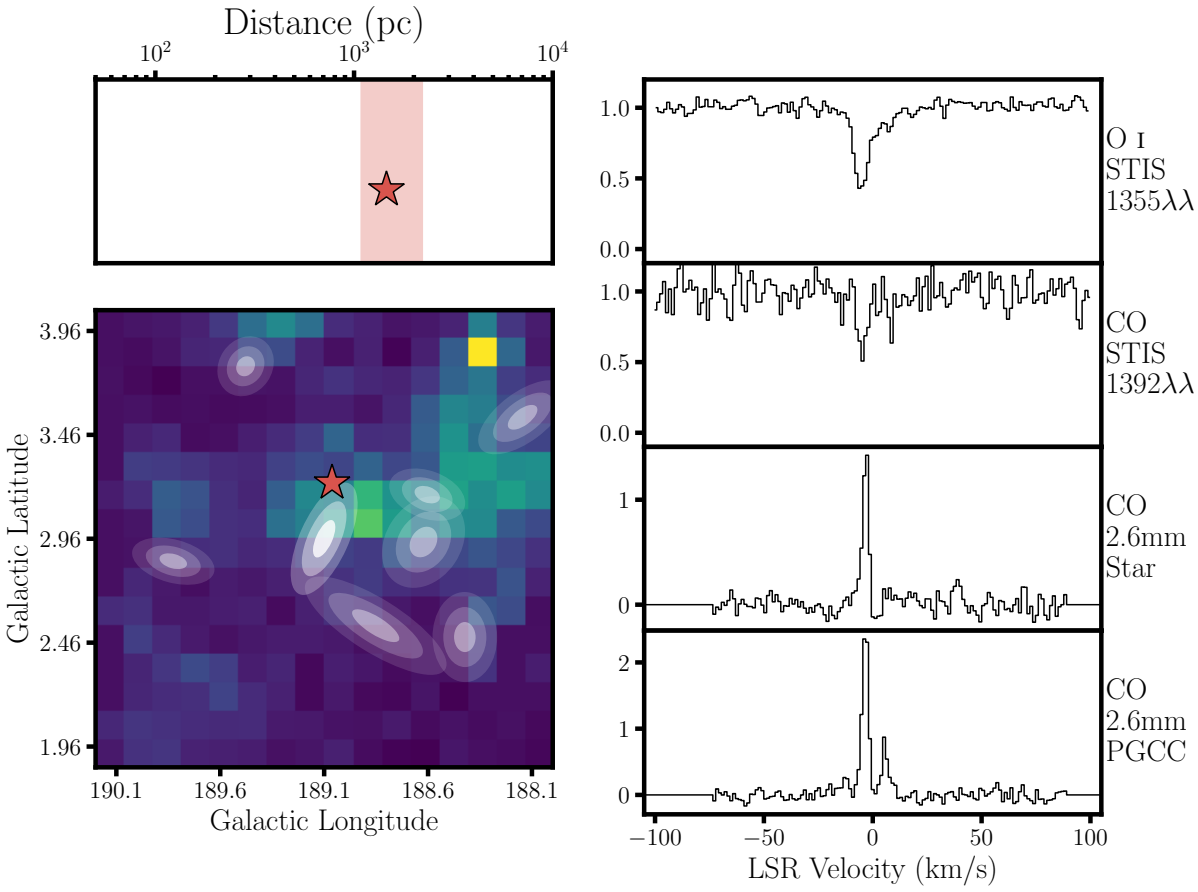

Figure 2.9. Combination of relevant data from *Gaia*, STIS, the PGCC catalog, and CO emission from Dame et al. (2001) for the sightline HD 43582. *Left:* All positional information for both the star and the PGCC source. The top panel displays the distance data, in this case only for the star, since this PGCC source has no distance estimate. The lower panel displays the sky location for the stellar sightline, and for the PGCC sources in this area of the sky. The background color map is the CO emission, integrated over a 10 km s^{-1} range centered on the peak of the CO emission. *Right:* Spectral data in both absorption and emission. The top two spectra represent *HST* STIS spectra centered on two specific species: the O I line at 1355.5977 Å that traces the total hydrogen column density Meyer et al. (1998), and the CO absorption band near 1392 Å. The bottom two spectra represent CO J=1-0 emission at 2.6mm extracted from two pixels on the map shown on the left: the pixel on which the stellar sightline lies, and the pixel on which the center of the PGCC sources lies. As is clear from the four spectra, the observed absorption occurs at the same relative velocity as the observed emission, indicating that this absorption sightline is probing the same gas giving rise to the emission seen at the center of the PGCC source.

to target 7 previously unobserved UV-bright sources determined to lie within the 1σ region of one of the PGCC sources, and whose *Gaia* distances placed them firmly behind the source. This proposal was accepted and implemented as General Observer program GO15104 in *HST* Cycle 25, with observations began in the summer of 2018. The first two sightlines observed as part of this program (HD 4768 and HD 220058) are included in this work, while the 5 other targets for this program (HD 236101, HD 217943, HD 334041, HD 147196, and HD 94414) were excluded in order to finish this work in a timely manner.

From the combination of the above methods, 25 total sightlines were identified and included in the dataset for this study: 11 via direct determination of the relative distances, and 14 via comparison of emission and absorption spectra. These sightlines, their associated PGCC sources, and the relative separation between the two are listed in Table 2.2. Furthermore, the distribution of relative separations in terms of the σ_{maj}, σ_{min} parameters defined in §2.3 is shown in Figure 2.10.

Table 2.2. Sightline Parameters

Star	PGCC	Separation[a] (σ)
HD 4768	G122.79-3.24	0.8
HD 13841	G134.21-4.20	3.6
HD 23180	G160.46-17.99	6.4
HD 23478	G160.52-17.04	6.1
HD 24398	G162.90-16.59	9.1
HD 24534	G162.84-17.15	3.1
HD 25443	G143.67+6.92	6.4
HD 43582	G189.10+2.96	3.3
HD 62542	G255.83-9.21	1.3
HD 72350	G262.63-3.24	1.6
HD 108002	G300.00-2.77	8.5
HD 108927	G302.11-14.92	8.2
HD 112999	G304.27+1.69	7.7
HD 124314	G312.84-0.71	4.3
HD 147683	G345.01+10.04	2.1
HD 148594	G350.77+14.50	7.6
HD 165918	G10.69-0.13	5.0
HD 185418	G54.02-2.38	7.3
HD 203532	G309.83-31.87	4.7
HD 208440	G104.08+6.36	1.2
HD 208947	G106.53+9.30	6.5
HD 210839	G103.46+2.81	9.1
HD 220058	G110.26-4.87	1.0
HD 232522	G130.69-6.79	1.4
HD 254755	G189.10+2.96	5.4

Sightlines identified for study in this work and the associated PGCC source which each sightline is deemed to be associated with, as well as the separation between the two.

[a] Values of separation are in units of σ, as defined in §2.3.

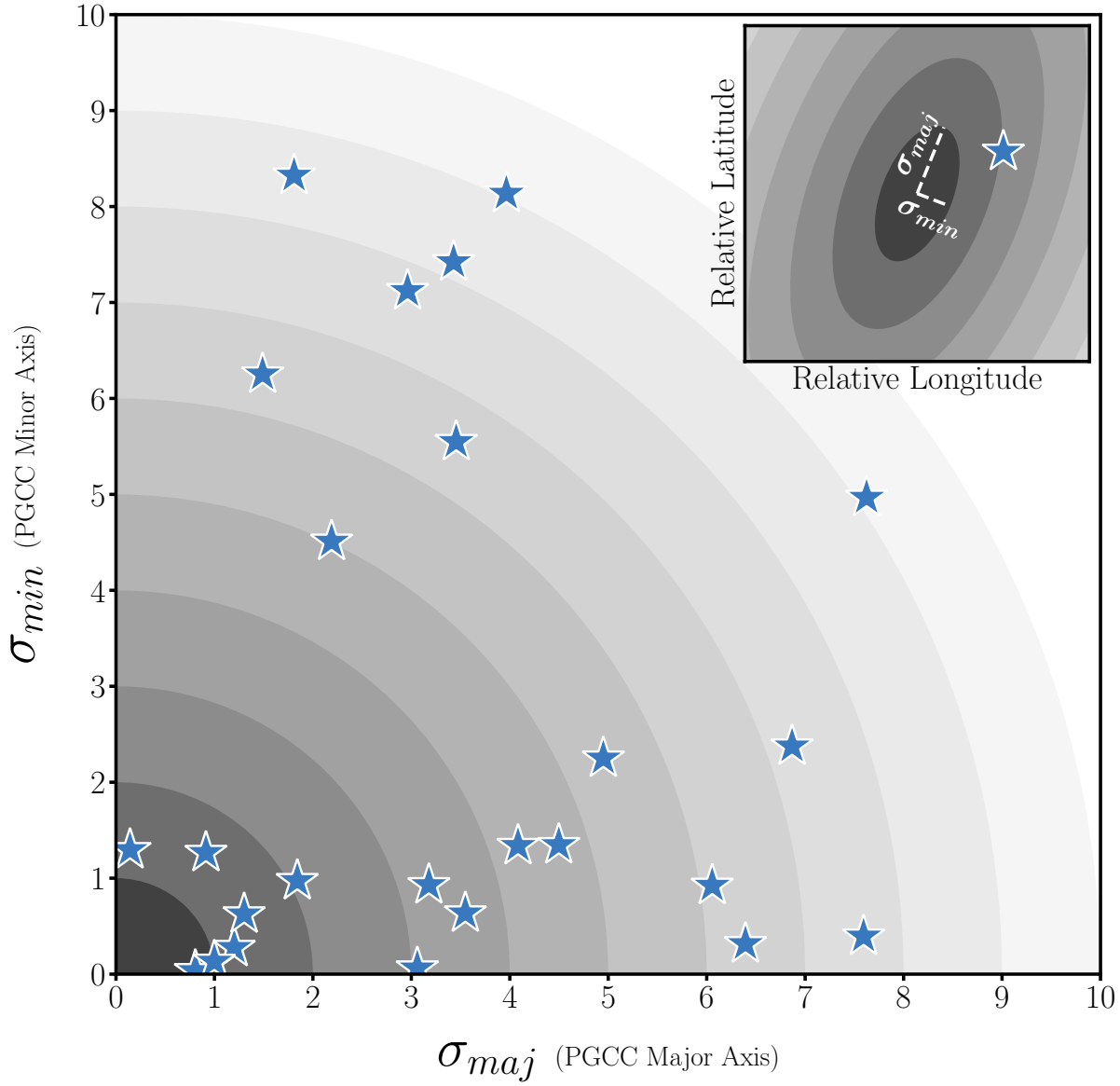

Figure 2.10. Distribution of separations between PGCC sources and their associated sightlines. The horizontal and vertical axes represent σ_{maj} and σ_{min}m the major and minor axes of the 2D Gaussian fits to each respective PGCC source, as listed in the PGCC catalog. Shaded contours thus represent the σ parameter as defined by Equation 2.7. The inset shows a visualization of how these parameters relate to the physical latitude/longitudes.

CHAPTER 3

Methods

As the ultimate goal of this project is to analyze the behavior of the abundances of specific species in the ISM, this abundance (i.e. column density) information must be distilled from the spectra obtained by *HST*. This chapter details the process by which the various calibrated, extracted X1D spectral datasets from the MAST archive are used to obtain abundance information. This process is twofold, involving the calibration and standardization of the spectral data, as well as the line-fitting process by which scalar abundance values are determined from the spectral data.

3.1. Data Calibration

All data calibration was performed using code written by the author in the `Python` programming language, and relies heavily upon the `numpy`, `scipy`, and `astropy` modules. This code was designed to emulate data calibration and reduction routines in the existing Image Reduction and Analysis Facility (IRAF)[1] distributed by National Optical Astronomy Observatories (NOAO). Code used for this data calibration is available at the author's GitHub page[2].

[1] `http://iraf.noao.edu`
[2] `https://github.com/codydirks`

3.1.1. Co-adding spectra

In the instances where multiple observations existed for a particular sightline, all spectra were co-added in the vicinity of the spectral lines of interest in order to increase the signal-to-noise ratio (S/N) and improve the overall data quality. This is a non-trivial process, as minuscule changes in the spectrograph optical components resulted in slight shifts in the assigned wavelengths, and therefore the wavelength grid is not necessarily identical between observations taken at different times. To correctly account for this, all of the individual spectral flux values must be mapped onto a common wavelength axis. This was done by selecting one of the axes present in the dataset and interpolating all of the other wavelength grids onto this selected grid using the `scipy` linear interpolation function `interp1d`. This function takes as input the original wavelength and flux arrays, as well as the new wavelength array on which to interpolate, and then returns the new fluxes at the locations defined by this new wavelength array.

Once all of the individual spectra have been transposed onto an identical wavelength grid, they can then be summed to create a single spectrum. In order to favor the contributions from higher signal-to-noise spectra, the contributions from each individual spectrum are weighted by that observation's exposure time. This weighted summation is performed pixel-by-pixel along the wavelength axis. Thus, when co-adding N individual spectra, each pixel's final flux value is calculated as:

$$F_i = \sum_{n=1}^{N} w_n \times F_i^n \tag{3.1}$$

$$w_n = \frac{t_{exp}^n}{\sum_{n=1}^{N} t_{exp}^n} \tag{3.2}$$

where F_i represents the flux of the i-th pixel along the wavelength axis, and w_n represents the weighting factor for the n-th spectrum. As is clear from Equation 3.2, these individual weights sum to unity by construction. The resulting summed, 1D spectrum is then passed to the continuum-fitting routine. An example of this summation is shown in Figure 3.1.

3.1.2. Continuum Fitting

When using absorption spectra to analyze abundances, the information content lies in the depth of the absorption line relative to the continuum flux. That is to say, the absolute scale of the fluxes is often irrelevant, as is the shape of the continuum flux profile. With this in mind, the spectra used in this work will be normalized such that the fluxes are no longer measured on an absolute scale, but rather a relative one (thus leaving only the deviations from continuum). Additionally, this normalization will remove any local variations in the continuum flux level.

To do this, the continuum is first isolated by masking any absorption components which clearly deviate from the stellar continuum. The remaining spectral data, which should be due solely to a noisy continuum profile, is modeled with a high-order Chebyshev polynomial. In each instance, the degree of this polynomial was determined manually,

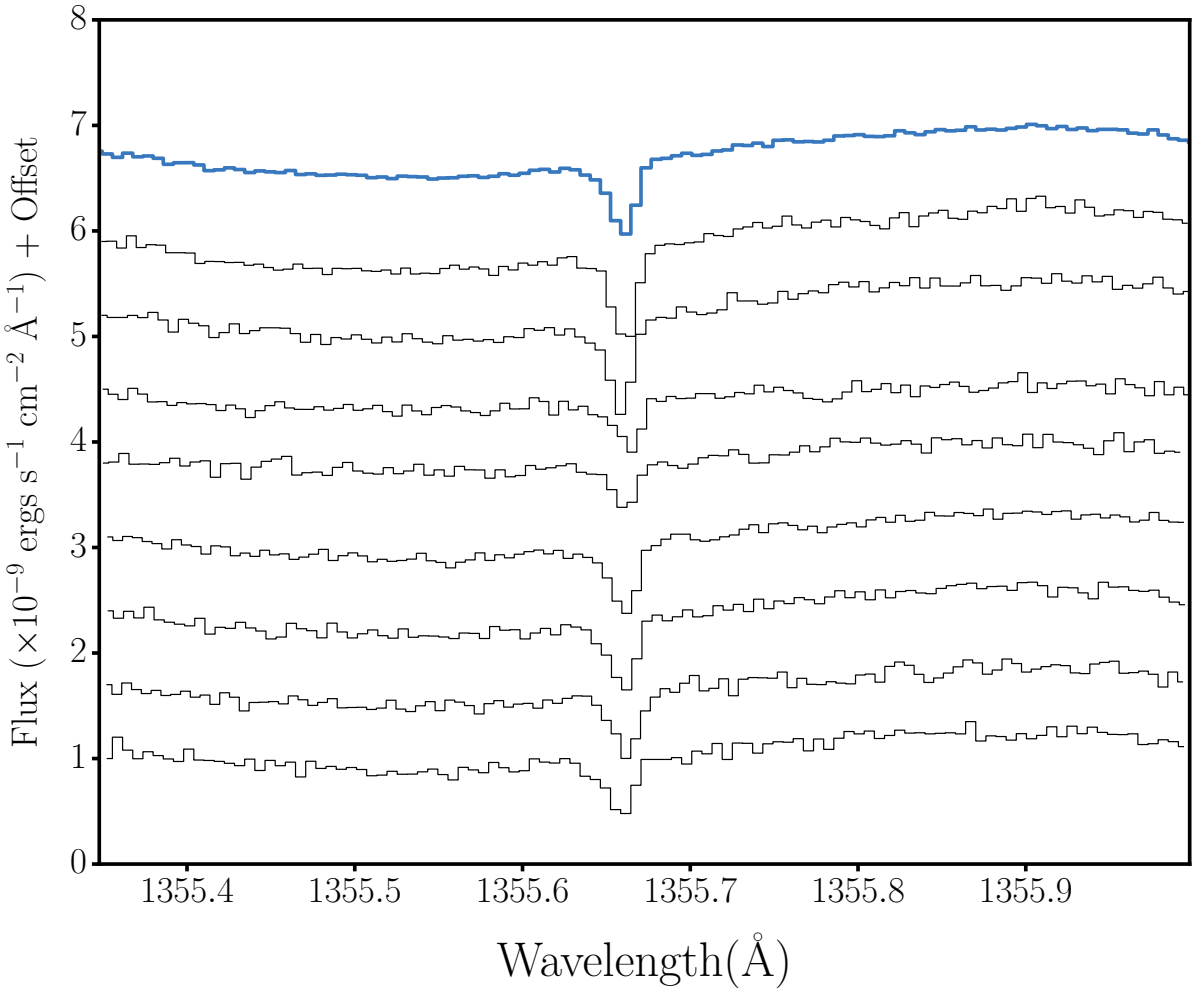

Figure 3.1. Visualization of the co-addition of individual spectral orders to create a single summed spectrum around the O I 1355.5977$\lambda\lambda$ line toward the sightline HD 24398. Shown in black are the individual spectral orders in the vicinity of the line. Shown in blue is the weighted summation of these individual orders.

as some sections of the continuum are relatively flat, while others could contain a considerable amount of variation. This necessitates care when choosing a polynomial order, as using a high-order polynomial on a relatively flat region of the continuum could result in overfitting the spectral noise, yielding a model that poorly describes the true continuum.

Once a sufficient polynomial solution is obtained, the entire spectrum is normalized by this continuum. This is done by evaluating the model continuum at each wavelength pixel, and dividing the true continuum at this pixel by the model value. Thus, the resulting normalized spectrum array contains data values between 0 and $\sim$1 (modulo the noise within the spectrum). An example of this continuum fitting process is seen in Figure 3.2. This process was done using a graphical interface developed by the author, designed to emulate existing continuum fitting routines present in the IRAF software package. The resulting normalized spectrum was output to a data file consisting of the wavelength, normalized flux, and normalized flux error of each data point.

3.2. Data Reduction

3.2.1. Determining physical parameters from absorption profiles

The normalized absorption spectra described above can be described generally as intensity as a function of wavelength. Any observed absorption (that is, a reduction in observed intensity relative to the expected background) is due to some material with optical depth τ_λ. Thus, the absorption spectrum can functionally be described as

$$I(\lambda) = I_0 e^{-\tau_\lambda}. \tag{3.3}$$

This optical depth encodes the physical information with which this work are concerned. Determining the relevant physical parameters from absorption profiles is primarily done in one of two ways - the apparent optical depth method, or cloud-component model fitting. The apparent optical depth method (Savage & Sembach 1991) directly transforms a typical absorption profile $I(\lambda)$ into an optical depth profile $\tau(\lambda)$ using Equation 3.3, which

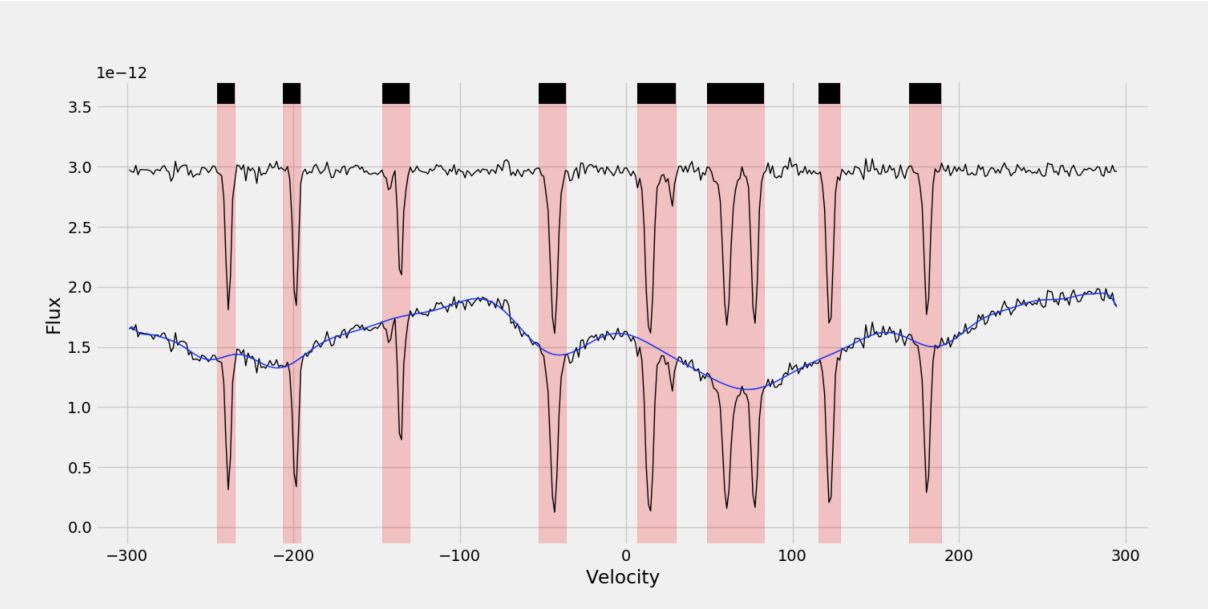

Figure 3.2. An example of the continuum fitting process. The raw spectrum, shown at bottom, is masked such that obvious absorption lines are identified and removed from the continuum data to be fitted. The masked regions are shown in red. The remaining spectral data are then fit with a high-order Chebyshev polynomial that accurately characterizes the remaining continuum. The ratio between the spectrum and this polynomial is then calculated for each point, with the resulting normalized spectrum plotted at the top of the image, yielding a resulting normalized spectrum where the data values lie between 0 and ∼1.

can then be integrated to determine the total sightline column density N. This method attempts to remain agnostic to the velocity structure along the sightline, and is typically useful when a profile is known to contain unresolved velocity structure. As this work is attempting to isolate the absorption due to the gas associated with a specific PGCC source, the second method, cloud-component model fitting, is preferred. This method treats the gas contributing to the absorption profile as individual discrete "clouds" along the sightline, requiring one to build a model defined by a combination of multiple absorption components. Each of these components is treated as a Voigt absorption profile defined by

three physical parameters: the column density N, which encodes the quantity of material contributing to the absorption; the linewidth b, which describes the observed width of the profile (the factors which contribute to this width will be discussed shortly); and a central velocity v, which describes the bulk motion of the entire parcel gas, independent of any internal velocity distribution.

Voigt profiles represent the convolution of two individual profiles: a Lorentzian and a Gaussian profile. The Lorentzian profile arises from the decay lifetimes of the energy states associated with these electronic transitions. Because these decay times are finite, Heisenberg's Uncertainty Principle dictates that this will create some finite width (ΔE) in the energy of the photons emitted during the electronic transitions, and thus a corresponding finite width in the photons' associated wavelength. The result of this is a Lorentzian profile $L(x;\gamma)$ with some natural linewidth γ, defined as:

$$L(x;\gamma) = \frac{\gamma}{\pi(x^2+\gamma^2)} \tag{3.4}$$

Additionally, depending on the temperature of the gas, there will be some inherent thermal velocity distribution which also contributes some width the the observed spectral line. The resulting profile is a Gaussian of the form

$$G(x;b) = \frac{1}{\sqrt{\pi}b}\, e^{-\frac{x^2}{b^2}} \tag{3.5}$$

where b represents the thermal linewidth, defined as

$$b^2 = \frac{2k_B T}{m} + 2\sigma_{turb}^2 \tag{3.6}$$

where k_B is Boltzmann's constant, T is the thermal temperature of the gas, and m is the mean molecular weight of the species. b is related to the traditional Gaussian width parameter σ by $b = \sqrt{2}\sigma$. Turbulent gas velocities σ^2_{turb} can also contribute to this linewidth, if the gas is sufficiently turbulent.

From these two individual profiles, the Voigt profile as a function of wavelength can be defined as a convolution of these two components:

$$V(\lambda; b, \gamma) = \int_{-\infty}^{\infty} G(\lambda'; b)\ L(\lambda - \lambda'; \gamma) d\lambda' \tag{3.7}$$

In practice, the natural linewidth γ is much, much smaller than b. Thus, these absorption profiles can, to an excellent approximation, be described as a pure Gaussian profile with linewidth b.

This profile is often also transformed into a function of velocity, rather than wavelength. This is done by applying a Doppler shift of the form

$$\frac{\lambda - \lambda_0}{\lambda_0} = \frac{v}{c} \tag{3.8}$$

These velocities are all defined relative to some reference wavelength λ_0 at which $v = 0$. This reference wavelength is commonly chosen to be the rest (i.e. laboratory) wavelength of the spectral line of interest.

The primary assumption inherent to this cloud-component fitting method is that each parcel of interstellar gas along the sightline contributes a discrete absorption component. These various components are then superposed to create the total absorption profile. This theoretical profile can then be compared to an existing spectrum and modified to

determine the best fit solution. This cloud-component method is often more complex than the apparent optical depth method, as it typically requires some a priori knowledge of the number of components, as well as initial estimates of each component's central velocity and linewidth. This knowledge is typically gleaned through analysis of other species along the same sightline, and thus often requires the analysis of multiple species before converging on an acceptable model of cloud components. This final model allows for the isolation and analysis of individual the "clouds" of gas along the sightline, rather than the convolution of multiple, un-associated regions of the ISM.

3.2.2. FITS6P

The `Fortran` program FITS6P Welty et al. (1994) was used to iteratively perform this cloud-component model fitting. This program allows for the user to interactively define absorption components with specific *(N,b,v)* parameters, as well as place constraints on how these parameters may vary. For instance, the user may choose to fix the linewidth b parameter to a specific value based on prior knowledge, or to constrain the central velocities such that all lines arising from the same absorption multiplet shift have identical central velocities. This approach is especially useful in instances when a sightline had many overlapping, saturated absorption components, from which the component structure and linewidths are not immediately apparent. Typically, this problem can be addressed by first identifying isolated, weak absorption lines of O I and C I to determine the component velocity structure and obtain best estimates for linewidths for the strongest components. These parameters were then applied to the more complex absorption profiles of CO or C I

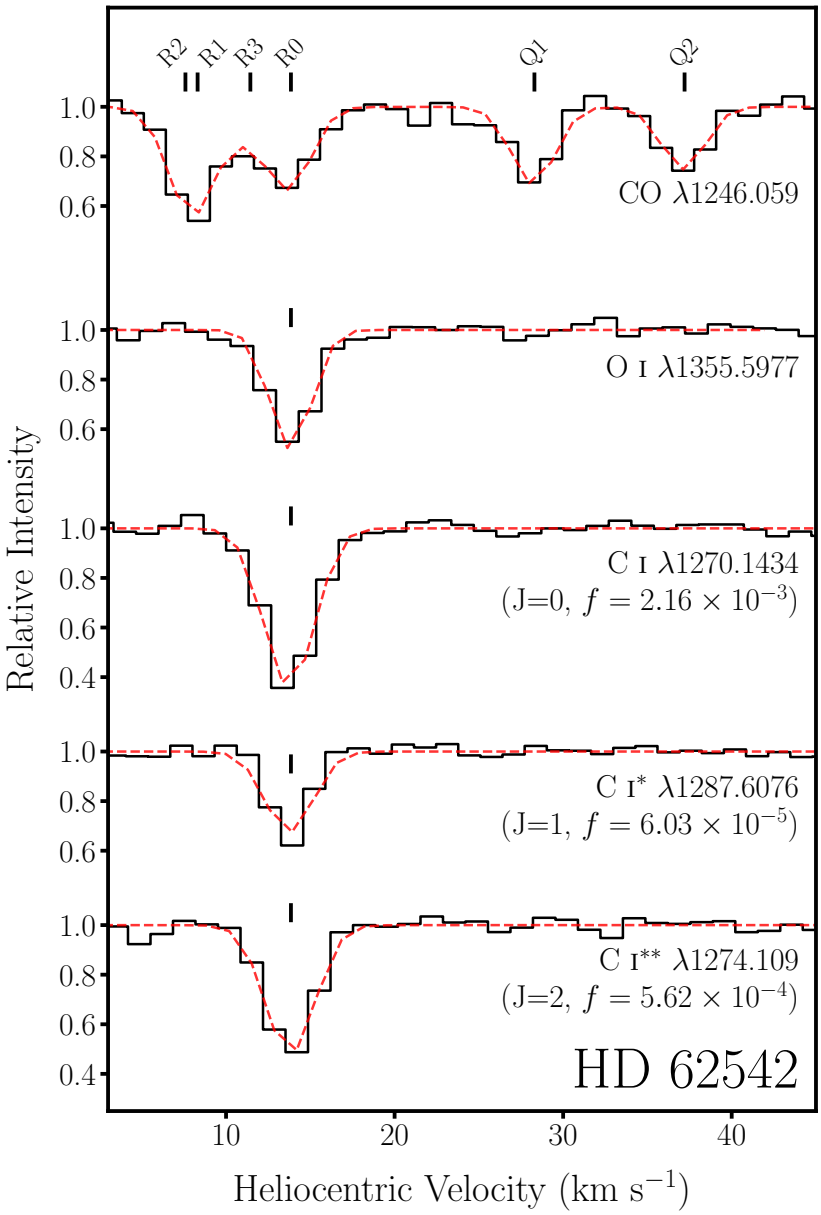

Figure 3.3. Example of cloud-component model fitting for the case of a sightline with a single absorption component. Shown are selected regions of the spectrum around absorption lines of interest (black histograms). Our FITS6P cloud-component models are overlaid as red dashed lines. Black tick marks denote the central velocity of each modeled line. For the CO absorption band (top), the individual lines that comprise the band are noted as well.

fine-structure multiplets, so that the column densities of those species could be accurately determined.

3.3. Species Used in this Analysis

3.3.1. Carbon Monoxide (CO)

As discussed in §1.3, CO represents the second-most abundant molecule behind H_2, and its two primary isotopes ^{12}CO and ^{13}CO have long served as useful probes of the molecular ISM. In addition to allowing for the determination of H_2 abundances, comparison of the column densities and central velocities of the two CO isotopes can yield insight into the kinematics of the molecular gas within these sources, indicating if the gas associated with PGCC sources is inherently turbulent or quiescent. These CO observations are taken in lieu of direct observation of H_2, which is inherently difficult due to the lack of a permanent dipole moment that would naturally give rise to observable rotational and vibrational electronic transitions.

CO exhibits over a dozen absorption bands in the far-UV regime accessible to the STIS bandpass. Thus, CO abundances can be reliably measured along our sightlines by simultaneously fitting these multiple bands, which allows for a more accurate determination of the central velocities and linewidths of each absorption component. Additionally, these absorption bands exhibit a wide range of oscillator strengths, which allows for the detection of any saturation effects by comparing the derived column densities for bands with differing oscillator strengths. Furthermore, utilizing absorption line measurements of these sightlines allows for a much more sensitive probe of the CO content than radio

emission studies, which are typically sensitive to column densities of N(CO) $\geq 10^{15}$ cm^{-2} (Liszt 2007) while absorption line studies can reliably probe down to N(CO) $\sim 10^{13}$ cm^{-2}.

3.3.2. C I

Carbon is one of the most abundant elements in the ISM. The carbon content of the ISM depends heavily on its physical conditions - in warm/hot diffuse ISM regions, singly ionized carbon (C II) is the dominant ion, while in cold, dense, molecular material, carbon is incorporated into the CO molecule. Neutral carbon (C I) can be formed from both the recombination of C II and the photodissociation of CO, and thus should probe the intermediate regions between molecular and atomic regions where these other species dominate (Burgh et al. 2010). Additionally, the ground state of C I contains fine-structure energy levels that are populated when C I collides with ambient atomic and molecular hydrogen (Jenkins & Shaya 1979). Thus, C I absorption is typically present as multiplet bands consisting of finely-spaced absorption lines from the ground-state C I and its two fine-structure excited states, C I* and C I**. The ultraviolet regime contains several of these C I multiplets with extremely disparate oscillator strengths, allowing for an accurate, robust measurement of each of these individual levels, which can be used to probe the gas thermal pressure (see §1.4.4), or summed to determine the total C I column density.

3.3.3. Dust content: O I, Kr I, Ge II, Mg II, Ni II

Dust is a ubiquitous feature within the ISM, and blackbody emission from dust represents the primary method by which the PGCC sources were initially detected. As discussed in section 1.1.1, the effect of this depletion is to reduce the gas-phase abundance which is

detectable via absorption-line spectroscopy. Studying the relative abundance of different species known to deplete at different rates can thus provide an estimate the dust content of the ISM probed by these sightlines. This methodology of comparing relative abundances to estimate dust depletions was first constructed by Jenkins (2009), who performed a study covering 17 different atomic species along 243 sightlines and quantified the relationships between the abundance of these atomic species and the dust content of the ISM. By drawing upon that study's quantitative results, a simpler study which requires only a few species to estimate the dust content of the ISM can be undertaken.

To achieve this, the following elements were studied: O I, Kr I, Ge II, Mg I, Ni II. These elements were chosen for two reasons. First, they span a broad range in how rapidly they deplete onto dust grains. Qualitatively speaking, Ni II and Mg II are typically heavily depleted onto grains, Ge II is moderately depleted onto grains, and O I and Kr I are lightly depleted onto grains. Second, all of these species have spectral lines that lie in the typical STIS E140H bandpass (though the choice of central wavelength for any given observation may affect whether a line is actually captured). Following the formulation laid out in Jenkins (2009, §3), an element's gas-phase depletion is defined as the reduction below the expected solar values, i.e.

$$\left[\frac{X_{\rm gas}}{H}\right] = \log\frac{N(X)}{N(H)} - \log\left(\frac{X}{H}\right)_{\odot} \tag{3.9}$$

where $\log(X/H)_{\odot}$ represents the expected solar abundance of a given element X.

Furthermore, one can construct a prediction for the depletion of element X as a function of some overall dust depletion strength parameter F_*, which denotes how far along in the depletion process this particular gas has progressed. This parameter was

defined in Jenkins (2009) to be dimensionless and on an arbitrary scale, varying between 0 for the sightline with the lowest observed overall depletions and 1.0 toward the strongly depleted ζ Oph (HD 149757), which represents one of the most well-studied sightlines with respect to elemental depletions. Since much of the data used in that study were derived as profile-integrated values rather than individual absorption components, the F_* values used in that work were generally not representative of local depletion values, which could conceivably be larger than $F_* = 1.0$.

Quantitively, F_* is defined as:

$$[X_{\rm gas}/H]_{\rm fit} = B_X + A_X(F_* - z_X) \tag{3.10}$$

Three additional fit parameters are defined, specific to each individual element: z_X is a reference point, B_X is the depletion at that reference point, and A_X represents the strength of the correlation between the observed depletion and the F_* parameter. Jenkins (2009) performed such fits to all of their included elements and derived A_X, B_X, and z_X values for each of the 17 elements in their study which are adopted here for the selected species of interest, as well as updated parameters from the follow-up study of O, Ge, and Kr by Jenkins (2019), when appropriate. Using the abundances measured as part of this work (Table 4.2) in combination with these elemental parameters, the dust depletion strength F_* for each the absorption components associated with the PGCC source can be determined.

Since this work does not directly measure the total hydrogen abundance, it would be preferable to eliminate this quantity from such a formulation to reduce uncertainty and to yield a result that is based solely on the (directly measured) elemental abundances.

This can be done by combining Equation 3.10 for two separate elements:

$$\frac{[X_1/H]}{[X_2/H]} = \frac{B_1 + A_1(F_* - z_1)}{B_2 + A_2(F_* - z_2)}. \tag{3.11}$$

Combining Equations 3.9 and 3.11 yields a final equation which does not depend directly on the measured N(H), instead relying on the relative abundance of two other species of interest:

$$\log\frac{N(X_1)}{N(X_2)} + \log\left(\frac{X_2}{H}\right)_\odot - \log\left(\frac{X_1}{H}\right)_\odot = (B_1 - B_2) + (A_2 z_2 - A_1 z_1) + (A_1 - A_2)F_* \tag{3.12}$$

Equation 3.12 allows one to solve for the F_* parameter for a given absorption component using only two directly measured elemental abundances and the associated empirically-determined fit parameters for those two elements (Table 3.1).

Table 3.1. Elemental Depletion Parameters

Element	$\log(X/H)_\odot$[a]	A_X	B_X	z_X
Oxygen	8.76 ± 0.05	-0.009 ± 0.100	-0.130 ± 0.110	0.538
Magnesium	7.62 ± 0.02	-0.997 ± 0.039	-0.800 ± 0.022	0.531
Nickel	6.29 ± 0.03	-1.490 ± 0.062	-1.829 ± 0.035	0.599
Germanium	3.69 ± 0.05	-0.300 ± 0.060	-0.490 ± 0.006	0.531
Krypton	3.29 ± 0.08	-0.140 ± 0.210	-0.160 ± 0.025	0.531

Adapted from Table 4 of Jenkins (2009) and Table 6 of Jenkins (2019). Elemental depletion parameters for the species of interest, derived from simultaneous fits to aggregated elemental abundance data.

[a] Relative solar abundances from Lodders (2003) on a logarithmic scale with H=12.

3.4. Determining H_2 Column Densities

As described previously, the STIS bandpass between 1150 – 1700Å lacks any direct H_2 absorption features. Thus, in order to determine the H_2 column densities, it is necessary to either rely on previously published quantities or to use some other indirect determinant of $N(H_2)$. While many of the sightlines included in this study have previously published $N(H_2)$ values, the majority of these were taken with other UV missions, primarily *FUSE*. As the highest *FUSE* spectral resolution (R$\sim$20,000) is still far below what is capable with the highest-resolution STIS echelle gratings (R$\geq$110,000), it is impossible to perform the same component-fitting analysis on *FUSE* observations as has been detailed above using STIS data. Thus, indirect methods are necessary to estimate $N(H_2)$ in the absorption components of interest. As has been shown previously, the CO/H_2 ratio varies by several orders of magnitude in the regime we are interested in (Burgh et al. 2007; Sonnentrucker et al. 2007; Sheffer et al. 2008), so a conversion based on the directly measured N(CO) quantities could prove to be quite uncertain.

As an alternative indirect method, Burgh et al. (2010) found a good correlation between the observed CO/H_2 ratio and the CO/C I ratio for 34 sightlines toward Galactic O and B stars. Their analysis was done using sightline-integrated values rather than individual components, which allowed for them to utilize $N(H_2)$ quantities from *FUSE* which has previously been compiled by Burgh et al. (2007) and Sheffer et al. (2008). If these quantities are well-correlated, then measurements of N(CO) and N(C I), which can both be obtained directly using STIS, can be used to estimate $N(H_2)$. The Burgh et al. (2010) dataset was combined with a second dataset created by combining this work's

measurements of N(CO) and N(C I) (which can be integrated over all observed absorption components to determine an analogous sightline-integrated value) with previously published $N(H_2)$ values for 12 of these sightlines compiled by Gudennavar et al. (2012). Both of these datasets are plotted in Figure 3.4. As is clearly visible in this plot, there is a strong linear correlation between these the logarithm of these two quantities.

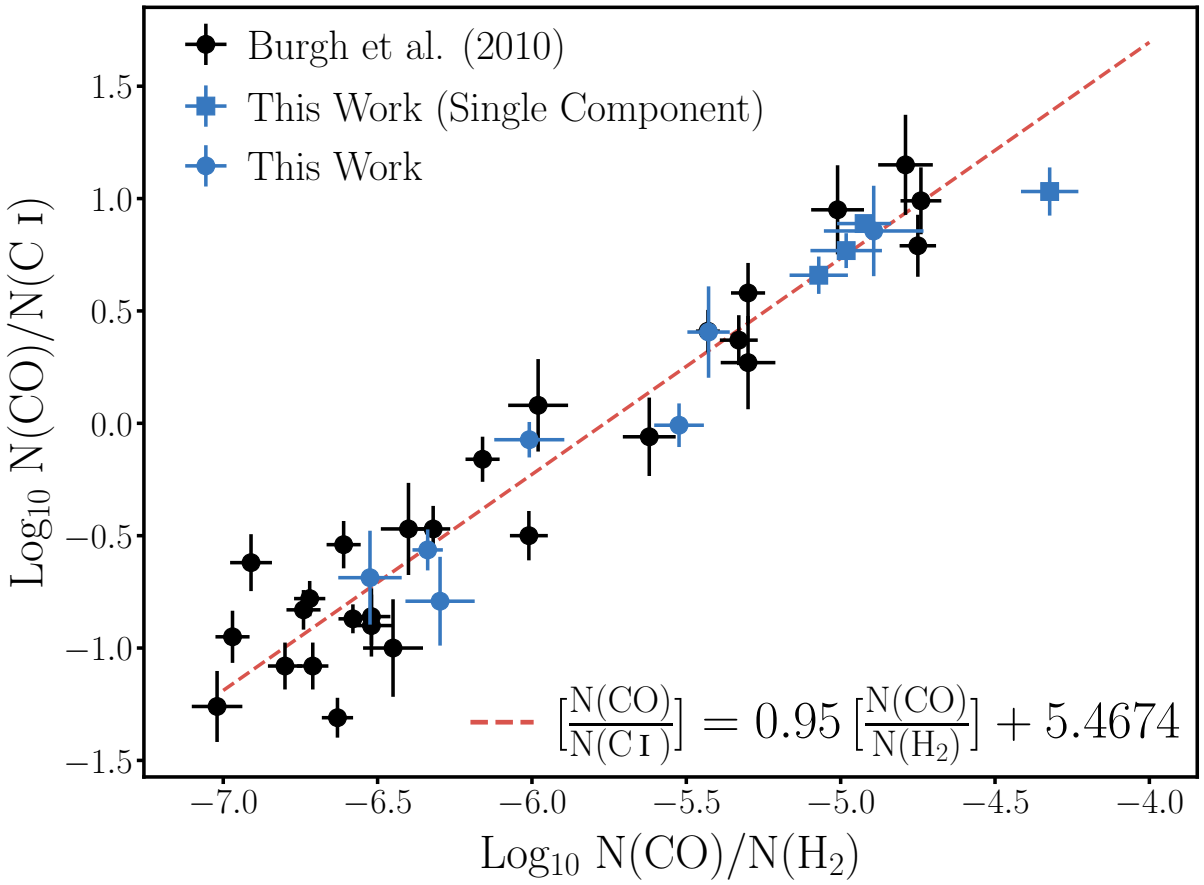

Figure 3.4. H_2 indirect method.

It should be noted that this relationship is derived using only sightline-integrated values, yet its intended use in this work is to estimate the H_2 abundances in individual absorption components. Ideally, in order to test the robustness of this relationship for both

sightline-integrated and individual-component values, a sample of sightlines with only a single observed absorption component would be tested and compared to the sightline-integrated relationship, to confirm that they yield a similar result. However, of the identified sample of 12 sightlines which have H_2 values present in Gudennavar et al. (2012), only four (HD 24398, HD24534, HD 62542, and HD203532) have absorption profiles defined by a single component, limiting the ability to perform a robust, quantitative analysis on the effects of integrating over the entire sightline with the current dataset. Sightlines with a single component are noted in Figure 3.4. Qualitatively speaking, these sightlines appear to obey the same relationship as those with multiple components. Nevertheless, it remains a critical assumption that both individual components and sightline-integrated values obey the same relationship.

To verify the accuracy of this method, we apply this relationship to the 12 sightlines for which we have $N(H_2)$ values from Gudennavar et al. (2012) and compare the derived values to the known published values. We find that in all cases, this method correctly predicts $N(H_2)$ to within 0.35 dex (i.e. a factor of $\sim$2).

3.5. Determining the Total Hydrogen Abundance

The total hydrogen column density N(H) represents a combination of the neutral atomic hydrogen N(H I) as well as the molecular hydrogen $N(H_2)$, such that $N(H) = N(H\ I) + 2N(H_2)$. While the method outlined in the previous section allows for a determination of $N(H_2)$, measuring N(H I) with STIS requires studying the Lyman-alpha

(Lyα) spectral line at 1215.67Å, which is typically observed to have a very broad, saturated profile. As such, disentangling discrete Lyα absorption components using FITS6P is often fruitless and subject to significant uncertainties.

As an alternative, the elemental dust depletion calculations described in §3.3.3 can be leveraged as an indirect measurement of N(H), as these dust depletions are all calculated relative to N(H) (Equation 3.9). Thus, having determined a value for F_*, one can work backward using Equations 3.9 and 3.10 to determine a value for N(H) given a specific element's abundance. This calculation can be done for each element, allowing for N(H) to be sampled several times. The resulting individual values can then be combined to determine an average N(H).

3.6. Isolating Components of Interest

Rather than integrating the absorption line results over the entire profile, and thus convolving the physical properties of multiple unrelated parcels of interstellar gas, this work seeks to identify and isolate the single absorption component arising from the gas associated with the PGCC source. This method yields a more accurate assessment of local physical environment, at the expense of introducing uncertainty related to discerning between overlapping components. The profile-fitting method described above yielded a cloud-component model for each sightline, often containing multiple absorption components. The total number of different components detected along each sightline is shown in Table 3.2. The component with the largest N(CO) value was selected as the component associated with the PGCC source. While many sightlines (12/25) have multiple components of CO absorption, the total CO column density is typically dominated by a

single component. Table 3.2 details for each sightline which component was selected to be associated with the PGCC source, as well as the percentage of the total sightline N(CO) that this selected component accounts for. Unless otherwise noted, all results detailed in §4 use column densities for this specific component rather than the entire profile.

Table 3.2. Selected Absorption Components

Star	# Comp.[a]	Velocity[b] (km s^{-1})	log $N(CO)_{comp}$ [c] (log cm^{-2})	% Total N(CO)[d]
HD 4768	9	-18.5	14.67	55
HD 13841	11	-13.7	14.36	100
HD 23180	2	14.7	14.64	82
HD 23478	2	11.0	14.87	82
HD 24398	1	14.4	15.69	100
HD 24534	1	15.2	16.02	100
HD 25443	3	4.2	14.31	36
HD 43582	3	7.3	13.93	77
HD 62542	1	13.8	16.49	100
HD 72350	4	20.2	14.05	100
HD 108002	8	9.9	13.63	89
HD 108927	1	10.2	15.30	100
HD 112999	4	8.1	12.85	100
HD 124314	5	2.8	14.01	75
HD 147683	2	-0.9	15.79	100
HD 148594	1	-4.7	12.75	100
HD 165918	2	-6.9	13.32	100
HD 185418	4	-11.1	14.60	80
HD 203532	1	15.0	15.57	100
HD 208440	5	-23.1	13.65	45
HD 208947	2	-14.4	14.10	100
HD 210839	7	-14.8	15.38	100
HD 217943	3	-11.4	13.55	87
HD 220058	2	-7.5	13.52	62
HD 232522	4	-17.0	13.45	56
HD 236101	3	-10.6	12.75	100
HD 254755	7	6.4	15.82	100
HD 334041	5	-12.5	13.60	67

[a] Total number of unique velocity components present across all studied species. Not all components are present in all species.
[b] Velocity of the single component deemed to be associated with the PGCC source.
[c] log N(CO) of the single isolated component.
[d] Percentage of the total CO column density (integrated across all observed CO components) attributable to this component.

CHAPTER 4

Results

4.1. Comparison with Radio Studies: CO-bright vs. CO-dark

As detailed in §1.3, there are inherent limits to the detectability of CO via radio emission. Column densities below N(CO)$\sim 10^{15}$ cm^{-2} are difficult to detect, though CO column densities in diffuse and translucent clouds are detected through UV absorption as small at 10^{13} cm^{-2}. With this in mind, two classes of sightlines are defined: "CO-bright" sightlines, i.e. those that have CO column densities of 10^{15} cm^{-2} or greater which would be detectable via CO radio emission, and "CO-dark" sightlines with N(CO)$<10^{15}$ cm^{-2}. Sightlines which fall into each category, as well as the relevant molecular column densities, are shown in Table 4.1. Within the sample analyzed in this work, 8/25 (32%) sightlines are considered "CO-bright." This is a comparable rate to the radio survey conducted by Liu et al. (2018), which surveyed ∼2,000 PGCC sources and detected CO toward ∼29% of their sample. These class distinctions will be referenced extensively in the following sections.

4.2. Spatial Dependence

As molecular regions of the ISM are commonly thought of as dense knots tapering off into more diffuse regions, it would be expected that the CO abundance should decrease as a function of distance away from the center of the associated PGCC source. In this vein, the observed CO column densities for components associated with PGCC sources

Table 4.1. Molecular Column Densities

Star	PGCC Source	Sep.[a]	log N(CO)	log $N(H_2)_{UV}$[b]	log $N(H_2)_{PGCC}$[c]
CO-bright					
HD24398	G162.90-16.59	9.1	15.69 ± 0.08	20.67 ± 0.11[1]	20.49 ± 0.12
HD24534	G162.84-17.15	3.1	16.02 ± 0.03	20.84 ± 0.17	20.46 ± 0.19
HD62542	G255.83-9.21	1.3	16.49 ± 0.08	20.81 ± 0.27[2]	20.47 ± 0.47
HD108927	G302.11-14.92	8.2	15.30 ± 0.21	20.53 ± 0.16	20.53 ± 0.20
HD147683	G345.01+10.04	2.1	15.79 ± 0.20	20.58 ± 0.15	20.32 ± 0.30
HD203532	G309.83-31.87	4.7	15.57 ± 0.08	20.64 ± 0.09[1]	20.11 ± 0.19
HD210839	G103.46+2.81	9.1	15.38 ± 0.04	20.55 ± 0.18	21.03 ± 0.43
HD254755	G189.10+2.96	5.4	15.82 ± 0.24	20.83 ± 0.14	21.31 ± 0.46
CO-dark					
HD4768	G122.79-3.24	0.8	14.67 ± 0.10	20.13 ± 0.19	20.08 ± 0.28
HD13841	G134.21-4.20	3.6	14.36 ± 0.12	19.95 ± 0.19	20.48 ± 0.14
HD23180	G160.46-17.99	6.4	14.64 ± 0.33	20.55 ± 0.15	21.97 ± 0.16
HD23478	G160.52-17.04	6.1	14.87 ± 0.07	20.57 ± 0.20	21.31 ± 0.35
HD25443	G143.67+6.92	6.4	14.31 ± 0.10	19.96 ± 0.19	20.34 ± 0.22
HD43582	G189.10+2.96	3.3	13.93 ± 0.10	20.45 ± 0.22	21.31 ± 0.46
HD72350	G262.63-3.24	1.6	14.05 ± 0.08	19.96 ± 0.20	21.02 ± 0.17
HD108002	G300.00-2.77	8.5	13.63 ± 0.08	19.72 ± 0.21	20.81 ± 0.25
HD112999	G304.27+1.69	7.7	12.85 ± 0.99	19.77 ± 0.13	21.17 ± 0.44
HD124314	G312.84-0.71	4.3	14.01 ± 0.09	20.13 ± 0.21	21.73 ± 0.22
HD148594	G350.77+14.50	7.6	12.75 ± 1.28	20.06 ± 0.60	20.93 ± 0.28
HD165918	G10.69-0.13	5.0	13.32 ± 0.08	20.08 ± 0.23	22.18 ± 0.37
HD185418	G54.02-2.38	7.3	14.60 ± 0.06	20.30 ± 0.20	21.09 ± 0.10
HD208440	G104.08+6.36	1.2	13.65 ± 0.23	20.06 ± 0.20	20.37 ± 0.45
HD208947	G106.53+9.30	6.5	14.10 ± 0.08	20.63 ± 0.23	20.35 ± 0.38
HD220058	G110.26-4.87	1.0	13.52 ± 0.12	20.31 ± 0.23	20.40 ± 0.17
HD232522	G130.69-6.79	1.4	13.45 ± 0.07	19.70 ± 0.22	20.56 ± 0.07

Note: All results listed here are for the single component deemed to be associated with the PGCC source (see Table 3.2).

[a] Separation between star and PGCC source (see Table 2.2).

[b] When noted, the values and their errors are taken from the following references: (1) Cartledge et al. (2001); (2) Jensen et al. (2005). In all other cases, $N(H_2)$ is derived using the empirical relationship described in §3.4.

[c] Molecular hydrogen column densities listed for the PGCC source, which is defined as the 1σ region (where σ is defined by Equation 2.7).

are plotted in Figure 4.1 as a function of the sightline's projected distance away from the center of the PGCC source. Using the CO-bright and CO-dark distinction described above, it is clear that the CO-bright sample exhibits a unique behavior in their measured N(CO) values – as a function of projected distance away from the center of the source, N(CO) steadily decreases. This is in stark contrast to the behavior of the CO-dark sample, which shows no trend whatsoever with distance, and shows a large spread of $\sim$2 dex in the observed N(CO) values. This result suggests that a transition in the ISM structure occurs around this N(CO) threshold. Below this threshold, the ISM appears patchy, while above this threshold, these sources develop into smoother, more coherent CO envelopes.

In a similar manner, the CO/C I ratio (and the corresponding CO/H_2 ratio, which is related to the CO/C I ratio via the relationship discussed in §3.4) appears to vary with projected distance for CO-bright sources (Figure 4.2). It is notable that all CO/C I values for the CO-bright sample are larger than all CO/C I values for the CO-dark sample. As discussed in Burgh et al. (2010), CO/C I = 1 and $CO/H_2 = 10^{-6}$ served as discriminators between "diffuse" and "translucent" sightlines. For the sample used in this work, a CO/C I ratio of $\sim$2 appears to distinguish between the CO-bright and CO-dark sample. While this threshold is slightly higher than the one suggested by Burgh et al. (2010), it is important to note that their study was carried out using profile-integrated column densities, whereas this work isolates the single component associated with the PGCC source. Since neutral carbon is, in general, more abundant in the ISM than CO, the effect of integration along the entire profile would be to drive the CO/C I to smaller values. Even taking this slight caveat into consideration, it is clear that the distinction between

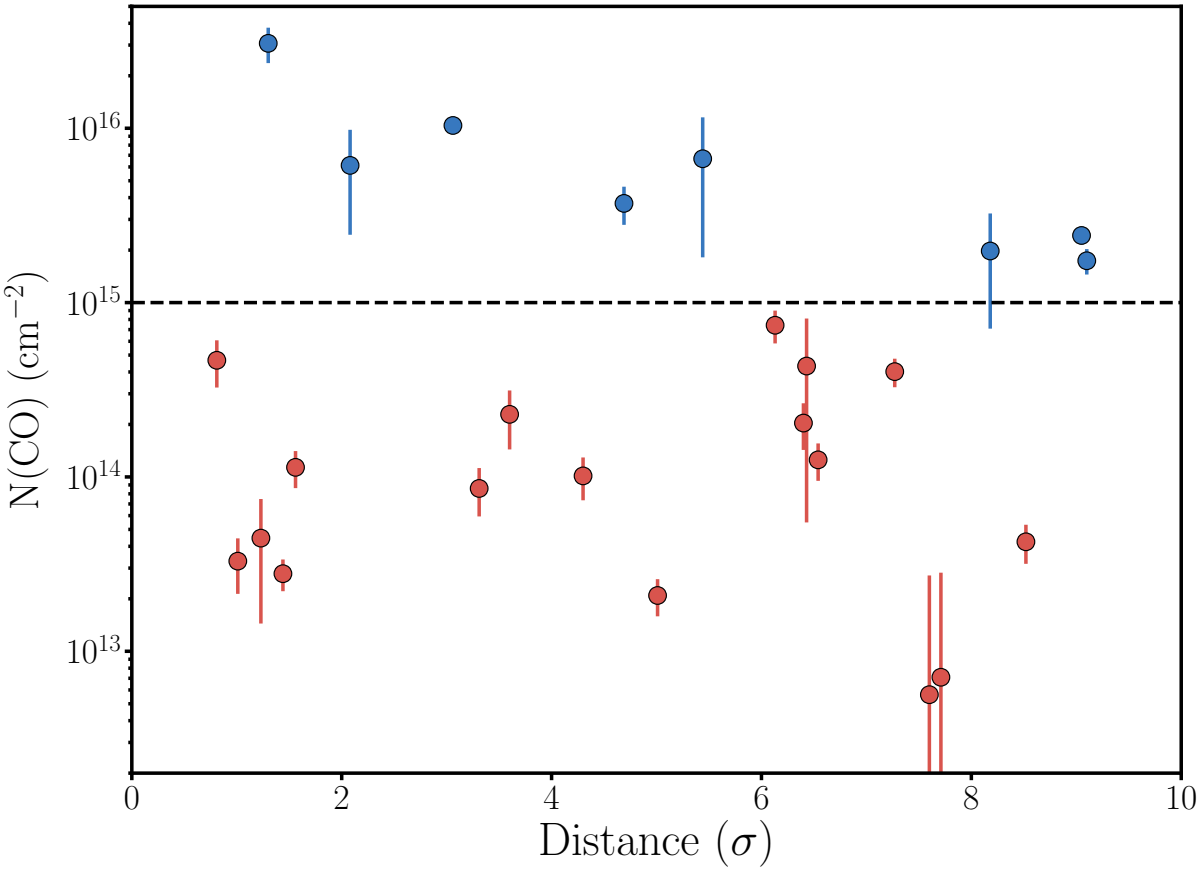

Figure 4.1. N(CO) as a function of projected distance from the center of the source. The units of the horizontal axis are σ, as defined by Equation 2.7. A threshold is drawn at N(CO) = 10^{15} cm^{-2}. Points above this threshold are coded blue, while points below this threshold are coded red.

"diffuse" and "translucent" detailed in Burgh et al. (2010) correspond quite neatly to the distinction of "CO-bright" or "CO-dark" detailed here.

4.3. ^{12}CO/^{13}CO Isotope Ratios

As mentioned previously, turbulence is one of the primary proposed mechanisms by which the ISM becomes dense enough to form molecular material. Szűcs et al. (2014) used hydrodynamic simulations to show that the effects of turbulence in pre-stellar molecular

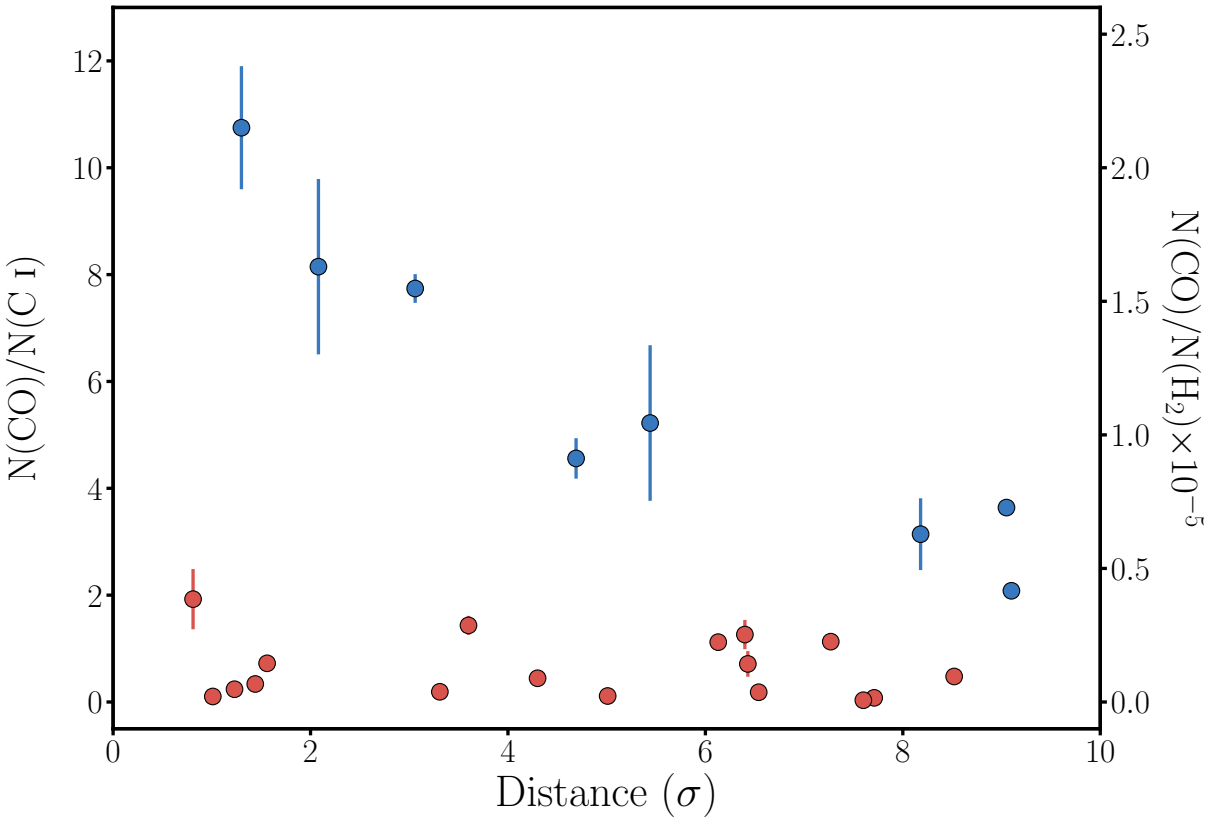

Figure 4.2. CO/C I as a function of projected distance from the center of the source. Color-coding is identical to Figure 4.1.

clouds can be seen in the behavior of the ^{12}CO/^{13}CO isotope ratio, with the ratio varying by a factor of a few as a function of increasing column density (Figure 4.3). In a similar manner, the observed central line velocities of these two isotopes can indicate the relative locations of the isotope-bearing gas within the clouds. Identical line velocities would indicate that the isotopes reside in the same location, while differing central velocities would be indicative of kinematics and/or chemical fractionation within the cloud, with ^{12}CO and ^{13}CO thus arising from different layers within the cloud.

An important result seen in these turbulent hydrodynamic simulations is a significant decrease in the ^{12}CO/^{13}CO ratio beginning at N(^{12}CO) $\sim 10^{13}$ cm^{-2} and reaching a

minimum around N(^{12}CO) $\sim 10^{16}$ cm^{-2} before increasing again. As seen in Figure 4.3, this feature is present regardless of the specific simulation parameters, indicating that this is a common feature of a turbulent molecular ISM.

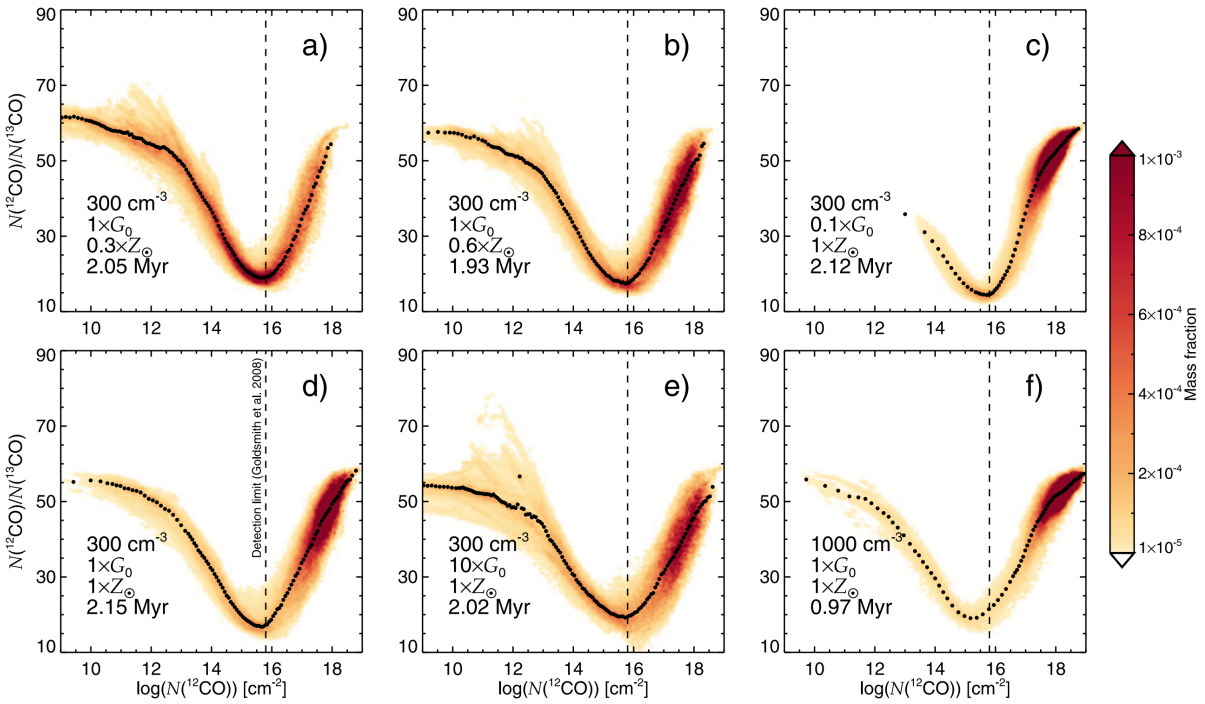

Figure 4.3. Smoothed-particle hydrodynamical simulation results from Szűcs et al. (2014). The simulated CO isotope ratio N(^{12}CO)/N(^{13}CO) is plotted as a function of the N(^{12}CO) for various combinations of simulation parameters, including the initial cloud volume density n_0 in cm^{-3}, the strength of the interstellar radiation in units of the standard interstellar radiation field strength G_0 defined in Draine (1978), the gas metallicity in units of the solar metallicity $Z_\odot$, and the simulation time (in Myr) at which the snapshot was taken. The colorbar indicates the relative gas mass fraction for each simulation particle, while the black points indicate the resulting isotope ratios when the data are binned along the x-axis.

^{13}CO is not ubiquitously seen within along the sample of sightlines studied in this work, with only 10/25 sightlines exhibiting detectable ^{13}CO absorption. Unsurprisingly, this subset is biased towards sightlines with the highest N(^{12}CO) values, containing all

8 of the CO-bright sightlines, as well as 2 additional CO-dark sightlines with N(^{12}CO) near the cutoff limit of 10^{15} cm^{-2}. Figure 4.4 shows the observed N(^{12}CO)/N(^{13}CO) as a function of N(^{12}CO), analogous to Figure 4.3. For all of the sightlines with detected ^{13}CO, the observed isotope ratio appears constant as a function of N(^{12}CO), with an average value of N(^{12}CO)/N(^{13}CO) $\sim$ 70. Additionally, the observed central line velocities of ^{12}CO and ^{13}CO derived from FITS6P profile fitting all fall within 1 km s^{-1} of each other, indicating a lack of internal cloud dynamics or chemical fractionation that would serve to differentiate these isotope velocities.

This combination of a nearly constant CO isotope ratio and matching central line velocities indicate that these PGCC sources are generally quiescent, rather than turbulent, dynamic sources. Wu et al. (2012) had previously reached a similar conclusion based on observations and analysis of ^{12}CO and ^{13}CO emission line profiles toward 674 sources in the *Planck* Early Cold Core Catalogue (ECC), which represented a precursor survey to the eventual full PGCC catalog. They found that 94% of the sources in their sample also displayed matching central line velocities, and concluded that ECC sources were inherently quiescent. It is important to restate here that the sample probed by Wu et al. (2012) and those in this work which display ^{13}CO absorption are biased toward the sources with the highest CO column density, and thus this conclusion of quiescent PGCC sources may not hold for the more diffuse sample which is incapable of being studied using ^{13}CO.

4.4. Comparing Molecular Hydrogen Column Densities

Many entries in the PGCC catalog contain estimates of the H_2 column density. As detailed in §2.1.3, these estimates are based on the dust emissivity maps, and thus are

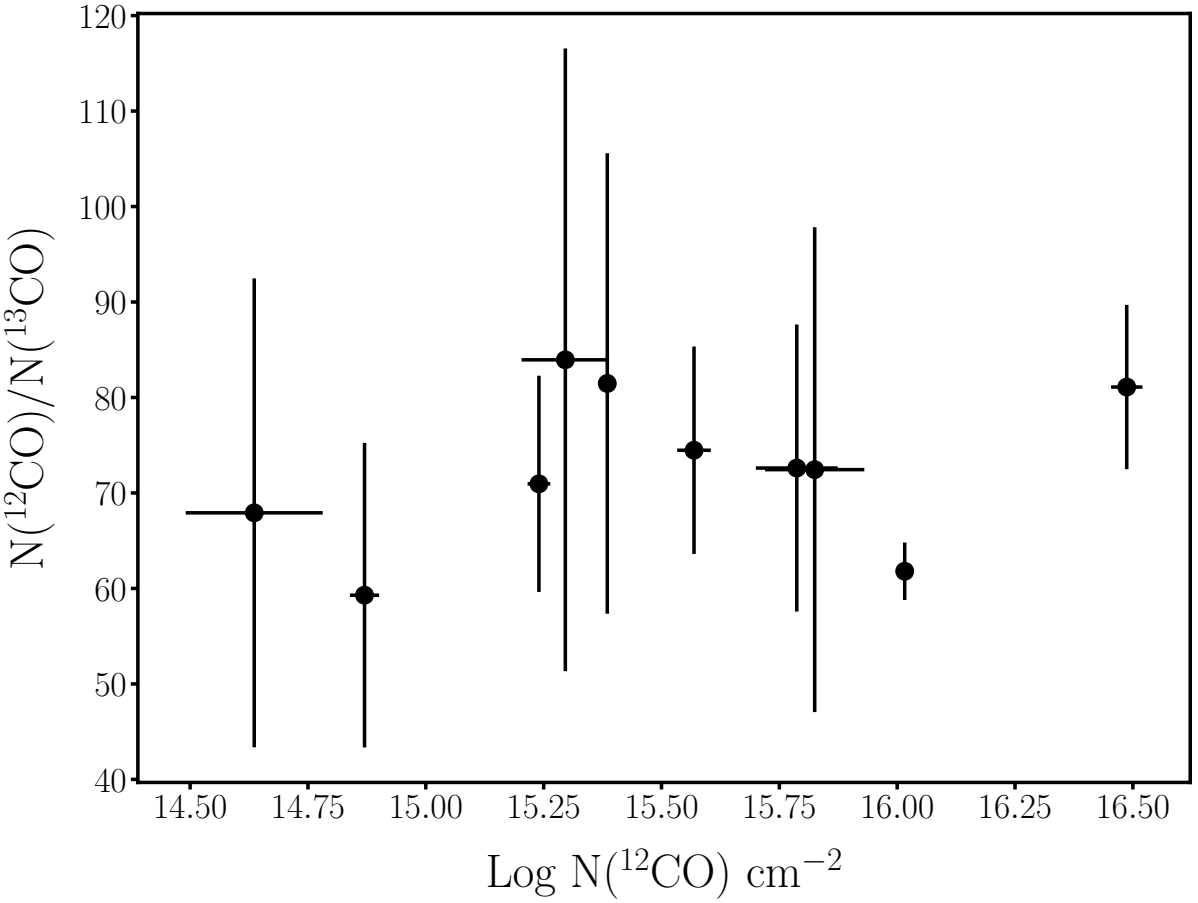

Figure 4.4. Observed CO isotope ratios (and associated errors) as a function of N(^{12}CO). When compared to the simulations seen in Figure 4.3, there is a clear lack of a large decrease and subsequent increase in the isotope ratio.

inherently limited by the angular resolution of these emissivity maps. In contrast to these emission measurements, an absorption line measurement of N(H_2) is only sensitive to the ISM along a single, narrow line-of-sight between the observer and the targeted background star. In terms of angular resolution, this absorption "beam" has a width that is typically of order $0.0001''$, many orders of magnitude smaller than the *Planck* beam. Because these two methods are sensitive to entirely different angular scales, any discrepancy between

$N(H_2)$ measurements taken using both of these methods may yield insight into the $N(H_2)$ structure in the ISM.

Figure 4.5 shows a comparison between $N(H_2)$ values for each source from the PGCC catalog, denoted $N(H_2)_{PGCC}$, and $N(H_2)$ as determined using the method outlined in §3.4 for each absorption component associated with the source, denoted $N(H_2)_{UV}$. For the CO-bright sample, all values derived from absorption-line measurements agree to within 3 standard deviations with the values listed in the catalog. This is in stark contrast to the CO-dark sample, for which over half (9/17) of these sightlines have $N(H_2)_{UV}$ values that are more than 3 standard deviations below their associated $N(H_2)_{PGCC}$ values. Importantly, in each of these cases, $N(H_2)_{PGCC}$ is significantly larger $N(H_2)_{UV}$. The sources that show this difference cover a broad range of angular distributions – that is to say, the extremely discrepant measurements are not isolated to the sightlines with the largest separation from their nearby PGCC source, as might be naively expected. Taking the weighted means of each of these two samples reveals that the CO-bright sample has average $N(H_2)_{UV}$ and $N(H_2)_{PGCC}$ values that agree to within $\sim$0.1 dex, whereas the CO-dark sample has a significantly larger difference, with the average $N(H_2)_{PGCC}$ nearly 0.8 dex larger than $N(H_2)_{UV}$.

The presence of CO-dark sightlines with $N(H_2)_{UV} \ll N(H_2)_{PGCC}$ at a broad range of angular distributions is indicative of structure in the H_2 spatial distribution. In particular, the observed discrepancies could arise from a "patchy" structure, with some fraction of the gas being relatively devoid of molecular material. The presence of this patchiness would serve to increase the surface area of the ISM that is subject to the interstellar UV radiation field, which would prevent any larger, coherent molecular regions from forming.

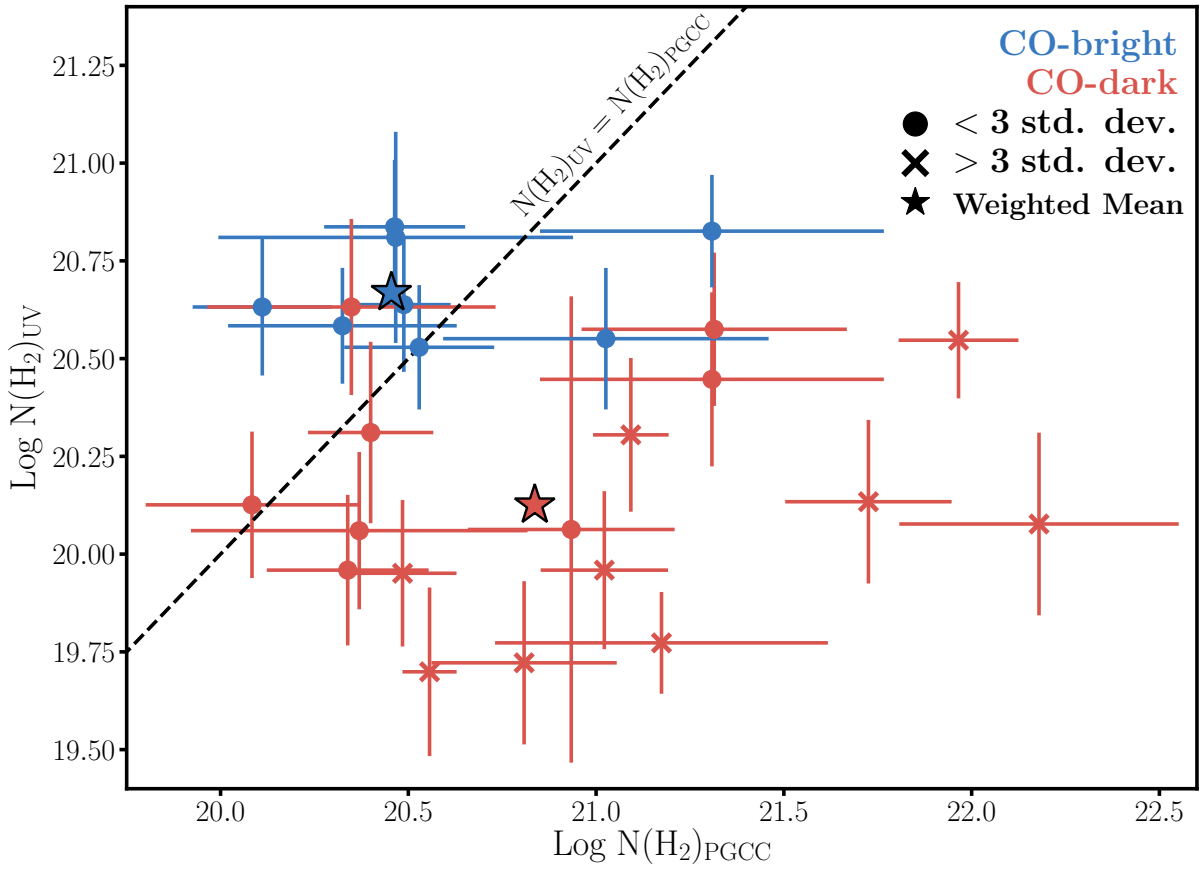

Figure 4.5. Comparison between $N(H_2)$ measurements listed for each source in the PGCC catalog (denoted as $N(H_2)_{PGCC}$) and those derived from UV absorption-line methods (denoted as $N(H_2)_{UV}$), see §3.4. CO-bright sightlines are coded blue, while CO-dark sightlines are coded red. Instances where the two measurements agree to within 3 standard deviations have circular points, while measurements which are discrepant by more than 3 standard deviations are shown with "×" markers. Additionally, weighted means of each sample are shown. Notably, all CO-bright measurements are in agreement, while roughly half (9/17) of the CO-dark sample have measurements which are discrepant.

Observationally, this patchy structure may be unresolved in the *Planck* dust emission maps due to a large beamwidth, but the narrow beam of an absorption sightline would

have some fractional chance of traveling though one of these regions which is relatively devoid of molecular material.

Conversely, the general agreement between $N(H_2)_{UV}$ and $N(H_2)_{PGCC}$ in the CO-bright sample indicates that the PGCC sources associated with these sightlines exist within smooth, translucent envelopes of gas. These regions appear to have properties analogous to the "translucent" definition from Burgh et al. (2010). Furthermore, this evidence of a smooth, coherent structure combined with the observed spatial dependence of N(CO) and the CO/C I ratio discussed in §4.2 indicate a traditional cloud-like structure, with a central, denser region tapering off into diffuse material at the outskirts of the cloud. Such a structure would better serve to shield its interior from the UV radiation capable of dissociating CO and H_2 molecules, leading to the higher overall CO abundance along these sightlines.

The combination of these H_2 results along with the results of §4.2 all seem to suggest that a transition occurs in the ISM gas around $N(CO) \sim 10^{15}$ cm^{-2}. Below this point the ISM appears to primarily contain diffuse, patchy structures, whereas above this transition point there appears to be larger, coherent, smooth envelopes of molecular material.

4.5. Gas Thermal Pressures

The study of the J=0,1,2 fine-structure excited states of C I has long been used to probe the gas thermal pressure in the interstellar medium (Jenkins & Shaya 1979; Jenkins & Tripp 2001, 2011). These individual states each give rise to discrete absorption lines with similar wavelengths, and thus are observed as multiplets in the ultraviolet. These multiplets are fit using absorption components to determine the individual column

densities associated with each of these J=0,1,2 states: N(C I), N(C I*), and N(C I**), respectively. To determine the gas thermal pressure $p/k = nT$, the relative populations of the two excited states can be represented by their fraction of the total observed C I

$$f_1 = \frac{\mathrm{N(C\ I^*)}}{\mathrm{N(C_{tot})}} \tag{4.1}$$

$$f_2 = \frac{\mathrm{N(C\ I^{**})}}{\mathrm{N(C_{tot})}} \tag{4.2}$$

where $\mathrm{N(C_{tot})} = \mathrm{N(C\ I)} + \mathrm{N(C\ I^*)} + \mathrm{N(C\ I^{**})}$. These relative populations can then be plotted against one another, as is done in Figure 4.6 for all PGCC components in this study, as well as the broader sample from Jenkins & Tripp (2011). For comparison, theoretical curves for a constant T and increasing number density n (and thus, increasing pressure) are included.

As is clear from this figure, observed values of f_1, f_2, rarely fall directly on these theoretical curves, instead preferentially lying above them at larger f_2 values. This behavior was taken by Jenkins & Tripp (2001, 2011) to indicate that the gas within the ISM is an admixture of gas at low and high pressures. The observed quantities thus represent a weighted mean of the entire distribution of gas pressure along the sightline, and thus tend to lie somewhere in between the low pressure regime at the bottom of the theoretical curve and the high pressure regime at the top of the curve. While those analyses were agnostic to separate components of absorption along the sightline, the same behavior is observed for the individual components of absorption studied here. This suggests that,

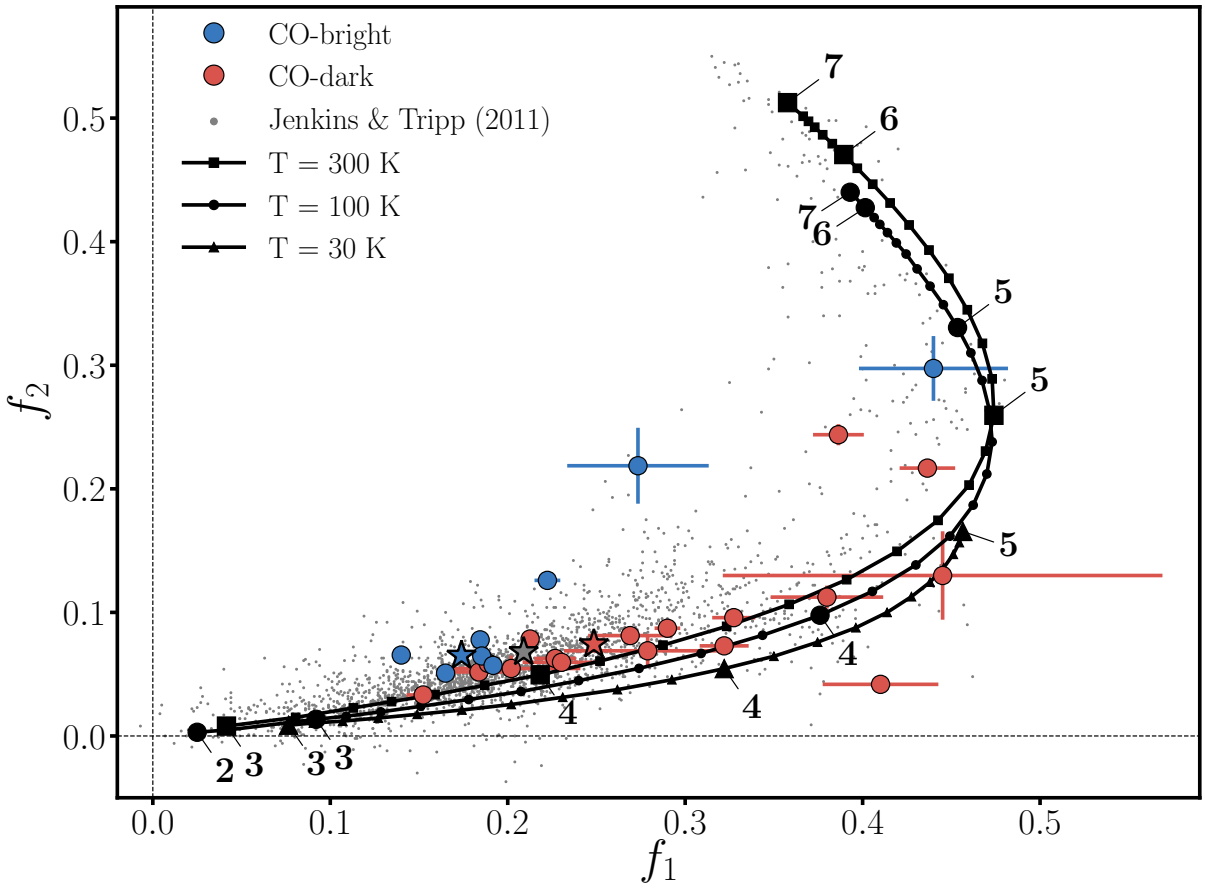

Figure 4.6. Behavior of the relative populations of the two excited fine-structure states N(C I*) and N(C I**), as defined by Eqs. 4.1 and 4.2. Blue and red points represent the CO-bright and CO-dark samples, respectively, defined in this work. Grey points represent the entire sample from Jenkins & Tripp (2011). Weighted means for each of these three samples are included as stars of each respective color. The black curve represents how the equilibrium f_1, f_2 values change as a function of gas pressure for gas at various temperatures. Black points along this curve represent increments of 0.1 in the logarithm of the gas pressure $\log(p/k)$, with larger points denoting integer values of this quantity along each curve.

even within a single component which probes the local gas behavior in the vicinity of the PGCC source, there appears to exist a distribution of gas thermal pressures.

Since the density is expected to increase near the center of these PGCC sources, the relationship between these quantities and the radial distance from the center of the source was investigated. As seen in Figure 4.7, the CO-bright and CO-dark samples do not distinguish themselves into separate regimes (as seen in Figure 4.2, for example). This indicates that value of these gas pressure diagnostics is not tied to specific regimes of CO or CO/C I.

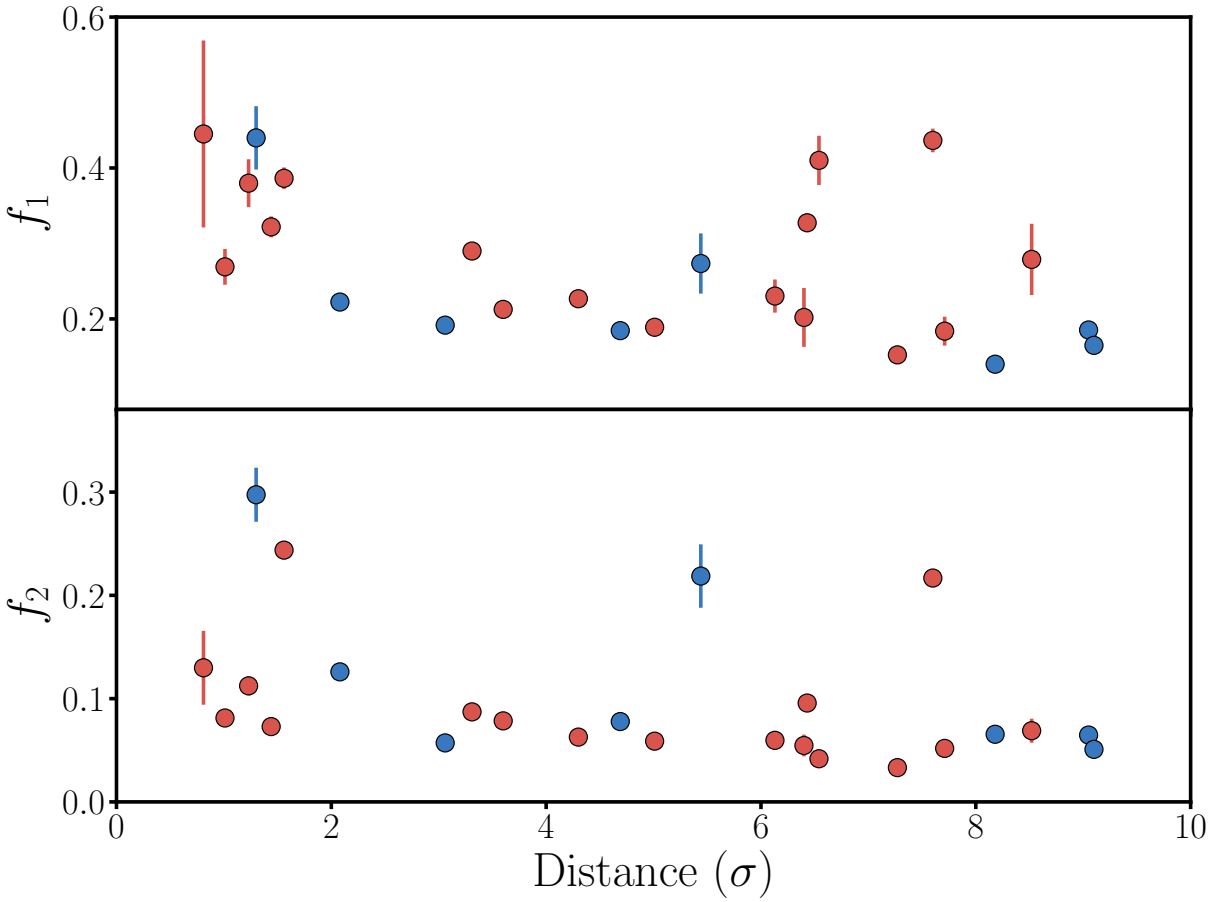

Figure 4.7. Behavior of the gas pressure diagnostics f_1, f_2 as a function of projected distance from the center of the PGCC source. Blue points indicate CO-bright components, while red points indicate CO-dark components.

Though the CO-bright sources do not appear to have distinct pressure values, previous results discussed in this work indicate that a transition does occur around N(CO)$\sim 10^{15}$ cm^{-2}. With this in mind, the behavior of these f_1, f_2 values in these individual regimes was investigated. When plotted instead purely as a function of N(CO), we see that a new trend emerges. Sightlines with N(CO)$>10^{15}$ cm^{-2} appear to have a positive correlation between N(CO) and f_1, f_2, whereas sightlines with N(CO)$<10^{15}$ cm^{-2} have f_1, f_2 values that appear entirely uncorrelated (Figure 4.8). This implies that sightlines probing the CO-dark "patchy" structures described in 4.4 are subject to a wide variety of gas thermal pressures. Once some critical threshold is reached around N(CO)$\sim 10^{15}$ cm^{-2} however, smoother, more coherent structures with well-behaved gas thermal pressures begin to emerge.

The observed f_1, f_2 quantities represent complex functions of temperature, density, irradiance, and admixtures of different parcels of gas. These quantities are not directly probed by our observations, making it difficult to disentangle the effects of each of these individual variables. A simple interpretation is to assume a typical temperature for the gas in order to derive an estimate of number density via the equation $p/k = nT$. With this in mind, the results of Figure 4.8 can further be interpreted as an expected positive correlation between N(CO) and the number density within the gas associated with the CO-bright PGCC sources.

4.6. Comparison to Results from Current PDR Modeling

In order to better understand the behavior along these sightlines, observational results were compared to PDR simulations by Gong et al. (2017). These simulations were chosen

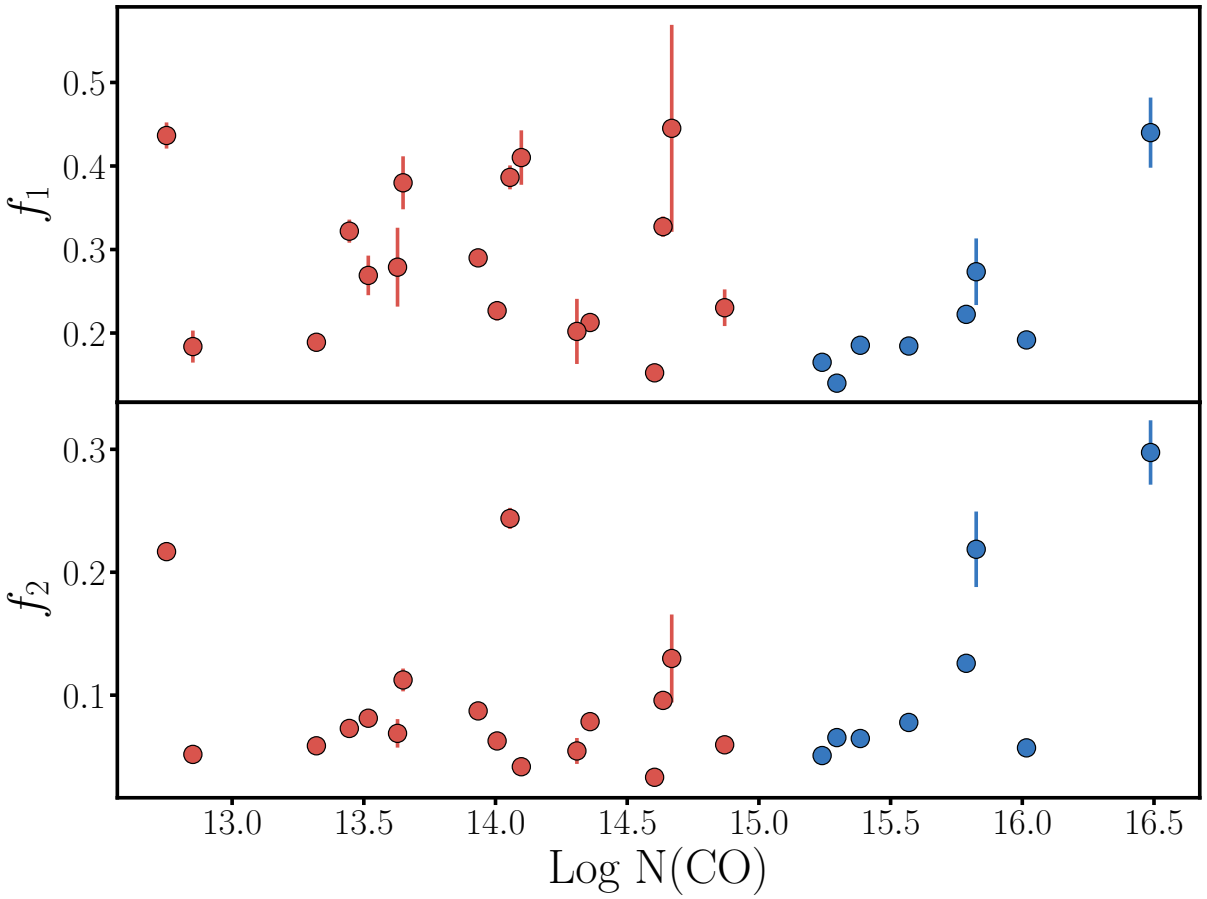

Figure 4.8. Relationship between the CO column density and the f_1, f_2 pressure diagnostics. Blue points represent CO-bright components, while red points represent CO-dark components. While the pressure diagnostics appear uncorrelated with N(CO) in the CO-dark regime, a positive correlation emerges once N(CO) reaches the 10^{15} cm^{-2} threshold.

specifically for their focus on the abundances of hydrogen and carbon species within the ISM, and because these models were shown to be more accurate overall than previously iterations of PDR models such as Nelson & Langer (1999) and Glover & Clark (2012). The Gong et al. (2017) results make predictions for the relative abundances of C II, C I, CO, H_2 and H_{total}, as well as the resulting integrated column densities for each of these species.

As such, it is possible to directly compare these simulation results to the observational results of this work.

One important caveat that will be relevant here is the consistent over-prediction of C I by an order of magnitude or more (shown previously in Figure 1.3), a common feature of PDR models that attempt to simulate equilibrium chemistry, dating back to some of the first modeling of such regions by van Dishoeck & Black (1988). Liszt (2011) argued that this may be due to the lack of understanding of the role of grain-assisted recombination, a process in which C II and a free electron combine on the surface of a dust grain to produce C I. This conjecture was investigated by Gong et al. (2017) by parameterizing the efficiency of such a recombination reaction, and found that while removing this process from their model does indeed lower the predicted C I abundance, it also affects the CO abundances in such a way that yields incorrect CO/C I ratios. In fact, the only model variation that Gong et al. (2017) found that could simultaneously reproduce the correct CO and C abundances was one in which the total gas-phase carbon abundance was depleted by a factor of $\sim$10. Interestingly, Burgh et al. (2010) found that their observed CO/C I and CO/H_2 ratios were best described by previous van Dishoeck & Black (1988) models that used a carbon depletion factor of 10. However, other observational evidence, such as the depletion study by Jenkins (2009), suggest that such an extreme depletion is unlikely.

Unsurprisingly, this effect is also seen when comparing the observational results found in this work to these model predictions, as shown in Figure 4.9. Rather than dismissing these models out of hand due to this discrepancy, their results can still be utilized if one assumption is made: that these theoretical models routinely overpredict the C I

abundance by some factor, and thus all of these predicted abundances can be reduced by the same factor to bring these results in line with the typical observed values. This assumption implies that the relative behavior of these abundances as a function of the total column density remains unchanged – it is only the overall scale that is incorrect. In reality, the reason for this discrepancy is likely to be more complicated than a constant factor, yet until more detailed simulations provide information about the specific nature of this overprediction, applying a correction factor remains the simplest solution by which to align the theoretical and observational results.

To estimate how large this correction factor is, the predicted C I values were systematically reduced until the differences between the observed C I values and the corresponding predictions matched those seen in the predicted and observed CO values. This correction factor was found to be 1.8 dex. The results of this correction are shown in the bottom panel of Figure 4.9.

4.7. Direct Comparison with Burgh et al. (2010) Results

The premise of Burgh et al. (2010) has considerable overlap with this work – they studied CO, C I, and H_2 in the context of the translucent ISM using STIS and *FUSE* data. However, there are a few key differences. Rather than using the PGCC or some comparable catalog to select sightlines as this work does, their sightline selection process was based entirely on total sightline extinction, as "translucent" sightlines have traditionally been defined as those with $A_V \sim 1$. Because of this, their numerical column density results are based on integrating the entire absorption profile, rather than isolating single components deemed to be arising from the actual translucent gas. Because of

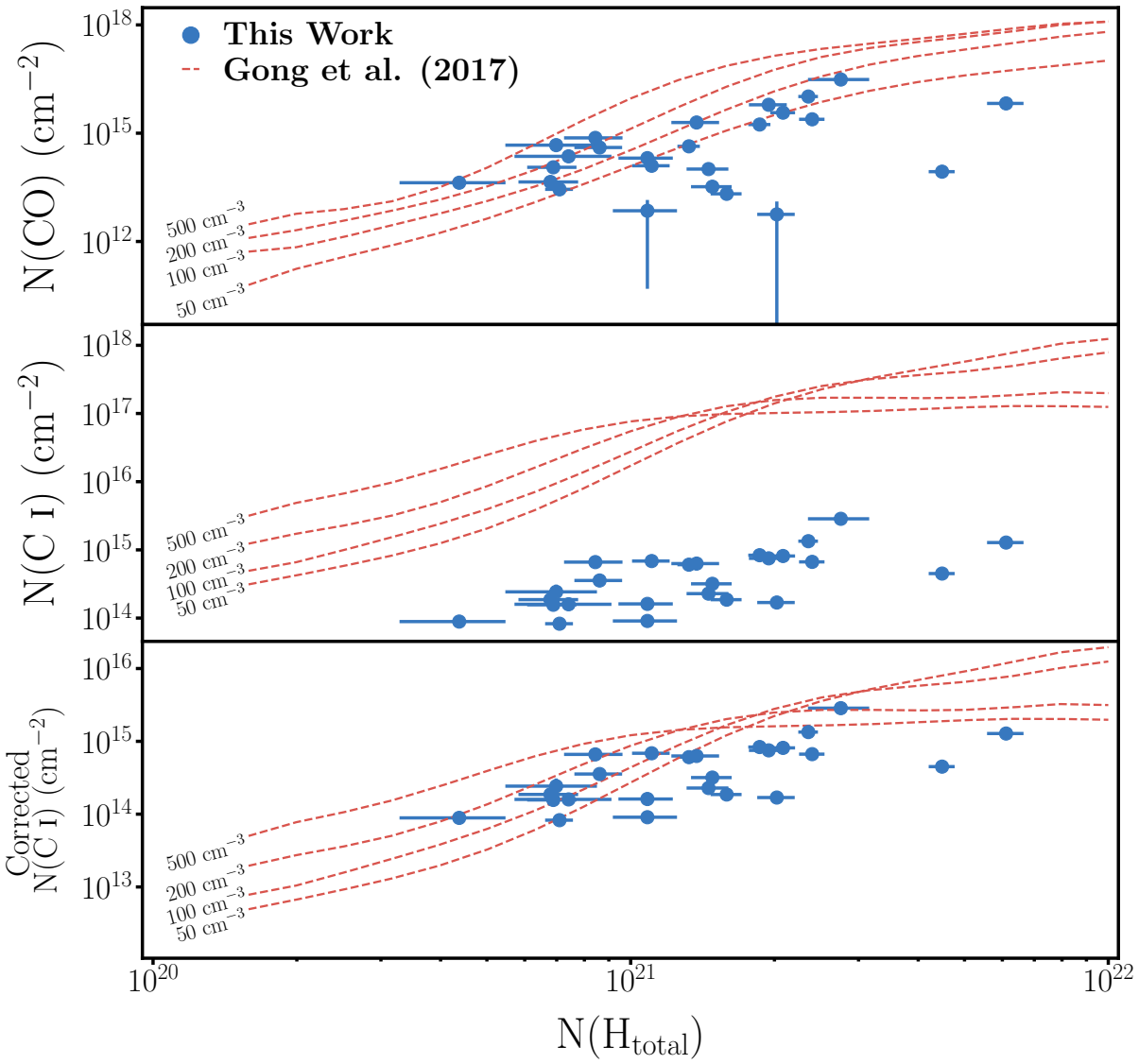

Figure 4.9. Comparison between observational data from this work (blue circles), and predictions from the PDR models of Gong et al. (2017) (red lines). Four separate models are included, with varying one-dimensional slab number densities, which are shown next to each model. Top and middle panels show the column densities of CO and C I, respectively, on the vertical axis, with respect to the total column density on the horizontal axis. While the models make reasonable predictions for the amount of observed CO, there is a clear discrepancy of more than an order of magnitude between the predicted and observed C I abundance. To account for this, the predicted C I abundances were modified downward by 1.8 dex such that they match the observations more appropriately. These corrected C I predictions are seen in the bottom panel.

these differences, a comparison between their results and those of this work may prove useful in understanding the specific nature of the PGCC sources, as well as the effects of profile-integration vs. isolating single components.

One of the important results of Burgh et al. (2010) was a steep increase in N(CO) over a relatively small range of N(C I). Between $3 \times 10^{14} <$ N(C I) $< 8 \times 10^{14}$ cm^{-2}, they observed N(CO) to increase by over 2 orders of magnitude. This was cited as evidence of a sharp transition in the observed molecular content along the sightline, where CO becomes the primary carbon-bearing species. However, when the individual component-wise N(CO) and N(C I) values determined in this work (including those not associated with PGCC sources) are plotted in comparison to those profile-integrated results (Figure 4.10), they result in a smoother transition between low and high N(CO) values. Furthermore, theoretical results from Gong et al. (2017) discussed in §4.6 are included for comparison. It is clear from this figure that the individual component values follow the predicted abundances more accurately, especially at lower N(C I) column densities, as these individual components better represent the true ISM properties.

The discrepancies between the data in this work and the data from Burgh et al. (2010) are almost certainly due to the effects of profile-integration vs. analysis of individual components. Since C I must form within the ISM before CO can be created, a sightline passing through multiple parcels of CNM gas is likely to observe more components of C I absorption than that of CO. Thus, the effects of profile-integration over the entire sightline would serve to drive the observed N(C I) to larger values without necessarily increasing the observed N(CO) by a commensurate amount. Figure 4.10 clearly shows this effect for N(C I) values below $\sim 8 \times 10^{14}$ cm^{-2}. Above this value, at the highest regimes for

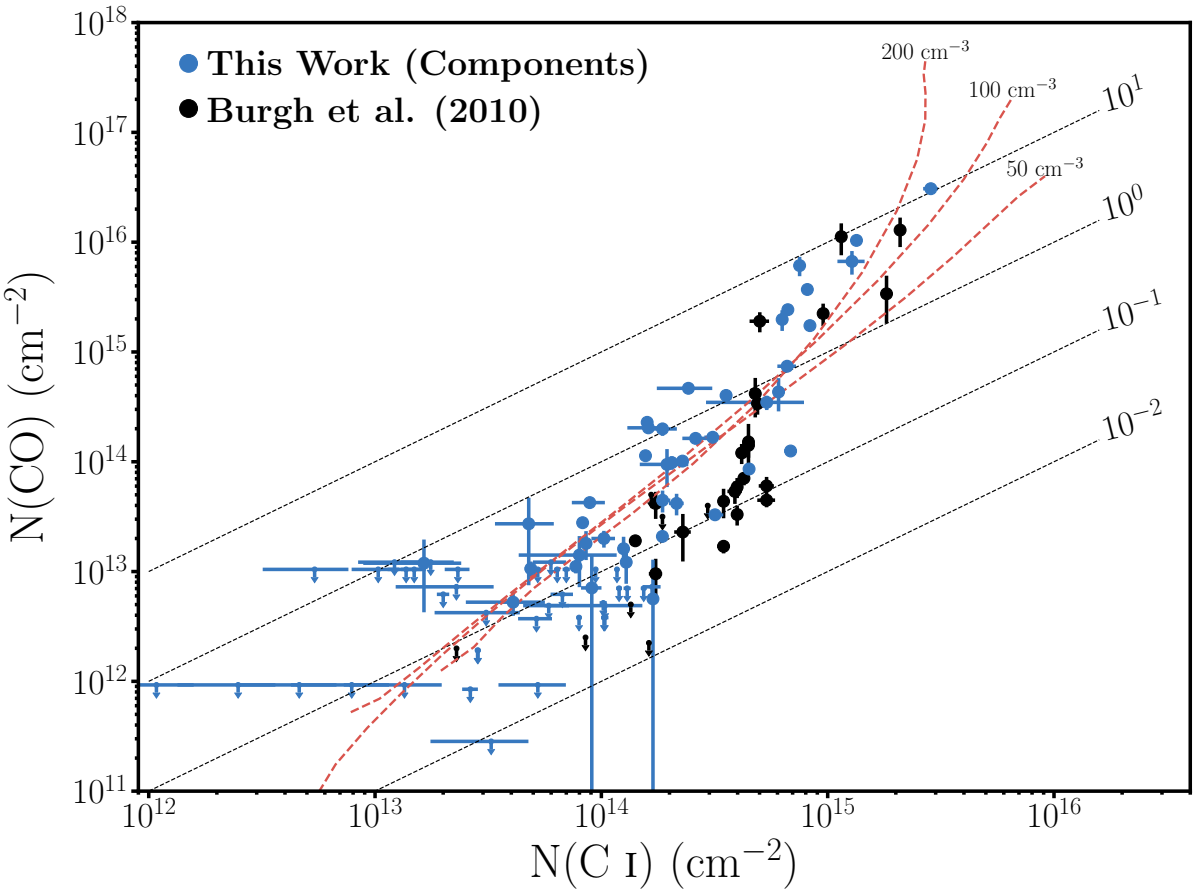

Figure 4.10. N(C I) vs. N(CO). Black points represent data from Burgh et al. (2010), which are profile-integrated values. In contrast, blue points represent data from this work for all detected individual absorption components (not just the components associated with PGCC sources, as described in §3.6). Red curves indicate predicted abundances from Gong et al. (2017) that have been corrected as per the discussion in §4.6.

both N(C I) and N(CO), the total observed column density is typically dominated by one component, thus the two methods will tend to converge.

With this effect in mind, one could ask: if the component-by-component results derived here were integrated across the entire sightline, and thus emulated the profile-integrated results of Burgh et al. (2010), would the two samples agree on the behavior of N(CO)

vs. N(C I)? The results of such a comparison are shown in Figure 4.11. As is clear from the figure, the smooth transition observed in the component-by-component analysis indeed becomes a much sharper transition akin to that of Burgh et al. (2010) when viewed as profile-integrated values. However, the specific transitionary region where N(CO) is observed to rise sharply occurs at a higher N(C I) value.

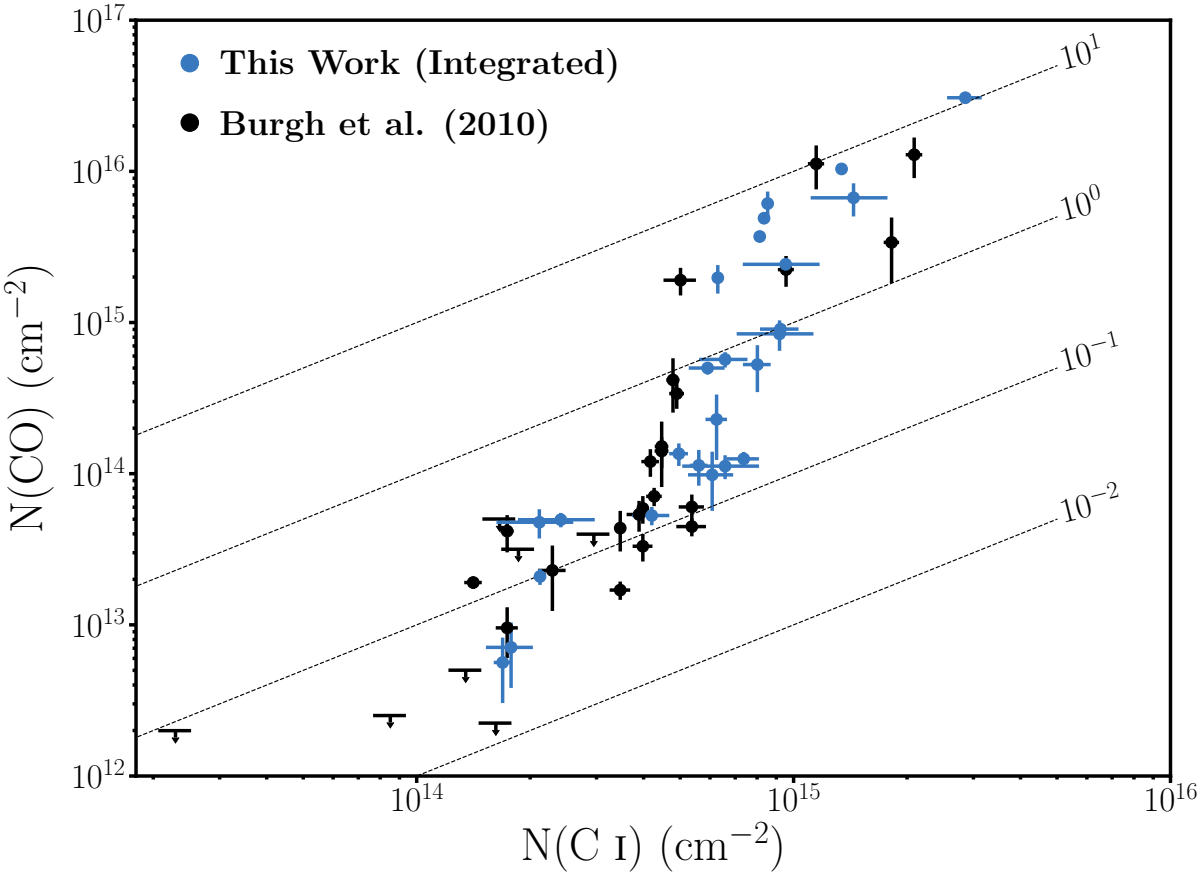

Figure 4.11. Profile-integrated N(CO) and N(C I) values. Color-coding is similar to Figure 4.10. Of note is the apparent shift in the location of the sharp upward rise of N(CO), which appears to occur at larger N(C I) for this work when compared to the Burgh et al. (2010) sample.

This shift is indicative that our PGCC sample is being biased toward larger N(C I) values, likely caused by an increased recombination of C II into C I. This increased recombination rate could be attributable to several factors. One is the potentially increased volume density along sightlines within the PGCC sources compared to the Burgh et al. (2010) sample of sightlines, which does not necessarily probe gas associated with PGCC sources. The PGCC sources are known to be cold, dusty sources – conditions associated with denser material within the ISM. This increased density would serve to increase the rate at which C II interacts with free electrons, yielding C I.

A second potential reason for this increased recombination could be related to the larger quantities of dust present in the PGCC sources that we are probing. These dust grains act as a catalyst for grain-assisted recombination (previously discussed in §4.6, which is thought to play a factor in the progression from C II to C I to CO (Liszt 2011). While the sightlines in this work are all known to pass through the regions surrounding PGCC sources and thus are likely probing the associated dust content, it is unclear how much dust exists along the sightlines of Burgh et al. (2010). As seen in Figure 4.12, a comparison of the sightline extinction values of the two samples reveals that the overall distributions are similar, indicating that there are not dramatic differences between the general sightline properties.

4.8. Correlations between Dust and Gas

Having probed the molecular gas associated with these sources, it is natural to wonder how this molecular gas is correlated with the dust embedded within it, as both are known to be important components of the cold, dense ISM. Using the methodology described in

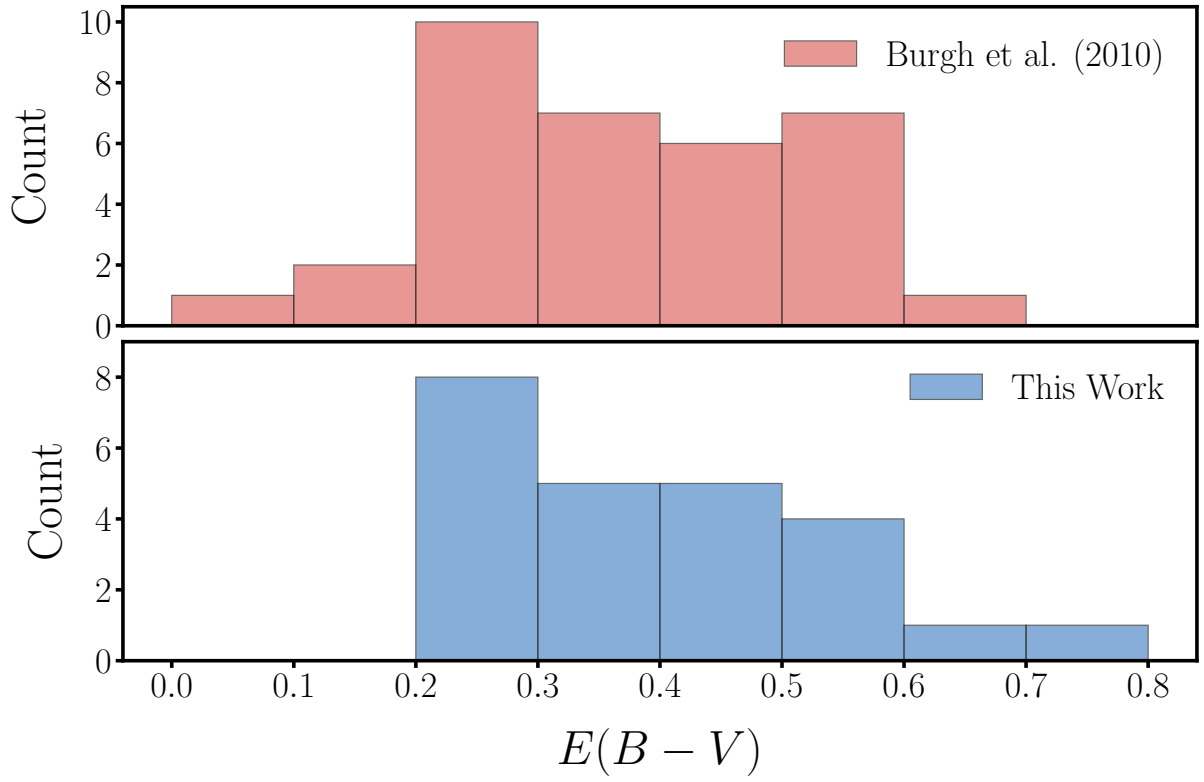

Figure 4.12. Histograms of the total sightline extinctions for all sightlines in Burgh et al. (2010) (red) and the sightlines in this work (blue).

§3.3.3, the dust content of the PGCC gas has been investigated by analyzing the gas-phase abundances of different elements that may be depleted onto these dust grains embedded within the gas. While it was shown in that section that only two elemental abundances are necessary to calculate a value for F_*, the wide bandpass of STIS and the density of elemental spectral lines in the ultraviolet often resulted in several elemental abundances being available for measurement. For cases where more than two elemental abundances were measured, pairwise combinations of all of the available elemental abundances can be used to sample F_* multiple times, and a single value can be determined by averaging all of the individually calculated F_* values. Using this formulation, measurements of gas-phase

elemental abundances from STIS absorption-line data (Table 4.2) have been combined with the selected elemental fit parameters from Jenkins (2009) and Jenkins (2019) which appear in Equation 3.12 (Table 3.1) to derive a single F_* value for each of the components associated with PGCC sources.

In a similar vein to §4.2, one might expect the dust depletions of the CO-bright sample to show some dependence on separation from the center of the source. As is seen in Figure 4.13, it appears that the CO-bright sample has, on average, a stronger dust depletion than the CO-dark sample. However, the distinction between these two samples is not nearly as sharp as seen in Figures 4.1 and 4.2. As studied in Hopkins & Lee (2016), the spatial distribution of gas and dust in the ISM can be considerably different depending on the size of dust grains.

In order to explicitly test the relationship between the gas and dust within the molecular ISM, this F_* parameter can be compared to N(CO). Furthermore, to test the importance of the PGCC environment on this relationship, an independent sample of non-PGCC sources is analyzed as well for the sake of comparison. This sample was garnered by combining sightlines which have an F_* value measured in Jenkins (2009) as well as a N(CO) measurement in Sheffer et al. (2008). As seen in Figure 4.14, PGCC absorption components show a positive correlation between F_* and N(CO), while the non-PGCC sample shows essentially no correlation between F_* and N(CO). This is clearly indicative of a link between the molecular gas and dust components of the ISM within these PGCC sources. As molecular gas becomes more abundant, elemental depletions onto dust grains becomes more prevalent.

Table 4.2. Gas-phase Elemental Abundances

Star	log N(O I)	log N(Kr I)	log N(Ge II)	log N(Mg II)	log N(Ni II)
HD 4768	17.35 ± 0.09	–	–	–	13.07 ± 0.07
HD 13841	17.37 ± 0.10	–	11.68 ± 0.07	15.36 ± 0.04	13.20 ± 0.05
HD 23180	17.63 ± 0.01	–	–	–	12.89 ± 0.02
HD 23478	17.43 ± 0.06	11.89 ± 0.07	11.76 ± 0.03	15.21 ± 0.02	12.83 ± 0.06
HD 24398	17.77 ± 0.01	–	–	–	13.05 ± 0.02
HD 24534	17.88 ± 0.01	–	–	–	13.17 ± 0.01
HD 25443	17.54 ± 0.05	11.98 ± 0.11	11.91 ± 0.05	15.47 ± 0.03	13.33 ± 0.02
HD 43582	18.16 ± 0.02	12.71 ± 0.06	12.49 ± 0.05	16.16 ± 0.06	13.49 ± 0.04
HD 62542	17.94 ± 0.06	12.46 ± 0.08	12.02 ± 0.12	14.89 ± 0.05	12.57 ± 0.05
HD 72350	17.34 ± 0.05	11.83 ± 0.08	11.51 ± 0.04	14.94 ± 0.02	12.72 ± 0.04
HD 108002	17.14 ± 0.11	–	–	15.53 ± 0.03	12.95 ± 0.03
HD 108927	17.64 ± 0.05	12.23 ± 0.07	12.02 ± 0.04	15.43 ± 0.03	13.05 ± 0.04
HD 112999	17.54 ± 0.06	12.19 ± 0.23	12.07 ± 0.03	15.78 ± 0.03	13.23 ± 0.03
HD 124314	17.67 ± 0.04	12.06 ± 0.15	12.00 ± 0.04	15.75 ± 0.02	13.15 ± 0.02
HD 147683	17.79 ± 0.03	12.38 ± 0.05	12.15 ± 0.03	15.62 ± 0.02	13.05 ± 0.02
HD 148594	17.81 ± 0.03	12.27 ± 0.09	12.12 ± 0.06	15.68 ± 0.03	13.29 ± 0.03
HD 165918	17.70 ± 0.03	–	–	–	13.43 ± 0.01
HD 185418	17.44 ± 0.05	11.91 ± 0.07	11.84 ± 0.04	15.45 ± 0.02	12.97 ± 0.03
HD 203532	17.82 ± 0.02	12.36 ± 0.04	12.05 ± 0.02	<13.48	12.77 ± 0.03
HD 208440	17.34 ± 0.06	11.78 ± 0.12	11.77 ± 0.04	15.57 ± 0.02	12.87 ± 0.03
HD 208947	17.55 ± 0.03	11.86 ± 0.08	11.96 ± 0.02	15.56 ± 0.01	13.38 ± 0.01
HD 210839	17.88 ± 0.02	12.06 ± 0.21	12.28 ± 0.05	15.74 ± 0.01	13.35 ± 0.02
HD 220058	17.68 ± 0.04	–	–	–	13.37 ± 0.02
HD 232522	17.36 ± 0.02	11.78 ± 0.07	11.79 ± 0.02	15.61 ± 0.02	13.36 ± 0.02
HD 254755	18.29 ± 0.03	–	–	–	13.72 ± 0.04

Gas-phase abundances for elements used to determine the dust depletion strength in the gas associated with the PGCC source. All listed column densities have units of log cm^{-2}. When applicable, upper limits are included. Entries with no listed values indicate that this species was not covered by STIS E140H data.

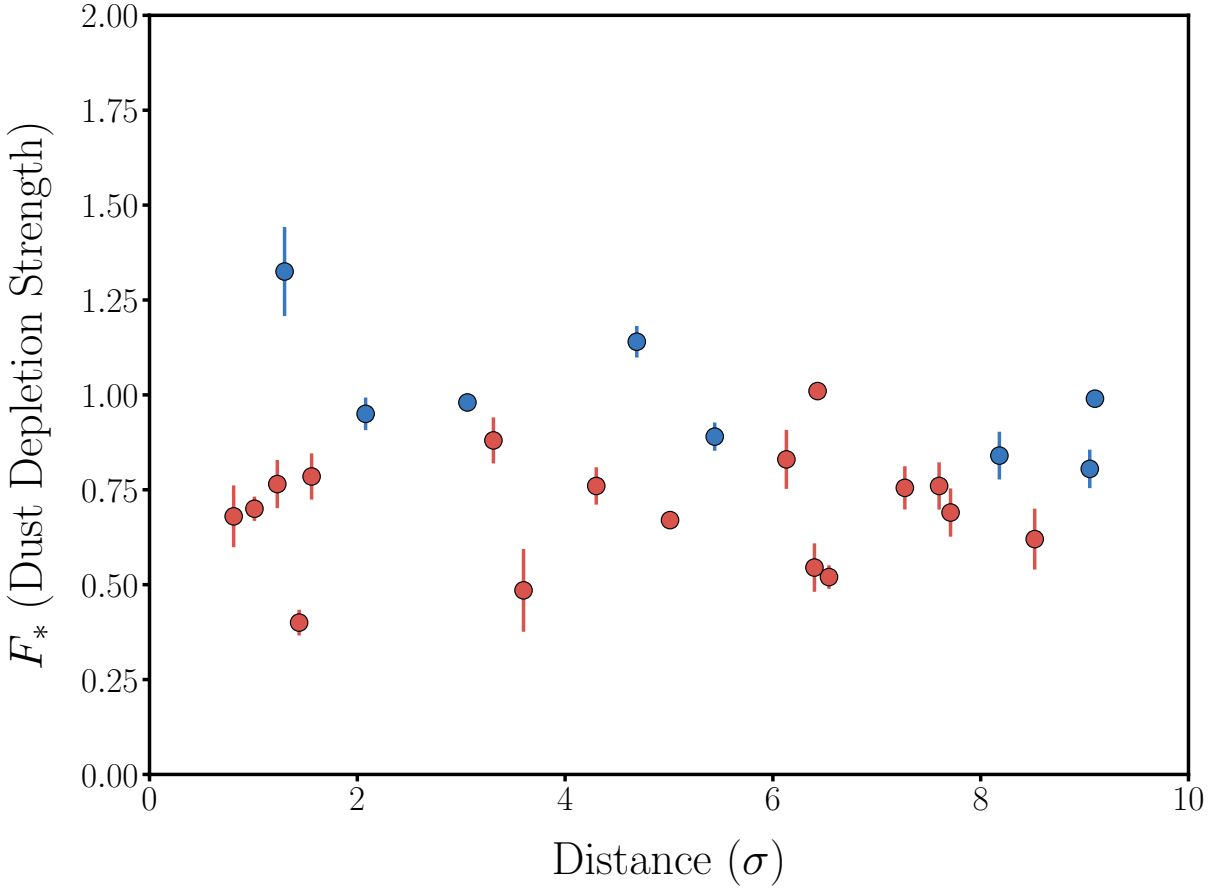

Figure 4.13. Calculated dust depletion strength parameter F_* as a function of the projected distance from the center of the associated PGCC source. Color-coding is the same as in Fig. 4.1, with CO-bright coded blue and CO-dark coded red. While a qualitatively similar difference between CO-bright and CO-dark can be seen, there is not nearly as clean of a distinction between these two samples, indicating that the dust and gas are not perfectly well-mixed.

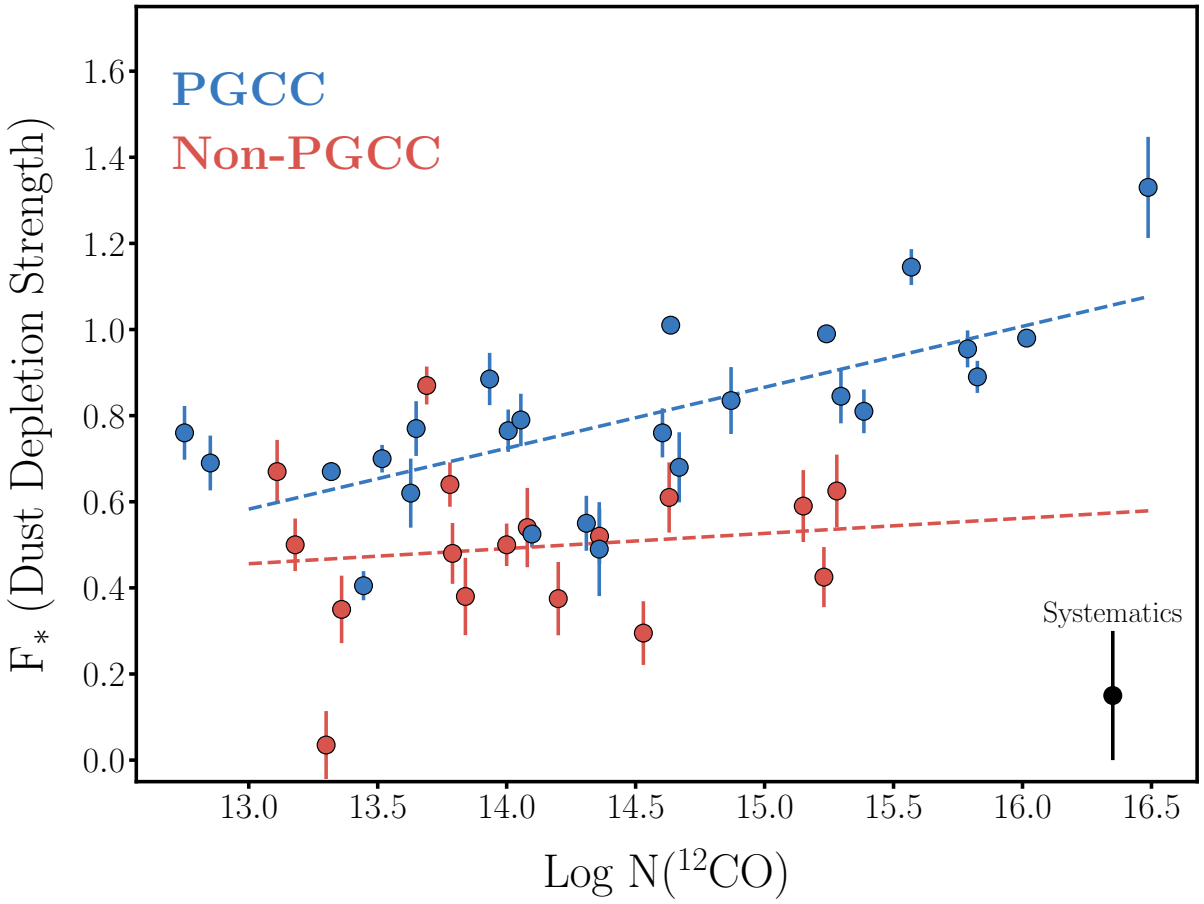

Figure 4.14. Calculated dust depletion strength parameter F_* as a function of the observed CO column density. Two samples are included: the individual absorption components associated with PGCC sources for sightlines discussed in this work, and a separate, non-PGCC sample compiled using F_* measurements from Jenkins (2009) and N(CO) measurements from Sheffer et al. (2008).

CHAPTER 5

Summary

Taken in their entirety, the results of this work suggest that PGCC sources do indeed cover a transitionary phase within the ISM. Based on these results, a transitionary point of N(CO)$\sim 10^{15}$ cm^{-2} is identified. One of the primary changes that appears to occur when this threshold is crossed is a change in the structure of the ISM. Smoother, more coherent molecular envelopes being to appear above this threshold, as evidenced by the emergence of spatial dependence in N(CO) and N(CO)/N(C I) (and to a lesser extent, the dust depletion strength F_*) appear, and the fact that above this threshold the N(H_2) measurements based on UV spectroscopy and sub-millimeter emission appear to converge. The threshold in N(CO)/N(C I) which defines this transition corresponds well with the definition of the translucence defined by Burgh et al. (2010), indicating that PGCC sources with these smooth coherent envelopes are part of the translucent ISM.

Analysis of these sightlines revealed that there exists two distinct classes of sources present in this study. These classes are denoted as "CO-bright" and "CO-dark," in accordance with their ability to be seen by typical radio observations, which are sensitive to N(CO) values of $>10^{15}$ cm^{-2} (Liszt 2007). CO-bright sightlines are found to have a clear dependence of their N(CO) and N(CO)/N(C I) values on separation from the center of the associated PGCC sources, while CO-dark sightlines show no such dependence (Figures 4.1, 4.2). The behavior of gas thermal pressure diagnostics determined from N(C I) and it's fine-structure excited states also support this distinction between CO-bright and

CO-dark sources, with CO-bright sources exhibiting a clear correlation between N(CO) and these pressure diagnostics, and CO-dark sources showing no correlation between these quantities. Finally, CO-bright sightlines have $N(H_2)_{UV}$ values that align well with the analogous $N(H_2)_{PGCC}$ values in the PGCC catalog, whereas CO-dark sightlines have $N(H_2)_{UV}$ values that are often considerably lower than $N(H_2)_{PGCC}$ (Figure 4.5).

These observations of CO, C I and H_2 are taken as evidence that the ISM within these CO-dark regions is "patchy" in nature, with some fraction of the gas being relatively devoid of molecular material. If this structure exists at scales smaller than the *Planck* beam size, it would be unresolved in the dust emission maps used to generate the PGCC catalog. However, the extraordinarily thin beam of an absorption sightline passing through one of these CO-dark regions would have some fractional chance of probing very little molecular material, as seen in the overall lower measured N(CO) and derived $N(H_2)$ abundances. Conversely, CO-bright regions appear to have smoother, more coherent molecular envelopes. This is evidenced by both the observed spatial dependence and the general agreement of $N(H_2)$ measurements, indicative that there is no such patchy sub-structure.

Further evidence that these CO-bright sources are smoother, more coherent envelopes is seen in the measurements of the individual CO isotopes ^{12}CO and ^{13}CO. The isotope ratio $^{12}CO/^{13}CO$ is known to be subject to variations by factors of a few in the presence of turbulent, dynamic gas (Szűcs et al. 2014). ^{13}CO was identified in 10 of the sightlines studied in this work, primarily biased toward the CO-bright sightlines. This CO isotope ratio was found to be essentially constant around the canonical $^{12}C/^{13}C$ values of $\sim$70 (Langer & Penzias 1990), indicating that these structures associated with the CO-bright

sightlines are static and quiescent. This is further supported by the relative line velocities of these two isotopes, which are found to be within 1 km s^{-1} of each other in all cases, whereas line velocities greater than 1 km s^{-1} have been observed in cold dense cores subject to turbulence (Zhang et al. 2011).

These observational results were also compared to current theoretical simulations. While N(CO) was found to match values expected from PDR simulations, the observed N(C I) values were found to be considerably lower than the predicted values by a factor of $\sim$1.8 dex. This reinforces a known issue with PDR modeling, highlighting the difficulty in capturing the behavior of C I within these regions, which may be exhibiting non-equilibrium effects due to gas dynamics or time-dependent chemistry (Gong et al. 2017). A simple, naive correction was applied to bring these theoretical values in line with the observed values for the sake of comparing to observational studies.

Perhaps the most comparable study to this work is that of Burgh et al. (2010), who also used *HST*/STIS to study CO and C I along translucent sightlines. A comparison of N(CO) and N(C I) values between the two works reveals the importance of profile-integration vs. cloud-component modeling, with the behavior of these abundance values from individual components more closely matching the behavior seen in theoretical models. This is not unexpected, as accurate cloud-component models allow for more accurate analysis of the local physical conditions that give rise to the individual components. Nonetheless, these results highlight important differences between the two methods and what information they tell us about the ISM along the sightline.

Finally, measurements of the molecular gas are compared to measurements of the dust content, via the gas-phase depletions of several elements know to constitute dust grains.

While a qualitatively similar trend with distance is seen in the dust depletion parameter F_* as was seen in N(CO) and N(CO)/N(C I), the distinction between CO-bright and CO-dark in F_* is not as clean as was observed in those gas-phase diagnostics. This indicates that while the transition to smoother, more coherent molecular envelopes seen in the gas phase has a qualitatively similar transition in the dust content (as the F_* for these CO-bright sightlines is on the whole larger), but it is not as strong of a distinguishing factor as the gas-phase diagnostics. However, the entire PGCC sample studied in this work displays a unique characteristic when compared to similar sightlines toward non-PGCC sources. PGCC sources appear to have dust depletion strengths that are correlated with their molecular gas content, with the F_* parameter nearly doubling (from $\sim$0.6 to $\sim$1.2) across the range of CO column densities probed here. This is in contrast with non-PGCC sightlines, whose dust depletion values appear roughly constant across all CO column densities, centered around $F_* = 0.5$ (albeit with a large scatter).

To arrive at these scientific results, a sample of sightlines was identified which probed the ISM in the vicinity of one of these PGCC sources. The angular separations between these sightlines and their associated PGCC sources range from very small separations, where the sightline is probing the actual "source" as identified within the catalog, to very large separations where the sightline probes the diffuse outer envelope of these sources. PGCC sources are identified as discrete objects embedded within the ISM, implying that the transition to translucent and molecular material is associated with structure within the ISM. As such, selecting sightlines which cover a range of separations from the center of identified PGCC sources is important in order to investigate this structure.

Sightlines which had high-resolution spectroscopic observations taken with *HST* were selected, allowing for comparison between data from the original PGCC catalog and data from absorption-line spectroscopy, two methods which are sensitive to entirely different angular resolutions. Furthermore, UV absorption-line spectroscopy is considerably more sensitive to CO than radio emission observations, allowing for scientific analyses not attainable through emission studies alone. Because of this increased sensitivity, this sightline selection process allowed for the study of a sample of PGCC sources that is representative of the inherent PGCC distribution, in contrast with previous studies of the PGCC using radio wavelengths which are inherently biased toward the densest sources (Wu et al. 2012; Yuan et al. 2016; Liu et al. 2018).

Data for these sightlines were obtained from the MAST archives and reduced using standard spectral reduction procedures to extract, co-add and normalize the spectra. To determine physical parameters such as column densities, linewidths, and central velocities, cloud-component models were constructed for each sightline, rather than integrating across the entire absorption profile. This method allows for the isolation and analysis of specific components deemed to be arising from the gas associated with PGCC sources, yielding a more accurate determination of the local conditions within this gas. Many of the analyses performed here focused on the behaviors of hydrogen and carbon, as these two elements have long been believed to be of utmost importance to the evolution of the physical conditions of the ISM. Transitions between the general phases of the ISM are often associated with a change in the behavior of one or both of these elements (Snow & McCall 2006) – a statement supported by the results of this work.

Dating back to the description of a multi-phase ISM first laid out by McKee & Ostriker (1977), observational and theoretical studies in the years since have sought to unravel the complex relationship between these elements, the observed structures in the ISM, and the physical conditions (such as density, temperature, and the impinging radiation fields) that mediate these structures and the ionization state of the elements that constitute them. This is especially important in the translucent ISM that serves as an intermediate phase in this transition, as this regime has often proved difficult to study observationally due to the limitations of observing molecular material in emission at low column densities (Liszt 2007) as well as theoretically due to the difficulties in correctly modeling the abundance of C I. (van Dishoeck & Black 1988; Bensch et al. 2003; Gong et al. 2017). Since the PGCC sources are known to contain cold dust and span a large range in $N(H_2)$, from $\sim 10^{19}$ cm^{-2} up to $\sim 10^{23}$ cm^{-2} (Planck Collaboration et al. 2016b), they almost assuredly play some role in this transition.

This work set out to determine what role the PGCC sources play in the larger role of the ISM's evolution from a warm, tenuous phase which fills the volume of the Galaxy to a cold, dense star-forming phase where the majority of the ISM's mass resides. With the above analyses, this work has identified physical characteristics that define the ISM associated with these PGCC sources and placed them in context relative to previous studies (both observational and theoretical) of the translucent ISM. These results show that the PGCC sources and their associated environments cover an important transitionary phase within the ISM, with this transition being associated with both the emergence of physical structure as well as changes in the physical conditions of the ISM associated with these sources.

References

André, P., Di Francesco, J., Ward-Thompson, D., et al. 2014, in Protostars and Planets VI, ed. H. Beuther, R. S. Klessen, C. P. Dullemond, & T. Henning, 27
Beckwith, S. V. W., Sargent, A. I., Chini, R. S., & Guesten, R. 1990, AJ, 99, 924
Bensch, F., Leuenhagen, U., Stutzki, J., & Schieder, R. 2003, ApJ, 591, 1013
Boggess, A., Carr, F. A., Evans, D. C., et al. 1978, Nature, 275, 372
Bolatto, A. D., Wolfire, M., & Leroy, A. K. 2013, ARA&A, 51, 207
Boulanger, F., Abergel, A., Bernard, J. P., et al. 1996, A&A, 312, 256
Burgh, E. B., France, K., & Jenkins, E. B. 2010, ApJ, 708, 334
Burgh, E. B., France, K., & McCandliss, S. R. 2007, ApJ, 658, 446
Cardelli, J., & Boehm-Vitense, E. 1982, ApJ, 262, 213
Carruthers, G. R. 1970, ApJ, 161, L81
Cartledge, S. I. B., Meyer, D. M., Lauroesch, J. T., & Sofia, U. J. 2001, ApJ, 562, 394
Clark, P. C., Glover, S. C. O., Ragan, S. E., & Duarte-Cabral, A. 2018, arXiv e-prints, arXiv:1809.00489
Crenny, T., & Federman, S. R. 2004, ApJ, 605, 278
Dame, T. M., Hartmann, D., & Thaddeus, P. 2001, ApJ, 547, 792
Dame, T. M., Ungerechts, H., Cohen, R. S., et al. 1987, ApJ, 322, 706
Dobbs, C. L., & Pringle, J. E. 2013, MNRAS, 432, 653
Draine, B. T. 1978, The Astrophysical Journal Supplement Series, 36, 595
—. 2003, ARA&A, 41, 241
Gaia Collaboration, Brown, A. G. A., Vallenari, A., et al. 2018, A&A, 616, A1
Glover, S. C. O., & Clark, P. C. 2012, MNRAS, 421, 116
Godard, B., Falgarone, E., & Pineau Des Forêts, G. 2009, A&A, 495, 847
Goldsmith, P. F., & Langer, W. D. 1978, ApJ, 222, 881
Gong, M., Ostriker, E. C., & Wolfire, M. G. 2017, ApJ, 843, 38
Gudennavar, S. B., Bubbly, S. G., Preethi, K., & Murthy, J. 2012, The Astrophysical Journal Supplement Series, 199, 8
Heiles, C., & Troland, T. H. 2003, ApJ, 586, 1067
Heyer, M., & Dame, T. M. 2015, Annual Review of Astronomy and Astrophysics, 53, 583
Hollenbach, D., & Salpeter, E. E. 1971, ApJ, 163, 155
Hopkins, P. F., & Lee, H. 2016, MNRAS, 456, 4174
Howk, J. C., & Sembach, K. R. 2000, AJ, 119, 2481
Jenkins, E. B. 2009, ApJ, 700, 1299

—. 2019, ApJ, 872, 55
Jenkins, E. B., & Shaya, E. J. 1979, ApJ, 231, 55
Jenkins, E. B., & Tripp, T. M. 2001, ApJS, 137, 297
—. 2011, ApJ, 734, 65
Jensen, A. G., Rachford, B. L., & Snow, T. P. 2005, ApJ, 619, 891
Jura, M. 1975a, ApJ, 197, 581
—. 1975b, ApJ, 197, 575
Kaczmarczyk, G. 2000, MNRAS, 312, 794
Krumholz, M. R., McKee, C. F., & Tumlinson, J. 2008, ApJ, 689, 865
Langer, W. D., & Penzias, A. A. 1990, ApJ, 357, 477
Lien, D. J. 1983, PhD thesis, Illinois Univ., Urbana-Champaign.
Liszt, H. S. 2007, A&A, 476, 291
—. 2011, A&A, 527, A45
Liu, T., Wu, Y., & Zhang, H. 2012, ApJS, 202, 4
Liu, T., Kim, K.-T., Juvela, M., et al. 2018, The Astrophysical Journal Supplement Series, 234, 28
Lodders, K. 2003, ApJ, 591, 1220
McKee, C. F., & Ostriker, J. P. 1977, ApJ, 218, 148
Meyer, D. M., Jura, M., & Cardelli, J. A. 1998, ApJ, 493, 222
Miville-Deschênes, M.-A., & Lagache, G. 2005, The Astrophysical Journal Supplement Series, 157, 302
Montier, L. A., Pelkonen, V. M., Juvela, M., Ristorcelli, I., & Marshall, D. J. 2010, A&A, 522, A83
Montillaud, J., Juvela, M., Rivera-Ingraham, A., et al. 2015, A&A, 584, A92
Moos, H. W., Cash, W. C., Cowie, L. L., et al. 2000, ApJ, 538, L1
Nelson, R. P., & Langer, W. D. 1999, ApJ, 524, 923
Neufeld, D. A., Wolfire, M. G., & Schilke, P. 2005, ApJ, 628, 260
Oka, T. 2013, Chemical Reviews, 113, 8738
Pineda, J. L., Goldsmith, P. F., Chapman, N., et al. 2010, ApJ, 721, 686
Planck Collaboration, Ade, P. A. R., Aghanim, N., et al. 2011a, A&A, 536, A1
—. 2011b, A&A, 536, A23
Planck Collaboration, Adam, R., Ade, P. A. R., et al. 2016a, A&A, 594, A1
Planck Collaboration, Ade, P. A. R., Aghanim, N., et al. 2016b, A&A, 594, A28
Rachford, B. L., Snow, T. P., Tumlinson, J., et al. 2001, ApJ, 555, 839
—. 2002, ApJ, 577, 221
Rachford, B. L., Snow, T. P., Destree, J. D., et al. 2009, The Astrophysical Journal Supplement Series, 180, 125
Savage, B. D., & Sembach, K. R. 1991, ApJ, 379, 245
Schneider, S., & Elmegreen, B. G. 1979, The Astrophysical Journal Supplement Series, 41, 87
Sheffer, Y., Rogers, M., Federman, S. R., et al. 2008, ApJ, 687, 1075

Shull, J. M., & Beckwith, S. 1982, Annual Review of Astronomy and Astrophysics, 20, 163
Shull, J. M., & van Steenberg, M. E. 1985, ApJ, 294, 599
Simon, R., Jackson, J. M., Rathborne, J. M., & Chambers, E. T. 2006, ApJ, 639, 227
Skrutskie, M. F., Cutri, R. M., Stiening, R., et al. 2006, AJ, 131, 1163
Snow, T. P., & McCall, B. J. 2006, Annual Review of Astronomy and Astrophysics, 44, 367
Sonnentrucker, P., Welty, D. E., Thorburn, J. A., & York, D. G. 2007, The Astrophysical Journal Supplement Series, 168, 58
Spitzer, Lyman, J., & Zabriskie, F. R. 1959, Publications of the Astronomical Society of the Pacific, 71, 412
Stecker, F. W., Solomon, P. M., Scoville, N. Z., & Ryter, C. E. 1975, ApJ, 201, 90
Szűcs, L., Glover, S. C. O., & Klessen, R. S. 2014, MNRAS, 445, 4055
Tarafdar, S. P., & Krishna Swamy, K. S. 1982, MNRAS, 200, 431
van Dishoeck, E. F., & Black, J. H. 1988, ApJ, 334, 771
Vázquez-Semadeni, E., Gómez, G. C., Jappsen, A. K., et al. 2007, ApJ, 657, 870
Vazquez-Semadeni, E., Passot, T., & Pouquet, A. 1995, ApJ, 441, 702
Watson, W. D., Anicich, V. G., & Huntress, W. T., J. 1976, ApJ, 205, L165
Welty, D. E., Hobbs, L. M., & Kulkarni, V. P. 1994, ApJ, 436, 152
Weselak, T., Galazutdinov, G., Beletsky, Y., & Krełowski, J. 2009, A&A, 499, 783
Weselak, T., Galazutdinov, G. A., Beletsky, Y., & Krełowski, J. 2010, MNRAS, 402, 1991
Wilson, R. W., Jefferts, K. B., & Penzias, A. A. 1970, ApJ, 161, L43
Wilson, T. L. 1999, Reports on Progress in Physics, 62, 143
Wolfire, M. G., Hollenbach, D., & McKee, C. F. 2010, ApJ, 716, 1191
Wolfire, M. G., Tielens, A. G. G. M., Hollenbach, D., & Kaufman, M. J. 2008, ApJ, 680, 384
Wu, Y., Liu, T., Meng, F., et al. 2012, ApJ, 756, 76
Young, J. S., & Scoville, N. 1982, ApJ, 258, 467
Yuan, J., Wu, Y., Liu, T., et al. 2016, ApJ, 820, 37
Zhang, S. B., Yang, J., Xu, Y., et al. 2011, The Astrophysical Journal Supplement Series, 193, 10

APPENDIX A

Tables of All Observed Absorption Components

Table A.1. All Observed CO Column Densities

Sightline	σ	Vel km/s	^{12}CO log cm^{-2}	^{13}CO log cm^{-2}
HD 4768	0.8	-35.0	<13.09	–
		-28.1	<13.09	–
		-23.3	14.54± 0.06	–
		-18.5	14.67± 0.04	–
		-14.1	13.44± 0.31	–
		-10.5	<13.09	–
		-7.0	<13.09	–
		-1.6	<13.09	–
		2.2	<13.09	–
HD 13841	3.6	-58.5	<13.02	–
		-52.9	<13.02	–
		-48.1	<13.02	–
		-44.3	<13.02	–
		-24.7	<13.02	–
		-18.7	<13.02	–
		-13.7	14.36± 0.05	–
		-10.2	<13.02	–
		-6.2	<13.02	–
		-2.9	<13.02	–
		2.5	<13.02	–
HD 23180	6.4	11.5	13.98± 0.16	<11.89
		14.7	14.64± 0.15	12.80± 0.06
HD 23478	6.1	11.0	14.87± 0.03	13.10± 0.11
		14.6	14.21± 0.03	<13.03
HD 24398	9.1	14.0	15.24± 0.02	13.39± 0.06
HD 24534	3.1	15.2	16.02± 0.01	14.22± 0.02

continued on next page

Sightline	σ	Vel	^{12}CO	^{13}CO
HD 25443	6.4	-11.6	14.22± 0.05	–
		-0.9	14.30± 0.06	–
		4.2	14.31± 0.04	–
HD 43582	3.3	7.3	13.93± 0.04	–
		14.4	13.09± 0.16	–
		20.7	13.15± 0.21	–
HD 62542	1.3	13.8	16.49± 0.03	14.58± 0.03
HD 72350	1.6	15.7	<12.85	–
		20.2	14.05± 0.03	–
		32.5	<12.85	–
		37.4	<12.85	–
HD 108002	8.5	-23.0	<11.97	–
		-19.5	<11.97	–
		-15.0	<11.97	–
		-8.8	<11.97	–
		-2.0	<11.97	–
		0.9	<11.97	–
		5.2	12.72± 0.11	–
		9.9	13.63± 0.04	–
HD 108927	8.2	10.2	15.30± 0.09	13.37± 0.14
HD 112999	7.7	-2.3	<12.79	–
		3.0	<12.79	–
		6.4	<12.79	–
		8.1	12.85± 0.43	–
HD 124314	4.3	-19.3	13.21± 0.12	–
		-13.5	<12.28	–
		-7.5	13.26± 0.13	–
		-2.5	<12.28	–
		2.8	14.01± 0.04	–
HD 147683	2.1	-0.9	15.79± 0.09	13.93± 0.02
		3.5	<12.71	<12.17
HD 148594	7.6	-4.7	12.75± 0.55	–
HD 165918	5.0	-11.8	<11.93	–
		-6.9	13.32± 0.03	–
HD 185418	7.3	-17.0	<12.63	–
		-11.1	14.60± 0.03	–
		-6.8	13.99± 0.06	–
		-2.7	<12.63	–
HD 203532	4.7	15.0	15.57± 0.04	13.70± 0.05

continued on next page

Sightline	σ	Vel	^{12}CO	^{13}CO
HD 208440	1.2	-29.1	13.08± 0.28	–
		-23.1	13.65± 0.10	–
		-18.5	13.62± 0.10	–
		-12.8	<12.86	–
		-6.3	<12.86	–
HD 208947	6.5	-22.0	<12.57	–
		-14.4	14.10± 0.04	–
HD 210839	9.1	-33.0	<12.58	<12.75
		-26.1	<12.58	<12.75
		-20.8	<12.58	<12.75
		-14.8	15.38± 0.02	13.47± 0.13
		-8.0	<12.58	<12.75
		-4.4	<12.58	<12.75
		-1.5	<12.58	<12.75
HD 220058	1.0	-14.0	13.30± 0.08	–
		-7.5	13.52± 0.05	–
HD 232522	1.4	-23.0	<11.45	–
		-17.0	13.45± 0.03	–
		-9.5	13.05± 0.06	–
		-6.1	13.03± 0.07	–
HD 254755	5.4	6.4	15.82± 0.11	13.96± 0.11
		16.2	<12.69	<13.20
		23.5	<12.69	<13.20
		30.0	<12.69	<13.20
		34.0	<12.69	<13.20
		37.0	<12.69	<13.20
		44.8	<12.69	<13.20

Table A.2. All Observed C I Column Densities

Sightline	σ	Vel	C I	C I*	C I**
		km/s	log cm^{-2}	log cm^{-2}	log cm^{-2}
HD 4768	0.8	-35.0	13.09± 0.10	<12.22	<12.23
		-28.1	13.25± 0.10	<12.22	<12.23
		-23.3	14.60± 0.34	14.02± 0.04	13.59± 0.06
		-18.5	14.01± 0.28	14.03± 0.04	13.50± 0.06
		-14.1	13.68± 0.12	<12.22	<12.23
		-10.5	13.71± 0.08	12.91± 0.13	<12.23
		-7.0	<11.99	<12.22	<12.23
		-1.6	<11.99	<12.22	<12.23
		2.2	<11.99	<12.22	<12.23
HD 13841	3.6	-58.5	13.01± 0.07	<12.08	<12.09
		-52.9	13.37± 0.04	<12.08	<12.09
		-48.1	12.73± 0.11	<12.08	<12.09
		-44.3	13.60± 0.01	13.09± 0.06	<12.09
		-24.7	13.17± 0.02	<12.08	<12.09
		-18.7	13.78± 0.01	12.63± 0.13	<12.09
		-13.7	14.05± 0.01	13.53± 0.02	13.10± 0.04
		-10.2	13.97± 0.01	11.60± 1.63	<12.09
		-6.2	14.00± 0.01	13.21± 0.05	<12.09
		-2.9	13.82± 0.01	12.62± 0.22	<12.09
		2.5	13.10± 0.02	12.01± 0.81	<12.09
HD 23180	6.4	11.5	14.16± 0.14	13.63± 0.02	12.94± 0.02
		14.7	14.54± 0.01	14.30± 0.03	13.76± 0.01
HD 23478	6.1	11.0	14.67± 0.06	14.18± 0.02	13.60± 0.02
		14.6	14.28± 0.07	13.75± 0.02	13.16± 0.03
HD 24398	9.1	14.0	14.82± 0.01	14.14± 0.02	13.63± 0.01
HD 24534	3.1	15.2	15.00± 0.01	14.41± 0.02	13.88± 0.01
HD 25443	6.4	-11.6	14.35± 0.05	13.84± 0.02	13.23± 0.04
		-0.9	14.20± 0.08	13.38± 0.03	12.72± 0.11
		4.2	14.08± 0.11	13.51± 0.02	12.95± 0.10
HD 43582	3.3	7.3	14.45± 0.01	14.12± 0.03	13.59± 0.04
		14.4	14.00± 0.01	13.35± 0.04	12.80± 0.15
		20.7	13.90± 0.12	<13.90	<18.35
HD 62542	1.3	13.8	14.88± 0.01	15.10± 0.06	14.93± 0.07
HD 72350	1.6	15.7	13.61± 0.03	13.75± 0.02	13.52± 0.02
		20.2	13.76± 0.03	13.78± 0.02	13.58± 0.02
		32.5	13.64± 0.03	13.81± 0.02	13.66± 0.03
		37.4	13.41± 0.02	13.71± 0.02	13.63± 0.03

continued on next page

Sightline	σ	Vel	C I	C I*	C I**
HD 108002	8.5	-23.0	12.90± 0.10	<12.81	<12.82
		-19.5	12.03± 0.60	<12.81	<12.82
		-15.0	12.39± 0.23	<12.81	<12.82
		-8.8	12.66± 0.14	<12.81	<12.82
		-2.0	13.56± 0.21	13.07± 0.07	12.68± 0.19
		0.9	13.13± 0.58	<12.81	<12.82
		5.2	13.53± 0.18	12.83± 0.12	<12.82
		9.9	13.76± 0.11	13.39± 0.05	12.79± 0.15
HD 108927	8.2	10.2	14.70± 0.01	13.95± 0.02	13.62± 0.03
HD 112999	7.7	-2.3	12.81± 0.04	12.89± 0.04	12.76± 0.06
		3.0	13.74± 0.06	13.02± 0.05	12.05± 0.31
		6.4	<11.77	<12.00	<12.01
		8.1	13.84± 0.06	13.22± 0.03	12.67± 0.07
HD 124314	4.3	-19.3	14.00± 0.01	13.39± 0.06	12.16± 0.86
		-13.5	13.45± 0.01	<11.62	<11.63
		-7.5	13.78± 0.01	13.36± 0.08	12.49± 0.39
		-2.5	13.46± 0.01	<11.62	<11.63
		2.8	14.21± 0.01	13.71± 0.06	13.16± 0.13
HD 147683	2.1	-0.9	14.69± 0.01	14.22± 0.04	13.98± 0.03
		3.5	13.81± 0.01	13.45± 0.05	12.96± 0.09
HD 148594	7.6	-4.7	13.77± 0.03	13.87± 0.02	13.56± 0.02
HD 165918	5.0	-11.8	13.42± 0.03	<11.93	<11.94
		-6.9	14.15± 0.01	13.55± 0.02	13.04± 0.06
HD 185418	7.3	-17.0	<11.69	<11.93	<11.94
		-11.1	14.46± 0.03	13.73± 0.03	13.07± 0.05
		-6.8	14.23± 0.05	13.49± 0.03	12.64± 0.12
		-2.7	13.49± 0.18	<11.93	<11.94
HD 203532	4.7	15.0	14.78± 0.01	14.18± 0.01	13.80± 0.01
HD 208440	1.2	-29.1	13.00± 0.47	12.80± 0.09	11.02± 4.38
		-23.1	13.98± 0.07	13.85± 0.02	13.32± 0.03
		-18.5	14.20± 0.04	13.65± 0.02	13.00± 0.06
		-12.8	14.09± 0.05	13.59± 0.02	12.70± 0.12
		-6.3	13.34± 0.22	11.95± 0.43	<11.66
HD 208947	6.5	-22.0	13.62± 0.09	12.90± 0.04	12.35± 0.16
		-14.4	14.57± 0.03	14.45± 0.05	13.46± 0.03
HD 210839	9.1	-33.0	13.45± 0.03	13.62± 0.02	13.53± 0.03
		-26.1	<12.87	<13.60	<18.05
		-20.8	<12.87	<13.60	<18.05
		-14.8	14.70± 0.01	14.09± 0.02	13.63± 0.01
		-8.0	13.76± 0.01	13.29± 0.04	12.53± 0.15
		-4.4	<12.87	<13.60	<18.05
		-1.5	13.80± 0.01	13.50± 0.02	12.90± 0.08

continued on next page

Sightline	σ	Vel	C I	C I*	C I**
HD 220058	1.0	-14.0	13.95± 0.06	13.07± 0.05	12.44± 0.21
		-7.5	14.31± 0.06	13.93± 0.02	13.41± 0.03
HD 232522	1.4	-23.0	13.50± 0.04	11.88± 0.89	<17.85
		-17.0	13.70± 0.01	13.43± 0.04	12.78± 0.13
		-9.5	13.69± 0.01	13.36± 0.04	12.75± 0.17
		-6.1	13.55± 0.01	13.00± 0.08	12.48± 0.33
HD 254755	5.4	6.4	14.81± 0.11	14.54± 0.08	14.45± 0.06
		16.2	13.48± 0.01	13.39± 0.22	12.57± 0.45
		23.5	13.89± 0.47	13.37± 0.05	12.42± 0.21
		30.0	<11.86	<12.26	<12.05
		34.0	<11.86	<12.26	<12.05
		37.0	<11.86	<12.26	<12.05
		44.8	<11.86	<12.26	<12.05

Table A.3. All Observed Hydrogen Column Densities

Sightline	σ	Vel km/s	H_2 log cm^{-2}	H_{tot} log cm^{-2}
HD 4768	0.8	-35.0	18.77± 0.20	<19.97
		-28.1	19.32± 0.20	19.61± 1.36
		-23.3	20.50± 0.22	20.88± 0.09
		-18.5	20.13± 0.19	20.84± 0.09
		-14.1	19.45± 0.13	<19.97
		-10.5	19.47± 0.20	20.52± 0.18
		-7.0	19.03± 0.20	<19.97
		-1.6	18.73± 0.20	<19.97
		2.2	18.42± 0.20	<19.97
HD 13841	3.6	-58.5	18.28± 0.20	20.31± 0.24
		-52.9	19.30± 0.20	19.27± 2.57
		-48.1	–	19.06± 4.54
		-44.3	19.27± 0.20	20.65± 0.13
		-24.7	18.90± 0.20	20.26± 0.27
		-18.7	19.62± 0.20	<19.92
		-13.7	19.95± 0.19	20.87± 0.10
		-10.2	–	20.24± 0.39
		-6.2	20.01± 0.20	20.80± 0.11
		-2.9	19.15± 0.20	20.77± 0.11
		2.5	–	20.18± 0.33
HD 23180	6.4	11.5	20.06± 0.15	20.78± 0.03
		14.7	20.55± 0.15	21.12± 0.02
HD 23478	6.1	11.0	20.57± 0.20	20.93± 0.06
		14.6	20.18± 0.21	20.88± 0.05
HD 24398	9.1	14.0	20.66± 0.19	21.27± 0.02
HD 24534	3.1	15.2	20.84± 0.17	21.37± 0.02
HD 25443	6.4	-11.6	20.26± 0.20	21.34± 0.04
		-0.9	20.02± 0.19	20.80± 0.08
		4.2	19.96± 0.19	21.04± 0.06
HD 43582	3.3	7.3	20.45± 0.22	21.65± 0.03
		14.4	19.92± 0.18	20.93± 0.06
		20.7	19.70± 0.31	20.74± 0.08
HD 62542	1.3	13.8	21.16± 0.16	21.44± 0.06
HD 72350	1.6	15.7	18.55± 0.20	<19.74
		20.2	19.96± 0.20	20.84± 0.05
		32.5	18.79± 0.20	<19.74
		37.4	18.56± 0.20	<19.74

continued on next page

Sightline	σ	Vel	H_2	H_{tot}
HD 108002	8.5	-23.0	17.98± 0.20	20.39± 0.21
		-19.5	17.53± 0.20	20.05± 0.44
		-15.0	–	19.86± 0.53
		-8.8	17.82± 0.20	<19.93
		-2.0	18.49± 0.20	<19.93
		0.9	19.04± 0.20	20.25± 0.26
		5.2	19.41± 0.22	20.85± 0.08
		9.9	19.72± 0.21	20.64± 0.11
HD 108927	8.2	10.2	20.53± 0.16	21.14± 0.05
HD 112999	7.7	-2.3	17.72± 0.20	<19.95
		3.0	19.03± 0.20	20.76± 0.13
		6.4	20.05± 0.20	21.04± 0.07
		8.1	19.77± 0.13	21.04± 0.07
HD 124314	4.3	-19.3	19.90± 0.20	21.33± 0.04
		-13.5	18.93± 0.20	20.22± 0.25
		-7.5	19.73± 0.19	20.78± 0.08
		-2.5	19.24± 0.20	20.66± 0.10
		2.8	20.13± 0.21	21.16± 0.04
HD 147683	2.1	-0.9	20.58± 0.15	21.29± 0.04
		3.5	19.81± 0.20	20.61± 0.15
HD 148594	7.6	-4.7	20.06± 0.60	21.31± 0.04
HD 165918	5.0	-11.8	19.00± 0.20	19.57± 0.64
		-6.9	20.08± 0.23	21.20± 0.03
HD 185418	7.3	-17.0	18.52± 0.20	<19.72
		-11.1	20.30± 0.20	20.93± 0.05
		-6.8	20.09± 0.20	21.33± 0.03
		-2.7	18.78± 0.20	20.49± 0.11
HD 203532	4.7	15.0	20.63± 0.18	21.32± 0.03
HD 208440	1.2	-29.1	18.98± 0.23	18.60± 6.97
		-23.1	20.06± 0.20	20.83± 0.06
		-18.5	20.13± 0.21	20.99± 0.05
		-12.8	20.82± 0.20	21.03± 0.04
		-6.3	18.81± 0.20	20.31± 0.15
HD 208947	6.5	-22.0	19.02± 0.20	20.29± 0.13
		-14.4	20.63± 0.23	21.04± 0.04
HD 210839	9.1	-33.0	19.09± 0.20	20.41± 0.09
		-26.1	18.30± 0.20	19.86± 0.37
		-20.8	19.07± 0.20	20.51± 0.08
		-14.8	20.55± 0.18	21.38± 0.03
		-8.0	20.90± 0.20	20.87± 0.05
		-4.4	19.38± 0.20	20.27± 0.13
		-1.5	18.81± 0.20	19.99± 0.22

continued on next page

Sightline	σ	Vel	H_2	H_{tot}
HD 220058	1.0	-14.0	19.80± 0.21	20.94± 0.06
		-7.5	20.31± 0.23	21.17± 0.04
HD 232522	1.4	-23.0	19.78± 0.20	20.11± 0.10
		-17.0	19.70± 0.22	20.85± 0.03
		-9.5	19.69± 0.22	20.84± 0.03
		-6.1	19.48± 0.21	20.57± 0.05
HD 254755	5.4	6.4	20.83± 0.14	21.79± 0.04
		16.2	20.52± 0.20	21.12± 0.06
		23.5	20.05± 0.20	20.96± 0.08
		30.0	20.06± 0.20	21.05± 0.07
		34.0	20.03± 0.20	<20.08
		37.0	19.26± 0.20	21.02± 0.08
		44.8	20.27± 0.20	<20.08

Table A.4. All Observed Dust Depletion Column Densities

Sightline	σ	Vel	O I	Kr I	Ge II	Mg II	Ni II
		km/s	log cm^{-2}	log cm^{-2}	log cm^{-2}	log cm^{-2}	log cm^{-2}
HD 4768	0.8	-35.0	<16.48	–	–	–	12.63± 0.11
		-28.1	16.12± 1.36	–	–	–	12.13± 0.28
		-23.3	17.38± 0.09	–	–	–	13.09± 0.06
		-18.5	17.35± 0.09	–	–	–	13.07± 0.07
		-14.1	<16.48	–	–	–	12.96± 0.08
		-10.5	17.03± 0.18	–	–	–	13.04± 0.08
		-7.0	<16.48	–	–	–	12.63± 0.12
		-1.6	<16.48	–	–	–	11.87± 0.46
		2.2	<16.48	–	–	–	<11.83
HD 13841	3.6	-58.5	16.81± 0.24	–	<10.32	15.15± 0.05	<11.60
		-52.9	15.78± 2.57	–	<10.32	15.19± 0.04	<11.60
		-48.1	15.56± 4.54	–	<10.32	<13.70	<11.60
		-44.3	17.15± 0.13	–	<10.32	15.20± 0.04	<11.60
		-24.7	16.76± 0.27	–	10.74± 0.44	14.70± 0.10	11.22± 3.02
		-18.7	<16.42	–	11.69± 0.07	15.46± 0.03	13.07± 0.06
		-13.7	17.37± 0.10	–	11.68± 0.07	15.36± 0.04	13.20± 0.05
		-10.2	16.75± 0.39	–	<10.32	<13.70	<11.60
		-6.2	17.31± 0.11	–	11.94± 0.05	15.55± 0.04	13.28± 0.05
		-2.9	17.28± 0.11	–	<10.32	15.32± 0.05	13.39± 0.04
		2.5	16.68± 0.33	–	<10.32	<13.70	<11.60
HD 23180	6.4	11.5	17.29± 0.02	–	–	–	12.58± 0.04
		14.7	17.63± 0.01	–	–	–	12.89± 0.02
HD 23478	6.1	11.0	17.43± 0.06	11.89± 0.07	11.76± 0.03	15.21± 0.02	12.83± 0.06
		14.6	17.38± 0.05	11.95± 0.06	11.70± 0.04	14.96± 0.03	12.86± 0.05
HD 24398	9.1	14.0	17.77± 0.01	–	–	–	13.05± 0.02
HD 24534	3.1	15.2	17.88± 0.01	–	–	–	13.17± 0.01
HD 25443	6.4	-11.6	17.84± 0.03	12.40± 0.05	12.31± 0.03	15.97± 0.02	13.23± 0.06
		-0.9	17.30± 0.08	11.67± 0.19	11.57± 0.09	15.23± 0.06	12.94± 0.06
		4.2	17.54± 0.05	11.98± 0.11	11.91± 0.05	15.47± 0.03	13.33± 0.02
HD 43582	3.3	7.3	18.16± 0.02	12.71± 0.06	12.49± 0.05	16.16± 0.06	13.49± 0.04
		14.4	17.44± 0.06	12.17± 0.14	11.86± 0.08	15.87± 0.04	13.51± 0.04
		20.7	17.25± 0.08	11.82± 0.23	11.83± 0.07	15.59± 0.05	13.37± 0.05
HD 62542	1.3	13.8	17.94± 0.06	12.46± 0.08	12.02± 0.12	14.89± 0.05	12.57± 0.05
HD 72350	1.6	15.7	<16.24	<11.00	<10.30	14.85± 0.03	12.08± 0.13
		20.2	17.34± 0.05	11.83± 0.08	11.51± 0.04	14.94± 0.02	12.72± 0.04
		32.5	<16.24	<11.00	<10.30	<13.49	<11.43
		37.4	<16.24	<11.00	<10.30	<13.49	<11.43

continued on next page

Sightline	σ	Vel	O I	Kr I	Ge II	Mg II	Ni II
HD 108002	8.5	-23.0	16.89± 0.21	–	–	15.28± 0.03	12.90± 0.04
		-19.5	16.55± 0.44	–	–	14.91± 0.05	12.60± 0.07
		-15.0	16.37± 0.53	–	–	14.58± 0.09	12.92± 0.04
		-8.8	<16.43	–	–	14.79± 0.06	13.30± 0.02
		-2.0	<16.43	–	–	<13.61	12.57± 0.08
		0.9	16.75± 0.26	–	–	15.27± 0.03	12.68± 0.06
		5.2	17.35± 0.08	–	–	15.73± 0.04	13.29± 0.02
		9.9	17.14± 0.11	–	–	15.53± 0.03	12.95± 0.03
HD 108927	8.2	10.2	17.64± 0.05	12.23± 0.07	12.02± 0.04	15.43± 0.03	13.05± 0.04
HD 112999	7.7	-2.3	<16.45	<11.27	<10.54	<13.73	<11.64
		3.0	17.27± 0.13	11.44± 1.11	11.54± 0.07	15.50± 0.02	12.56± 0.13
		6.4	17.54± 0.06	12.19± 0.23	12.07± 0.03	15.78± 0.03	13.23± 0.03
		8.1	17.54± 0.06	12.19± 0.23	12.07± 0.03	15.78± 0.03	13.23± 0.03
HD 124314	4.3	-19.3	17.83± 0.03	12.07± 0.14	12.12± 0.03	15.90± 0.02	13.46± 0.01
		-13.5	16.72± 0.25	<11.46	11.43± 0.09	15.07± 0.03	12.99± 0.03
		-7.5	17.28± 0.08	11.77± 0.24	11.59± 0.07	15.33± 0.03	12.65± 0.05
		-2.5	17.16± 0.10	<11.46	11.45± 0.09	15.34± 0.03	12.74± 0.04
		2.8	17.67± 0.04	12.06± 0.15	12.00± 0.04	15.75± 0.02	13.15± 0.02
HD 147683	2.1	-0.9	17.79± 0.03	12.38± 0.05	12.15± 0.03	15.62± 0.02	13.05± 0.02
		3.5	17.12± 0.15	<11.29	11.36± 0.09	14.98± 0.04	12.28± 0.11
HD 148594	7.6	-4.7	17.81± 0.03	12.27± 0.09	12.12± 0.06	15.68± 0.03	13.29± 0.03
HD 165918	5.0	-11.8	16.08± 0.64	–	–	–	<11.49
		-6.9	17.70± 0.03	–	–	–	13.43± 0.01
HD 185418	7.3	-17.0	<16.22	<11.04	<10.38	14.87± 0.03	<11.44
		-11.1	17.44± 0.05	11.91± 0.07	11.84± 0.04	15.45± 0.02	12.97± 0.03
		-6.8	17.83± 0.02	12.30± 0.04	12.20± 0.03	15.64± 0.02	13.41± 0.01
		-2.7	17.00± 0.10	<11.04	<10.38	14.78± 0.04	<11.44
HD 203532	4.7	15.0	17.82± 0.02	12.36± 0.04	12.05± 0.02	<13.48	12.77± 0.03
HD 208440	1.2	-29.1	15.10± 6.97	11.39± 0.23	10.39± 0.45	14.66± 0.05	11.66± 0.33
		-23.1	17.34± 0.06	11.78± 0.12	11.77± 0.04	15.57± 0.02	12.87± 0.03
		-18.5	17.50± 0.04	12.05± 0.06	11.88± 0.03	15.54± 0.02	13.32± 0.02
		-12.8	17.54± 0.04	12.00± 0.07	11.83± 0.04	15.45± 0.02	13.25± 0.02
		-6.3	16.82± 0.15	11.49± 0.18	11.37± 0.07	14.90± 0.03	12.74± 0.04
HD 208947	6.5	-22.0	16.80± 0.13	10.98± 0.51	11.25± 0.05	14.87± 0.02	12.81± 0.03
		-14.4	17.55± 0.03	11.86± 0.08	11.96± 0.02	15.56± 0.01	13.38± 0.01
HD 210839	9.1	-33.0	16.92± 0.09	<11.60	11.28± 0.15	14.82± 0.03	<11.43
		-26.1	16.37± 0.37	<11.60	11.32± 0.16	14.93± 0.03	<11.43
		-20.8	17.01± 0.07	<11.60	11.21± 0.18	14.63± 0.05	12.45± 0.06
		-14.8	17.88± 0.02	12.06± 0.21	12.28± 0.05	15.74± 0.01	13.35± 0.02
		-8.0	17.38± 0.05	<11.60	11.68± 0.08	15.53± 0.02	13.37± 0.02
		-4.4	16.77± 0.13	<11.60	<10.69	<13.56	11.76± 0.45
		-1.5	16.50± 0.22	<11.60	10.79± 0.39	14.57± 0.05	<11.43

continued on next page

Sightline	σ	Vel	O I	Kr I	Ge II	Mg II	Ni II
HD 220058	1.0	-14.0	17.44± 0.06	–	–	–	13.29± 0.03
		-7.5	17.68± 0.04	–	–	–	13.37± 0.02
HD 232522	1.4	-23.0	16.61± 0.10	10.71± 0.80	11.09± 0.08	14.93± 0.05	12.99± 0.03
		-17.0	17.36± 0.02	11.78± 0.07	11.79± 0.02	15.61± 0.02	13.36± 0.02
		-9.5	17.34± 0.02	11.63± 0.11	11.63± 0.03	15.73± 0.03	13.63± 0.02
		-6.1	17.07± 0.04	10.78± 0.91	11.57± 0.04	15.14± 0.07	13.21± 0.02
HD 254755	5.4	6.4	18.29± 0.03	–	–	–	13.72± 0.04
		16.2	17.62± 0.06	–	–	–	13.66± 0.04
		23.5	17.47± 0.08	–	–	–	13.28± 0.07
		30.0	17.55± 0.07	–	–	–	12.92± 0.09
		34.0	<16.59	–	–	–	<11.68
		37.0	17.52± 0.07	–	–	–	<11.68
		44.8	<16.59	–	–	–	12.72± 0.13